

Broadband single-chip transceivers for compact NMR probes

THÈSE N° 7755 (2017)

PRÉSENTÉE LE 29 SEPTEMBRE 2017
À LA FACULTÉ DES SCIENCES ET TECHNIQUES DE L'INGÉNIEUR
LABORATOIRE DE MICROSYSTÈMES 1
PROGRAMME DOCTORAL EN MICROSYSTÈMES ET MICROÉLECTRONIQUE

ÉCOLE POLYTECHNIQUE FÉDÉRALE DE LAUSANNE

POUR L'OBTENTION DU GRADE DE DOCTEUR ÈS SCIENCES

PAR

Marco GRISI

acceptée sur proposition du jury:

Prof. M. Gijs, président du jury
Dr G. Boero, directeur de thèse
Prof. M. Utz, rapporteur
Prof. D. Sakellariou, rapporteur
Prof. C. Dehollain, rapporteuse



ÉCOLE POLYTECHNIQUE
FÉDÉRALE DE LAUSANNE

Suisse
2017

*"Try a hard problem.
You may not solve it, but you will prove something else."*

Abstract

Nuclear magnetic resonance (NMR) is one of the most relevant spectroscopic tools in use today. However, NMR requires relatively expensive and complicated experimental settings given by the combination of high homogeneous magnetic fields and a relatively complex radio-frequency (RF) electronics. This thesis concerns the development of RF electronics hardware, specifically introducing new complementary-metal-oxide-semiconductor (CMOS) transceiver designs. This work stems from a collaboration between EPFL and Metrolab SA, and aims at pushing in two directions: first, NMR-oriented CMOS transceivers will simplify the implementation of NMR probes for both experimental and commercial applications; second, novel CMOS ultra-compact probes will deliver experimental versatility and improved sensing power at the nL and sub-nL scale.

We describe broadband 1 mm^2 transceivers operating in the range from 1 MHz to 1 GHz. The microchips include a RF power amplifier, a low-noise RF preamplifier, a frequency mixer, an audio-frequency (AF) amplifier, fully integrated transmit-receive switches, IQ signal generation, and broadband quadrature detection. In this work we show multi-nuclear NMR spectroscopy in combination with excitation/detection probe-heads based on micro-solenoids, therefore validating the broadband functioning. A combination of the transceivers and Metrolab's technology is also shown to deliver state-of-art performance in prototypes of commercial probes aimed for magnetometry. We shown that custom multichannel probes employing water samples of 500 nL are capable of measurement resolutions as high as $0.06 \text{ ppb/Hz}^{1/2}$ at 7 T, and that magnetic noise due to field fluctuations can be directly measured at this resolution level and distinguished by the electronic noise. Overall, the results of this package indicate that NMR-oriented CMOS transceivers simplify the implementation of NMR probes for both experimental and commercial applications.

When CMOS transceivers are combined to external resonators the resulting NMR probe may be called "compact" in the sense that the overall probe size is dominated by the excitation/detection resonator itself. Besides the implementation of compact probes, in this thesis we introduce the concept of ultra-compact NMR probes, where a single-chip transceiver is co-integrated with a multilayer microcoil realized with the metals of the CMOS technology. We demonstrate that with a non-resonant integrated coil of about $150 \text{ }\mu\text{m}$ external diameter a ^1H spin sensitivity of about $1.5 \cdot 10^{13} \text{ spins/Hz}^{1/2}$ is achieved at 7 T. This value of sensitivity compares well with the most sensitive inductive probes previously reported at similar volume

scales, with the resulting device showing an exceptional degree of versatility. We use, for the first time, a ultra-compact CMOS probe for the NMR spectroscopy of intact, static, sub-nL single ova of 0.1 and 0.5 nL, thereby reaching the relevant volume scale where life development begins for a broad variety of organisms, humans included. Thanks to the robustness and the versatility of the probe we could deliver a first extensive study of sub-nL single ova and indicate that ultra-compact probes are promising candidates to enable NMR-based study and selection of microscopic entities at biologically relevant volume scales. Overall, the results of this study indicate that CMOS ultra-compact probes will deliver experimental versatility and improved sensing power at the nL and sub-nL scale.

Keywords: NMR, CMOS, transceiver, broadband, microcoil, sub-nL, compact, magnetometry, ultra-compact, single-cell.

Riassunto

La risonanza magnetica nucleare (NMR) è tra i più importanti metodi di spettroscopia attualmente in uso. Tuttavia, l’NMR richiede un equipaggiamento sperimentale relativamente costoso e complicato, che consiste di un campo magnetico forte ed omogeneo e di una elettronica a radio-frequenze (RF) relativamente complessa. Questa tesi riguarda lo sviluppo di elettronica RF, introducendo nello specifico nuove architetture di circuiti transmit-receive CMOS (complementary-metal-oxide-semiconductor). Questo lavoro nasce come collaborazione tra l’EPFL e Metrolab SA, e il suo scopo è di spingere in due diverse direzioni: un primo obiettivo è di proporre circuiti CMOS transmit-receive per semplificare l’implementazione di sonde NMR per scopi sia sperimentali che commerciali; un secondo obiettivo è quello di introdurre una nuova topologia di probe NMR, chiamata ultra-compatta, che permette superiore versatilità e sensibilità a scale di volumi dell’ordine del nL e sub-nL.

Descriviamo un transmit-receive di 1 mm^2 operante a banda larga (da 1 MHz a 1 GHz). Il microchip include un amplificatore di potenza RF, un amplificatore RF low-noise, un mixer, un amplificatore audio frequenza (AF), un sistema di switch interamente integrato per passare da trasmissione a ricezione, la generazione on-chip di segnali in quadratura, una demodulazione in quadratura a banda larga. In questo lavoro mostriamo esperimenti di spettroscopia NMR multi-nuclei in combinazione con risonatori basati su micro-solenoidi, validando il funzionamento a banda larga. Mostriamo che una combinazione del transmit-receive con la tecnologia Metrolab permette di realizzare prototipi di magnetometri commerciali con prestazioni di avanguardia. Mostriamo che design personalizzati di sonde basate su campioni di acqua di 500 nL sono capaci di misurare un campo magnetico con una risoluzione di $0.06 \text{ ppb/Hz}^{1/2}$ a 7 T, e che il rumore intrinseco del campo magnetico può essere direttamente misurato e distinto dal rumore elettronico della sonda stessa. I risultati di questa prima parte indicano che i transmit-receive CMOS opportunamente progettati per esperimenti NMR facilitano e semplificano l’implementazione di sonde sia per scopi sperimentali che commerciali. Quando i transmit-receive CMOS sono combinati con risonatori esterni la sonda risultante può essere denominata "compatta", nel senso che la taglia della sonda è essenzialmente dominata dalla dimensione del risonatore stesso. Oltre alla implementazione di sonde compatte, in questa tesi introduciamo il concetto di sonda ultra-compatta, nella quale un transmit-receive è co-integrato assieme a una micro-bobina realizzata con i diversi livelli di metallizzazione della tecnologia CMOS. Dimostriamo che con una bobina CMOS non risonante avente un

diametro esterno di circa 150 μm è possibile raggiungere, in un campo magnetico di 7 T, una sensibilità sul protone (^1H) di circa $1.5 \cdot 10^{13}$ spins/Hz $^{1/2}$. Questo valore di sensibilità si confronta molto bene con le sonde induttive piu' sensibili fino ad oggi realizzate a scale di volumi simili. Inoltre, il dispositivo risultante mostra un livello di versatilità che puo' essere considerato eccezionale. Usiamo, per la prima volta in letteratura, una sonda ultra-compatta CMOS per fare spettroscopia NMR di singole uova intatte, statiche, aventi un volume di 0.1 e 0.5 nL, raggiungendo cosi' la scala di volume tipica dove inizia lo sviluppo della vita per molti organismi, inclusi gli umani. Grazie alla robustezza e alla versatilità delle sonde ultra-compatte possiamo divulgare il primo studio NMR esteso di uova aventi volumi sub-nL, deducendo che le sonde ultra-compatte sono candidati promettenti per abilitare studi basati su metodi NMR e selezione di entità microscopiche a scale di volumi biologicamente rilevanti. In conclusione, i risultati di questo studio indicano che le sonde CMOS ultra-compatte permetteranno versatilità sperimentali e sensibilità superiori a scale di volumi attorno e al di sotto del nL.

Parole chiave: NMR, CMOS, transmit-receive, banda larga, micro-bobina, sub-nL, compatta, magnetometria, ultra-compatta, singola cellula.

Contents

List of figures	vii
List of tables	ix
1 Introduction	1
1.1 NMR basics	1
1.2 CMOS electronics in NMR tools: trends	5
1.3 Sensitivity of mass-limited NMR probes	9
2 A broadband single-chip transceiver for multi-nuclear NMR probes	21
2.1 Abstract	21
2.2 Introduction	21
2.3 Electronics design	23
2.3.1 Transmitter	23
2.3.2 Receiver	25
2.3.3 Deadtime	25
2.3.4 Variable frequency probes	26
2.3.5 External coil: intrinsic gain and pulse time	27
2.3.6 Integrated coil	28
2.4 Experimental Setup	28
2.5 Results	30
2.5.1 Noise and Gain	30
2.5.2 Multinuclear NMR spectroscopy	31
2.5.3 Discussion	35
3 CMOS-based broadband NMR probes for high field magnetometry	37
3.1 Abstract	37
3.2 Introduction	37
3.3 Experimental Setup	39
3.3.1 Description of the integrated circuit	39
3.3.2 Description of the main unit	40
3.3.3 Data processing	42
3.3.4 Standard Probe Heads	42
3.4 Results	43

Contents

3.4.1	Resolution in DC field measurements	43
3.4.2	Compact multichannel field monitoring probes	45
3.4.3	Absolute accuracy	48
3.4.4	Conclusions	48
4	NMR spectroscopy of single sub-nL ova with ultra-compact single-chip probes	51
4.1	Abstract	51
4.2	Introduction	52
4.3	Results	53
4.3.1	Linewidth in <i>Rc</i> ova	53
4.3.2	Experiments on <i>Rc</i> ova with an alternative setup	54
4.3.3	<i>Rc</i> ova spectroscopy	56
4.3.4	<i>Hp</i> ova spectroscopy	58
4.3.5	Sensitivity (with maps) of the single-chip probe	59
4.3.6	Chemical shifts in <i>Rc</i> and <i>Hp</i> ova.	60
4.4	Discussion	61
4.5	Methods	63
4.5.1	Single ovum probe mounting.	63
4.5.2	Tardigrade <i>Richtersius coronifer</i> (<i>Rc</i>).	63
4.5.3	Nematode <i>Heligmosomoides polygyrus bakeri</i> (<i>Hp</i>).. . . .	64
4.5.4	NMR experimental details.	64
5	Appendix: supplementary, designs	65
6	Conclusions and Outlook	83
	Bibliography	89

List of Figures

1.1	Numerical example of Bloch equation solution.	4
1.2	Sub-nL probes employing external VS integrated coils.	8
1.3	PMMA-embedded copper microsolenoids.	18
2.1	Photograph and block diagram of single-chip transceiver	24
2.2	Multi-frequency probes schematics	26
2.3	Probes tuning and matching	27
2.4	Experimental Setup	29
2.5	Measured equivalent input noise voltage spectral density (<i>VSD</i>)	31
2.6	Measurements with the external coil probe in a field $B_0 = 7.05$ T	32
2.7	Measurements with the integrated coil in a field $B_0 = 7.05$ T	33
3.1	Schematics of CMOS-based variable frequency probe	39
3.2	IQ single-chip transceiver	40
3.3	Magnetometry unit	41
3.4	12 hours monitoring of RF and DC field	44
3.5	2-channel probe for simultaneous field monitoring	45
3.6	2-channel field monitoring	47
4.1	Samples and Setup	53
4.2	NMR spectroscopy of single <i>Richtersius coronifer</i> (<i>Rc</i>) ova	54
4.3	Additional experiments of single <i>Richtersius coronifer</i>	55
4.4	Comparison between single ova experiments in D_2O -based gel and D_2O -based gel background	56
4.5	Reproducibility study of <i>Richtersius coronifer</i> (<i>Rc</i>) spectra	57
4.6	NMR spectra of single <i>Heligmosomoides polygyrus bakeri</i> (<i>Hp</i>) ova and averaged spectra of <i>Richtersius coronifer</i> (<i>Rc</i>) and <i>Hp</i>	58
4.7	Maps of effective unitary field and effective sensitivity of the integrated microcoil	59
4.8	Schematic representation of the probe mounting procedure	63
5.1	Single-channel transceiver, 2014	67
5.2	LNA	69
5.3	Mixer	70

List of Figures

5.4	AF Amplifier	70
5.5	Switches	71
5.6	Single-channel transceiver, 2014	73
5.7	Ultra-compact single-chip probe, 2014	75
5.8	IQ transceiver, 2015	77
5.9	180° Shift	78
5.10	Divider	78
5.11	IQ transceiver, 2015	79

List of Tables

1.1	Performance and topology of reported mass limited NMR probes.	16
2.1	Performance and characteristics of the multinuclear probes	35
3.1	Field measurement resolution obtained and values of the optimal matched filter decay time	43
5.1	Physical dimensions of transistors used in LNA, Mixer, AF Amplifier.	72

1 Introduction

1.1 NMR basics

Most nuclei have an associated magnetic moment $\bar{\mu}$. When large collections of such nuclei are placed in a strong magnetic field \bar{B}_0 the thermal equilibrium corresponds to a resulting magnetization \bar{M}_0 , aligned to \bar{B}_0 , whose value is determined by the Boltzmann statistics. Each microscopic magnetic moment $\bar{\mu}$ is proportional to the angular momentum \bar{l} of the nucleus by a factor γ : the so-called gyromagnetic ratio (which literally means ratio between the angular and magnetic momenta). Taken a nucleus with spin I , one has $\bar{l} = \hbar I$ and $\bar{\mu} = \gamma \hbar I$. γ is a factor which depends on the nature of the nucleus. As better explained below, this parameter determines the RF frequency needed to interact with the nuclear species when the sample is placed in a static magnetic field. Value of γ for a large variety of nuclei are extensively reported in literature. In this thesis we make little exploration of nuclei other than ^1H , which is the easiest nucleus to sense, having high abundance and an high resonating frequency. In general, this short treatment is restricted to nuclear paramagnetism, where the energy term in the Hamiltonian can be approximated by $H \simeq \pm \bar{\mu} \cdot \bar{B}_0$. The thermal magnetization of a sample can be determined by the value of the spin and by the density N_s of spins per unit volume. Taken the average magnetic moment $\bar{\mu}_{av}$ one can define the magnetization of the sample as $\bar{M}_0 = N_s \bar{\mu}_{av}$. In terms of Boltzmann statistics this translates to:

$$M_0 = N_s \frac{\sum_{m=-I}^I \gamma \hbar m \cdot e^{-(\gamma \hbar m B_0 / k_B T)}}{\sum_{m=-I}^I e^{-(\gamma \hbar m B_0 / k_B T)}} \quad (1.1)$$

where the energies related to the spin states are expressed as $E_m = \bar{\mu} \cdot \bar{B}_0 = \gamma \hbar m B_0$. At room temperature we always have a situation in which $k_B T \gg E_m$, which facilitates the expression of \bar{M}_0 . The sum resulting on top of eq. (1.1) can be reduced telescopically, while at the bottom

Chapter 1. Introduction

the resulting term simply counts the number of states. The final result is:

$$\overline{M}_0 = \frac{N_s(\gamma\hbar)^2 I(I+1)\overline{B}_0}{3k_B T} \quad (1.2)$$

Equation (1.2) describes the physical origin of the magnetization that can be measured in a nuclear magnetic resonance experiment. In a nutshell, during an NMR experiment the magnetization in eq. (1.2) is manipulated via the application of RF magnetic fields. The resulting rotational movement of \overline{M}_0 is then sensed and all the efforts in the experiment are dedicated to work out information about the sample, which is encoded in the detailed response of \overline{M}_0 to RF fields and the dynamics of its relaxation towards the thermal equilibrium. A theoretical description of such dynamics was first proposed by Felix Bloch [1, 2] and resulted in those which are now called the Bloch equations. Although it exists a more rigorous quantum mechanical treatment, the Bloch equations can be derived with a classical physics approach. The torque on a magnetic moment $\overline{\mu}$ placed in a magnetic field is given by $\overline{\tau} = \overline{\mu} \times \overline{B} = \frac{d\overline{l}}{dt}$, \overline{l} being the angular momentum. For a microscopic magnetic moment one has $\overline{\mu} = \gamma\overline{l}$ as previously discussed. The same principle can be applied at the scale of a bulk sample, where \overline{M} has the role of the magnetization. Its equation of motion can thus be written as:

$$\frac{d\overline{M}}{dt} = \gamma\overline{M} \times \overline{B} \quad (1.3)$$

Equation (1.3) clearly considers a case where the spins that constitute the magnetization \overline{M} do not feel each other and, more relevantly, there is no term in (1.3) suggesting that when \overline{B} is constant a thermal equilibrium condition exists and is approached at long times (\overline{M}_0 from equation (1.2)). In order to write Bloch equations the relaxation processes of \overline{M} towards equilibrium must be considered. Before discussing relaxation we can note that in eq. (1.3) we can already find the signature of the resonance phenomenon from which the term NMR originates. The best way to make this observation is to translate eq. (1.3) into a reference frame which rotates at an angular frequency $\overline{\omega}$:

$$\frac{d\overline{M}_\omega}{dt} = \gamma\overline{M}_\omega \times \left(\overline{B} - \frac{\overline{\omega}}{\gamma}\right) \quad (1.4)$$

If we assume that it only exists a field \overline{B}_0 , constant and uniform over the sample, we can see that for $\overline{\omega} = \gamma\overline{B}_0$ the magnetization \overline{M}_ω is constant. Thus, this is telling us that the frequency $\omega_0 = \gamma B_0$ (called the Larmor frequency) would determine the precession motion of \overline{M} in the laboratory frame in the case where \overline{M} was displaced from the direction of the field (i.e., M_x

and/or $M_y \neq 0$ if we assume $\overline{B}_0 = B_0 \hat{z}$). Even more relevantly, we can already see that in such precession motion the information about the nuclear species is encoded in the frequency via the term γ . Further, what makes NMR powerful is the fact that also the chemical environment of a nucleus can affect the Larmor frequency via slight modifications of the term B_0 due to the shielding of the magnetic field, which changes from molecule to molecule. In a nutshell, the detection of the Larmor frequencies that reside into a given sample is what allows for NMR spectroscopy of bulk matter.

In order to perform an NMR experiment it is necessary, in the most used experimental frame (to date), to displace the magnetization $M_0 \hat{z}$ into the \hat{x} - \hat{y} plane and detect the dynamics of its precession during relaxation towards thermal equilibrium. The initial displacement is achieved by the application of radio-frequency (RF) fields \overline{B}_1 (much weaker than B_0) which are perpendicular to \hat{z} and have frequencies right at the Larmor value. From eq. (1.4) it is possible to see that upon the action of a field \overline{B}_1 at the Larmor frequency the magnetization \overline{M}_ω approaches the \hat{x} - \hat{y} plane such that the angle θ between \overline{M}_ω and \hat{z} is $\theta = \gamma B_1 \tau$, τ being the duration of the B_1 pulse. When the B_1 pulse stops and the magnetization has exposed components in \hat{x} - \hat{y} there are two different mechanisms of relaxation acting to restore $M_0 \hat{z}$. Along the direction \hat{z} the magnetic moments of the nuclei can be significantly displaced only by field components perpendicular to B_0 and at the Larmor frequency: this is due to the fact that \overline{B}_0 is strong and only resonant and perpendicular fields (as discussed) can affect \overline{M}_ω along \hat{z} . On the other hand, in the \hat{x} - \hat{y} plane the components of \overline{M}_ω can more easily disappear. In simple terms, M_x and M_y can survive in their precession only if all the spins in the sample have a coherent precession motion around \hat{z} . Decoherence is induced by either interactions among spins or inhomogeneities of the field over the sample region (leading to inhomogeneity of the precession frequency, and thus to dephasing in \hat{x} - \hat{y}). The complete Bloch equation includes terms accounting for these relaxation mechanisms and approximates them with an exponential dynamics. Calling T_1 the relaxation time along \hat{z} and T_2 the \hat{x} - \hat{y} one, the resulting dynamics is described by the following equation:

$$\frac{d\overline{M}}{dt} = \gamma \overline{M} \times \overline{B} - \frac{M_x \hat{x} + M_y \hat{y}}{T_2} - \frac{M_z - M_0}{T_1} \hat{z} \quad (1.5)$$

Figure 1.1a shows the evolution of the magnetization components after a B_1 pulse at the Larmor frequency yielding $\theta = \pi/2$. As we can see, M_x and M_y relax exponentially with a decay time T_2 and M_z is restored with a typical time T_1 . As shown in Fig. 1.1b, the Larmor frequency can be directly measured after FFT of the M_x and M_y dynamics. From Fig. 1.1 it is evident that a detection scheme linearly related to M_x and M_y would allow for NMR spectroscopy of the magnetized sample.

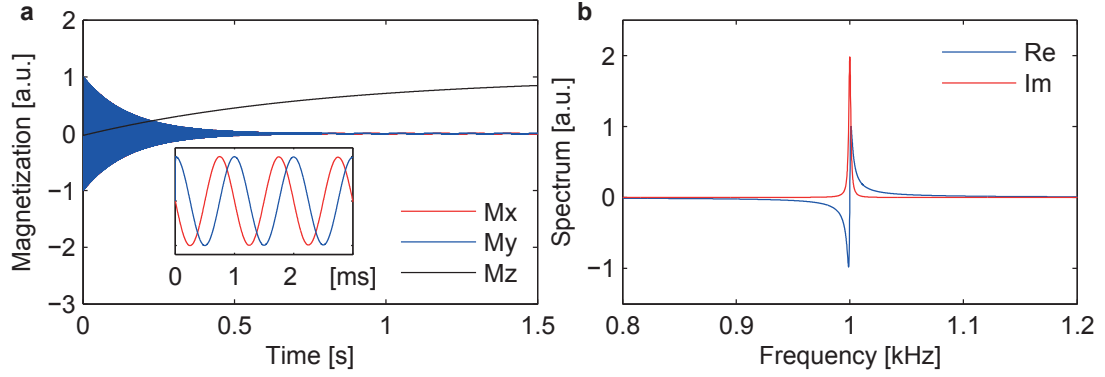


Figure 1.1: **Numerical example of Bloch equation solution.** (a) Time domain numerical solution of eq. (1.5) considering a Larmor frequency $\nu_0 = 1$ kHz, $T_2 = 150$ ms, $T_1 = 800$ ms. At time $t = 0$ a field $B_1 = 1$ mT is applied for a pulse length of $\tau = 5.9$ μ s so that the whole magnetization is rotated from \hat{z} into the \hat{x} - \hat{y} plane. (b) Fourier transform of the dynamic evolution of M_x and M_y .

In this thesis we use the so called inductive excitation/detection scheme. In this experimental frame an inductor is placed in proximity of the sample and the whole setup is merged in a static (strong) magnetic field B_0 . By applying RF signals across the inductor B_1 fields are generated (perpendicular to B_0) in pulses aimed at achieving the maximum deviation of the sample magnetization. When the excitation stops, the thermalisation of the magnetization is such that a voltage is induced in the inductor via Faraday's law. Such voltage is our observable, linearly related to M_x and M_y , it encodes the magnetization dynamics and it represents an opened window on the chemistry of the sample. Its amplitude can be computed by Faraday's law using the reciprocity principle and it is given by [3]:

$$s_0 = \omega_0 M_0 B_u V_s \sin(\theta) \quad (1.6)$$

where B_u is the so called unitary field of the coil projected in the \hat{x} - \hat{y} plane (the field produced by a current of 1 A flowing through the coil), ω_0 the Larmor frequency, V_s the sample volume, θ the nutation angle (the maximum signal is obtained for $\theta = \pi/2$), M_0 is given by eq. (1.2). If B_u is not homogeneous, the total signal can be easily computed with an integration of eq. (1.6) over the sample region by applying the superposition principle.

Many extensive and detailed descriptions of NMR and its applications can be found in books [4–7]. In this section we only want to briefly report the very few concepts and formulas needed for the subsequent chapters and describe the principles of the simplest NMR technique allowing for spectroscopy of bulk matter: the 1D pulsed experimental scheme and its combination with FFT. Much more refined techniques do exist, but they do not appear in this work. In this thesis we focus on the study and development of hardware, and in particular we show and

characterize broadband single-chip CMOS transceivers aimed at pulsed NMR operation. We show how such technology may be used for both the implementation of compact probes for applications such as NMR magnetometry, or open the way towards novel avenues such as the NMR spectroscopy at sub-nL volume scales, to date out of reach for the existing NMR instrumentation.

1.2 CMOS electronics in NMR tools: trends

Since their advent, CMOS technologies allowed for technology revolutions in fields such as communication, photography, and sensing. In recent years many advances have been proposed as well in the NMR research. Such developments rely on CMOS as enabler of novel technology in the attempt to expand the NMR applications portfolio. The CMOS-based innovations presented in the last two decades can be roughly separated into two sub-categories: on one side CMOS electronics is presented as the propelling element towards the aim of making portable NMR tools [8–20]. A second field of research pursues the aim of realizing NMR tools with high sensitivities (in terms of absolute spin number) and apply the power of NMR at exceedingly small volumes for applications in spectroscopy and microscopy [21–29]. In what follows we expand on these two different approaches, describing the main reasons that justify their developments.

CMOS for portable NMR tools

The search of portable NMR tools is justified by the need for simplification of the requirements and constraints that currently hinder a wide applicability of NMR-based biological/chemical assay. Small low-cost miniature NMR systems are claimed to be solutions for personalized medicine [8] and point of care stations aimed at early disease detection in remote areas [9]. One limitation of portable NMR tools is the strength of the magnetic field. Being based on permanent magnets, field strengths are typically below 1 T. In order to achieve the sensitivity necessary for biochemical assay, such weak static fields force the use of sample volumes of about 10 μL and labelling techniques. In this respect, the use of magnetic functionalized nanoparticles binding to molecular targets was demonstrated to have excellent performance. The sensing principle is based on the measurement of the relaxation time T_2 of the water in the biological fluid, where functionalized magnetic nanoparticles are introduced. The target molecules act as bridges clusterizing the nanoparticles, and consequently significantly affect the relaxation properties of water. Via relaxation measurements within this scheme portable NMR tools have been proved to sense pM concentrations of target molecules within 5 μL active volumes [10].

From the hardware point of view, relaxometry measurements are probably the ones that require less constraints to yield reliable results. Although the field homogeneity of portable fixed magnets can hinder high resolution spectroscopy, T_2 measurements in B_0 inhomogeneous fields can be obtained via spin-echoes [30]. The application of the modified spin-echoes

CPMG sequence [31] provides a solution to the often inhomogeneous B_1 that characterizes the excitation/detection coil, and defines the level of refinement needed in portable NMR tools.

Progressive developments used CMOS RF transceivers, that included pulse sequencers, to shrink an NMR relaxometer down to the size of a palm [8, 10–17]. Besides delivering the most compact NMR relaxometers, this research allowed for an in depth study of how CMOS transceivers and coils should be opportunely interfaced [16]. Further and more recent developments are moving towards the co-integration of transceivers with RF generators [18], ADCs [19], temperature-current driver loops to correct B_0 fluctuations and allow for long term averaging capabilities [9, 20].

CMOS probes for imaging and spectroscopy of mass limited samples: co-integration of coil and electronics

The problem of performing NMR-based studies of mass limited objects down to exceedingly small scales is a well known topic in the NMR community. The NMR signal s_0 is proportional to the sample volume V_s and to the unitary field of the detection coil B_u . Since the unitary field of a coil is inversely proportional to the dimension of the inductor, the optimal way to approach the NMR-based analysis of a mass limited sample (having a fixed volume) is to adapt the size of the detection coil to the sample [32]. The development of microcoils for mass limited NMR studies, their different topologies, the spin sensitivities achieved, and the advantages and trade-offs of each are better described in the following section. In this section we want to elucidate why CMOS technologies are particularly fit to deliver NMR probes oriented towards mass limited analysis and having an exceptional degree of versatility and performance. To this aim, we first describe the intrinsic advantages of this technology for the aim of reaching high sensitivities in small active volumes, and later report a literature survey on the topic.

Planar microcoils are one important type of coils that is well suited to be scaled towards microscopic dimensions (see below). In CMOS microchips, the use of planar inductors has a relevant role for the design of integrated units such as voltage controlled oscillators (VCOs). For this reason, integrated inductors were object of previous in-depth analysis and research [33]. With the aim of realizing NMR mass limited probes, the co-integration of electronics and planar microcoils has been reported in several scientific investigations. Thanks to the sub- μm features of CMOS, the coil realization and its connection to the RF electronics are realized with maximum grade of reproducibility and precision, allowing for eased implementations of micro-resonators [22–28] and multilayer microcoils [21, 34, 35].

A first advantage of this approach is the close proximity between the front-end amplification electronics and the detection coil, allowing for minimization of RF losses, parasitic capacitance and resistance, that would otherwise affect the SNR. However, an eventual loss in SNR is not the only problem related to cumbersome interconnections present between the NMR electronics and the active volume. As a matter of fact, the metal lines that connect the microcoil to passive elements and electronics constitute a parasitic circuit that is capable to sense (obviously in a non-optimal way) a certain active volume (different from the target one residing in close

proximity to the detection coil). Consequently, when packaging the NMR probe for use, one has to pay a high degree of attention to avoid that parasitic NMR signals, coming from the active region of the parasitic interconnection circuit, contribute in a significant way in the data retrieved. This particular issue is more and more dramatic as the active volume of the detection coil decreases and as the averaging time required to perform the experiment increases: both cases approach the situation where any material around the probe head is likely to induce problems in the experimental phase. On the other hand, when microcoils are co-integrated on a CMOS chip together with the RF electronics, the parasitic circuit due to interconnections practically disappears and the ^1H NMR background is null even for long averaging times (the technology itself does not contain ^1H nuclei if not in eventual atomic sporadic defects). Fig. 1.2 illustrates the concept by comparing two different realizations of compact probes aimed at sensing sub-nL active volumes. Fig. 1.2a shows a combination of a single-chip transceiver and a Bruker SU8-embedded copper planar microcoil, where the small size of electronics and active volume is obscured by the interconnections. The shaded rectangle indicates the area where the interconnections form a parasitic detection coil. Fig. 1.2b shows a fully integrated CMOS approach, which delivers a ultra-compact device with an improved degree of versatility. Other advantages that are intrinsically related to the use of CMOS technologies are the possibility of both eased implementation of arrayed and multichannel instruments and the reduction of production costs in the long term.

A first fully integrated NMR probe was presented for magnetometry purposes: the idea was to obtain a ultra-compact device capable to perform magnetic measurements with a high spatial resolution (≈ 1 mm). In this contribution the excitation was performed by an off-chip electronics via an integrated excitation coil, inductively decoupled from the detection coil which was connected to a receiver-only on-chip electronics [29]. In the subsequent years, the research of receiver-only CMOS microchips assumed a more general interest [22–28, 36–40]. Receiver-only CMOS probes, where low noise amplification electronics was buried below integrated microcoils, were extensively studied in relation to microscopy purposes [22–28] and proposed as optimal choice for applications such as the implementation of parallel imaging arrays aimed at obtaining high spatial resolution on a large sensitive area [26] and probes for surgical guidance [27]. Other MRI-related applications that employ CMOS receiver-only chips (without integrated coils) are the realization of wireless implanatable detection systems to locally improve the SNR [40] and the eased multiplexing in phased arrays [39]. Overall, these efforts allowed for a comprehensive understanding and refinement of the techniques used to realize a CMOS low-noise front-end receiver for a NMR probe.

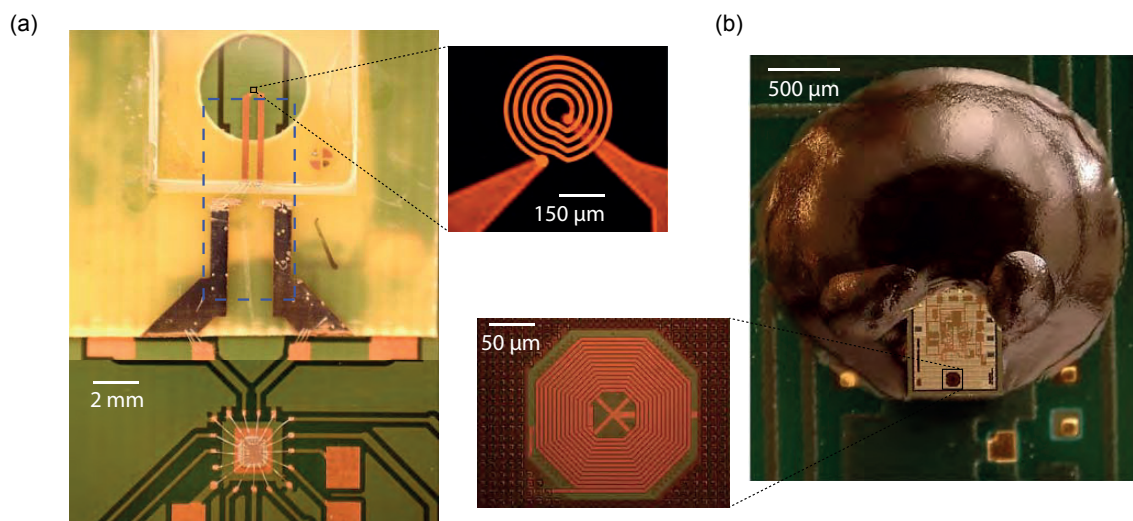


Figure 1.2: **Sub-nL probes employing external VS integrated coils.** (a) Photograph of a 1 nL probe based on a Bruker SU8-embedded copper microcoil. The microcoil is realized on a glass substrate and connected to a PCB that implements the resonant circuit connections. In this probe, the whole electronics is contained on a single-chip CMOS transceiver. Despite the small size of the active volume and electronics (see figure and inset), the necessary interconnections required to match and tune the microcoil occupy a significant amount of space. The shaded rectangle indicates the region where these interconnections form a parasitic detection coil. (b) Photograph of an ultra-compact NMR probe where a single-chip transceiver is co-integrated on the same chip with a multilayer non-resonant microcoil. In this case, thanks to the very close proximity of the differential interconnections that link the coil to the amplification stage (the metals are 4 μm wide and 1 μm distant) there is no parasitic detection. Moreover, the overall size of the system is well comparable to the sensitive region itself.

CMOS-based probes in this thesis and their aims

My PhD project was within the KTI/CTI frame which funds close collaborations between Swiss companies and universities. Our industrial partner in this project was Metrolab SA, a company based in Geneva and specialized in magnetometry instrumentation. The initial aim of the PhD project was to implement CMOS broadband electronics for use in pulsed NMR-based teslameters that operate at frequencies covering the entire range of existing fields (^1H frequencies range from 1 MHz to 1 GHz). The realization of the first transceivers, as explained above, was initially implemented to realize portable NMR relaxometers [12, 13, 18]. Based on these few contributions, we have developed on top of the previous know-how concerning the integration of receiver channels and delivered multiple fully functional NMR CMOS single-chip transceiver architectures. The technical details of the design of this instrument are fully explained in Chapters 2, 3 and 5.

In a nutshell, the single-chip transceiver can be interfaced with on-chip integrated microcoils or external LC resonators and it is tested experimentally in a frequency range from 3 MHz to 300 MHz. The dimension of the chip is about 1 mm^2 , and it consists of a radio-frequency

(RF) power amplifier, a low-noise RF preamplifier, a frequency mixer, an audio-frequency (AF) amplifier, and fully integrated transmit-receive switches. The initial interest in this technology was to provide a functional integrated broadband electronics to Metrolab and show full compatibility to their pulsed teslameter units. For magnetometry purposes the single-chip transceiver is interfaced with external resonators: results of both multi-nuclear spectroscopy and high field magnetometry using standard high resolution micro-solenoids and standard probe heads for magnetometry are contained in Chapters 2 and 3 respectively. Coherently with what described above, CMOS transceivers resulted effective in delivering compact, versatile, trade-off free probes for both applications. Metrolab SA has already invested on this technology and aims at integrating CMOS single-chip transceivers in their commercial products. Besides the implementation of compact probes, in this thesis it is introduced the concept of ultra-compact NMR probe, where the co-integration of a transceiver together with a multi-layer CMOS microcoil simultaneously allows for high sensitivities in sub-nL active volumes together with an exceptional degree of versatility and miniaturization in the resulting probe. Fig. 1.2b shows a ultra-compact NMR probe. With an integrated coil of about 150 μm external diameter, a ^1H spin sensitivity of about $1.5 \cdot 10^{13}$ spins/Hz $^{1/2}$ is achieved at 7 T. The calibration of the sensor is discussed in Chapter 2, while the very first consistent study of NMR spectroscopy of sub-nL biological entities (ova of microorganisms) is presented in Chapter 4. In the following section we try to summarize on the spin sensitivity previously achieved with inductive approaches dedicated to small active volumes. As a result of this analysis, it appears convincing that CMOS ultra-compact NMR probes deliver high-sensitivity performance at the sub-nL scale, in absolute values comparable to the most sensitive approaches experimentally reported, but with practical and crucial advantages. In all likelihood, CMOS ultra-compact devices represent the best option to achieve sub-nL NMR assays as well as simultaneous arrayed operation within a single magnet.

1.3 Sensitivity of mass-limited NMR probes

As anticipated in the previous section, the problem of performing NMR spectroscopy on mass limited objects is well known in the NMR community. Indeed, NMR suffers from an intrinsic low sensitivity (mainly due to the relatively low operational frequencies) that hinders significantly the application of the technique to microscopic objects. Despite this disadvantage, NMR is still considered one of the most powerful spectroscopic techniques, thanks to both its resolving power and its bio-compatible non-invasivity. For this reason, in the past decades, many efforts and many research groups have sought solutions to the problem of mass-limited NMR by proposing multiple probe designs at progressively small volume scale [21, 23, 41–45, 45–60].

In this section we want to describe the most significant approaches that have been reported in the recent literature with the aim of implementing NMR probes dedicated to mass limited samples. As anticipated above, by referenced comparisons we will show that CMOS ultra-compact devices are probably the best option for the development of NMR tools at sub-nL

Chapter 1. Introduction

volumes. First we will make considerations on the signal-to-noise ratio (SNR) and sensitivity of a generic NMR detector. Later, we will present a short review of the approaches that have been previously developed, and compare their performance.

SNR considerations

We can write with good approximation the time-domain NMR signal as follows:

$$S(t) = (s_0 e^{-\frac{t}{T_2^*}} e^{-i\omega_0 t} + n(t)) \cdot e^{-\frac{t}{T_m}} \quad (1.7)$$

where s_0 is the signal amplitude, T_2^* the effective relaxation time (resulting from a combination of field inhomogeneities and dipolar interactions), T_m the decay time of the applied exponential filter, ω_0 the Larmor frequency expressed in rad/s, $n(t)$ the noise contribution. The aim of this discussion is to determine relations, assuming the validity of eq. (1.7), between the SNR in time and frequency domain and the limit of detection (LOD) of a sensor.

First, we consider the noise fluctuations in both the time and frequency domains. Assuming that the sensor is affected by white noise (a good approximation if the detection is performed far from the $1/f$ region) we can write the time domain root mean squared (RMS) as:

$$\bar{n}_t \equiv \left\{ \frac{1}{T} \int_0^T n^2(t) dt \right\}^{1/2} \quad (1.8)$$

where T is the acquisition time. \bar{n}_t is expressed in Volts and it can be directly measured in the time domain. In order to write down the frequency domain noise we consider the assumption of having white noise at our source: this is justified by the fact that the physical noise of the detector is due to a resistor, and that it is therefore expressed as [61]:

$$\bar{n}_t = n_{sd} \sqrt{F} \quad (1.9)$$

where n_{sd} represents the noise spectral density [V/Hz^{1/2}] and F the detection bandwidth. The noise spectral density is, in generic terms, the physically fixed quantity in the system. For the resistive case we would have the well known expression $n_{sd} = \sqrt{4k_B T R}$. Eq. (1.9) expresses the fact that with a larger bandwidth we acquire more frequencies that equally contribute to the time domain noise RMS. In a similar intuitive way one can write the RMS noise in the

frequency domain:

$$\bar{n}_f = n_{sd} \sqrt{T} \quad (1.10)$$

where T is the acquisition time. In terms of a more rigorous mathematical definition, the RMS shown in eq. (1.10) can be defined in the frequency domain and then treated with the Parseval's identity:

$$\bar{n}_f \equiv \left\{ \frac{1}{F} \int_0^F n^2(f) df \right\}^{1/2} = \left\{ \frac{1}{F} \int_0^T n^2(t) dt \right\}^{1/2} = \frac{\sqrt{T} \bar{n}_t}{\sqrt{F}} = \sqrt{T} n_{sd} \quad (1.11)$$

We note that eq. (1.11) simply corresponds to the FFT of the function $n^2(t)$ at a frequency $\nu = 0$. By assumption of white noise, in fact, we stated that $\bar{n}_f = \bar{n}(\nu) = \bar{n}(\nu') \quad \forall \nu, \nu' \in [0, F]$. In eq. (1.11) the quantity is easily computed thanks to the convenient choice of $\nu = 0$. The factor $1/F$, on the other hand, correctly normalizes over the number of data points and restores the correct dimensions.

NMR signals are typically filtered by exponentially decaying functions, as implicit in eq. (1.7). This operation equally affects the noise and in particular the RMS \bar{n}_f :

$$\bar{n}_f = \left\{ \frac{1}{F} \int_0^T n^2(t) e^{-\frac{2t}{T_m}} dt \right\}^{1/2} = n_{sd} \sqrt{\frac{T_m}{2} (1 - e^{-\frac{2T}{T_m}})} \quad (1.12)$$

Eq. (1.12), fully derived in Appendix A, describes the link between frequency RMS and noise spectral density. Via eq. (1.9) the ultimate link to the time domain noise is therefore possible. From eq. (1.7) we can proceed to the analysis of the FFT of the time domain signal:

$$S(\nu) = \int_0^T s_0 e^{-t(\frac{1}{T_2} + \frac{1}{T_m})} e^{-i2\pi\nu t} dt \quad (1.13)$$

where ν is introduced as frequency deviation from the Larmor value. In simpler terms, $S(0)$ corresponds to the FFT contribution at the Larmor frequency. By solving eq. (1.13) in more

generic notations and for the real part only we find:

$$\begin{aligned}
 S(\nu) &= s_0 \int_0^T e^{-\frac{t}{\tau^*}} \cos(\omega t) dt \\
 &= s_0 \frac{\tau^*}{1 + (\omega\tau^*)^2} - s_0 \left\{ \left(\frac{\tau^*}{1 + (\omega\tau^*)^2} \right) \cos(\omega T) e^{-\frac{T}{\tau^*}} + \left[\frac{\omega(\tau^*)^2}{1 + (\omega\tau^*)^2} \right] \sin(\omega T) e^{-\frac{T}{\tau^*}} \right\}
 \end{aligned} \tag{1.14}$$

where $\omega \equiv 2\pi\nu$ and $\tau^* \equiv \frac{T_2^* T_m}{T_2^* + T_m}$. The peak value of equation (1.14) is, as expected, at $\nu = 0$:

$$S(\nu = 0) = S_{max} = \frac{s_0 T_2^* T_m}{T_2^* + T_m} \left[1 - e^{-T(\frac{1}{T_2^*} + \frac{1}{T_m})} \right] \tag{1.15}$$

By combining eqs. (1.14) and (1.12) one can finally write the SNR in the frequency domain:

$$SNR_f = \frac{s_0 T_2^* T_m}{T_2^* + T_m} \frac{1 - e^{-T(\frac{1}{T_2^*} + \frac{1}{T_m})}}{n_{sd} \sqrt{\frac{T_m}{2} (1 - e^{-\frac{2T}{T_m}})}} \tag{1.16}$$

In accordance to Refs. [4, 62] the sensitivity of the detector is maximized for $T_2^* = T_m$. For this reason such condition is always adopted as a criterion in NMR data processing. It is worth to note at this point that, thanks to action of the matched filter (as it is commonly called the exponential filter described above) the contribution of noise is exponentially dumped during the acquisition. As a consequence, the acquisition time T affects the SNR only slightly. In order to produce more friendly expressions we can consider the situation in which $T \gg T_m = T_2^*$ by computing the $T \rightarrow \infty$ limit in eqs. (1.14) and (1.12). As result we find the following expressions for, respectively, the real part of the signal FFT $S(\nu)$ and the frequency RMS of the noise \bar{n}_f :

$$S(\nu) = s_0 \frac{2/T_2^*}{(2/T_2^*)^2 + (2\pi\nu)^2} \tag{1.17}$$

$$\bar{n}_f = n_{sd} \sqrt{\frac{T_2^*}{2}} \tag{1.18}$$

In eqs. (1.17) and (1.18) T_m was replaced by T_2^* . It is worth to note that eq. (1.17) corresponds to the well known Lorentzian function, in this case having a peak centred at the Larmor

frequency. When looking at NMR spectra, it is often relevant to look at the spectral width. One main parameter commonly used to evaluate this spectral feature is the full width at half maximum (FWHM). From equation (1.17) we find that for the NMR signal the FWHM $\Delta\nu$ is:

$$\Delta\nu = \frac{1}{\pi T_2^*} \quad (1.19)$$

Eq. (1.19) represents a measure of the frequency range over which the NMR signal power is distributed. Obviously, the larger this frequency range and the lower the resulting SNR from a fixed signal power. This intuitive law is confirmed by eq. (1.16), whose $T \rightarrow \infty$ limit becomes:

$$SNR_f = \frac{s_0}{n_{sd}} \sqrt{\frac{T_2^*}{2}} \quad (1.20)$$

Since NMR analysis is more powerful and versatile by frequency-domain visualization, eq. (1.20) is much more central and useful with respect to its time domain counterpart.

Sensitivity and LOD

The limit of detection (LOD) is an important parameter that expresses the effective minimum quantity of a target compound detectable with a given NMR probe. Throughout this thesis NMR LOD and sensitivity statements mainly concern the detection of ^1H nuclei, but they can in general be expressed for all nuclear species. Before defining LOD and sensitivity the nuclear species should always be specified. Sometimes the literature offers statements of sensitivity and LOD that are related to some complex molecule: this approach can be better generalized by reporting LOD and sensitivity per unit nucleus (or spin). The relation between the two clearly resides in the multiplicity of the target nucleus in the target molecule. In order to simplify the treatment we will consider LODs and sensitivities as related to nuclei (or spins). The definition of LOD is straightforward: assuming that eq. (1.20) describes the SNR obtained in an NMR experiment where N_{spins} are sensed, the LOD expressed in terms of $\#spins$ can be conveniently defined as:

$$LOD_{\#} = \frac{N_{spins}}{SNR_f} = \frac{\sqrt{2}N_{spins}n_{sd}}{s_0\sqrt{T_2^*}} \quad (1.21)$$

Eq. (1.21) is often multiplied by 3 in the literature in order to indicate the $\#spins$ that is visible with an SNR of 3. However, in this treatment, we neglect this optional factor to maintain a

more uniform notation in all equations, and thus define the LOD as the $\#spins$ that yields an SNR of 1. From eq. (1.21) we note that $LOD_{\#}$ is a dimensionless quantity, and that it relates to a single NMR experiment where a single free-induction decay is analysed. In spectroscopy it is also interesting to state the LOD in such a way that it includes information about the experimental time needed to perform the detection. As discussed in Chapter 2 the most used NMR detection frame is the pulsed scheme, where N_{exp} experiments are successively performed with a repetition time T_R . Clearly, by averaging the spectra obtained in each single experience one can improve the SNR of the experiment by a factor $\sqrt{N_{exp}}$ in a time $T_{exp} = N_{exp} T_R$. As we can see, the SNR (and thus the $LOD_{\#}$) of an NMR experiment have a $\sqrt{\quad}$ dependence on the experimental time. By seeking the amount of spins that are detected in the experimental time T_{exp} :

$$LOD_{\#}(T_{exp}) = \frac{LOD_{\#}}{\sqrt{N_{exp}}} = LOD_{\#} \sqrt{\frac{T_R}{T_{exp}}} \quad (1.22)$$

From eq. (1.22) it is straightforward to identify the function that, independently from T_{exp} , expresses the capability of detection of the sensor in terms of LOD over time:

$$LOD = LOD_{\#} \sqrt{T_R} = \frac{\sqrt{2} N_{spins} n_{sd} \sqrt{T_R}}{s_0 \sqrt{T_2^*}} \quad (1.23)$$

Equation (1.23) is the definition of LOD typically used in NMR spectroscopy and it has dimensions of $\#spins/\sqrt{Hz}$. In this definition, the added dimension \sqrt{Hz} refers to the real experimental time and its influence on the performance. From eqs. (1.23) and (1.22) the relation relating the LOD to the effective number of spins detected after a given experimental time is correctly deduced as $LOD_{\#}(T_{exp}) = LOD/\sqrt{T_{exp}}$.

Despite its widespread use, the LOD is objectively not the best way to characterize an NMR sensor itself. This is readily visible in eq. (1.23), where the LOD is shown to depend on T_R and T_2^* , which are both parameters that ultimately depend on the sample nature and/or on the field distortions present in the sensitive region of the detector. Therefore the LOD can be used as optimal parameter only to express the capability of detection of a target compound at a given spectral resolution, but it results uncomfortable to express, independently from the sample nature and the spectral resolution, the ability of the sensor itself to detect spins. In order to better convince the reader that such performance parameter (that we can call "spin sensitivity" or N_{min}) is a more comfortable and unambiguous way to describe the sensing power of a detector, we might go back to the sensor of Fig. 1.2b and ask what is its performance. Throughout my course we have measured with this same sensor liquid samples having $T_2^* \simeq 100$ ms, biological cells exhibiting $T_2^* \simeq 5 - 10$ ms, solid samples having T_2^* in a range

from 30 μs to 2 ms. Clearly, the experimental LOD changes in each situation. In order to solve this issue it is sufficient to define N_{min} in such a way that all the dependences from sample nature and linewidth are eliminated. Later, the relationship between N_{min} and LOD can serve to compute the effective amount of spins detected in a given experiment. By going backwards in the above discussion one realizes that the spin sensitivity of the detector can be best defined by eliminating the dependence on T_2^* in eq. (1.20):

$$N_{min} = \frac{N_{spins} n_{sd}}{s_0} \quad (1.24)$$

where the physical dimensions are $\#spins/\sqrt{\text{Hz}}$. It is worth to note, however, that the meaning of the $\sqrt{\text{Hz}}$ dimension in (1.24) and (1.23) are different from each other. In eq. (1.23) it is referred to the experimental time, while in eq. (1.24) it refers to the linewidth of the NMR signal. The relation between the spin sensitivity and the LOD is easily found to be:

$$\text{LOD} = N_{min} \sqrt{\frac{2T_R}{T_2^*}} \quad (1.25)$$

In NMR experiments at high field it is often true that repetitions times T_R are in the order of 1 s. In this peculiar case one finds a straightforward relation between the LOD and the spin sensitivity expressed in function of the linewidth $\Delta\nu$:

$$\text{LOD} \simeq N_{min} \sqrt{2\pi\Delta\nu \cdot [s]} \quad (1.26)$$

Sensitivity of mass limited NMR probes

Table 1.1 shows a collection of referenced performance of mass-limited NMR probes normalized at 600 MHz following the criteria as in Ref. [63]. The production of this table is partially inspired by Ref. [63] and the values reported, hopefully minimizing the human errors, should be taken with caution (although safely as a good approximation of reality). In order to evaluate and compare the different approaches for the implementation of a mass-limited NMR probe we reported as main information: (1) sample volume V_s ; (2) Linewidth (in ppb and Hz); (3) LOD and sensitivity. The main parameter that can be used for a first classification of the probe is, of course, the sample volume. In table 1.1 we have classified the probes by volume and considered approaches aimed at active volumes smaller than the $\approx\mu\text{L}$. In what follows we try to summarize more in depth the advantages and disadvantages of the three class of topologies that are commonly used to make inductive NMR probes: planar, solenoidal, and stripline

Chapter 1. Introduction

(microslot). Despite on this same topic there are already extensive reviews [32, 64], these are not comprehensive of the most recent contributions.

Sensitivity of mass-limited NMR probes

≈μL probes					
Topology and Ref.	V_s [nL]	Linewidth [ppb]	Linewidth [Hz]	LOD [nmol/ $\sqrt{\text{Hz}}$]	N_{min} [#spins/ $\sqrt{\text{Hz}}$]
Planar-Helmoltz [41]	8000	20	12	800	$5.5 \cdot 10^{16}$
Stripline [42]	2000	6	3.6	1.57	$2 \cdot 10^{14}$
Planar [43]	900	13.5	8.1	21	$1.8 \cdot 10^{15}$
Phased Array [44]	520	11	6.6	7500	$7 \cdot 10^{17}$
Planar [45]	470	300	180	40	$7 \cdot 10^{14}$
Planar [46]	390	15	9	230	$1.8 \cdot 10^{16}$
Solenoid [47]	315				$4 \cdot 10^{13}$
100 – 300 nL probes					
Planar [48]	200	400	240	15	$2.3 \cdot 10^{14}$
Planar [49]	160	70	42	4	$1.5 \cdot 10^{14}$
Solenoid [50]	130	6	3.6	2	$2.5 \cdot 10^{14}$
Solenoid [51]	125	1700	1000	16.5	$1.2 \cdot 10^{14}$
Stripline [52]	125	80	48	18	$6.2 \cdot 10^{14}$
Solenoid (this thesis) [21]	100				$6 \cdot 10^{13}$
30 – 1 nL probes					
Microslot [53]	30	1.8	1.1	1.4	$3.2 \cdot 10^{14}$
Planar [45]	30	300	180	3	$5.3 \cdot 10^{13}$
Planar CMOS [23]	15				$9 \cdot 10^{12}$
Solenoid [54]	15	74	44	0.1	$3.6 \cdot 10^{12}$
Microslot [55]	10	7.2	4.3	0.1	$1.15 \cdot 10^{13}$
Solenoid [56]	7	2.3	1.4	0.8	$1.6 \cdot 10^{14}$
Solenoid [57]	5	2	1.2	0.1	$2.8 \cdot 10^{13}$
sub-nL probes					
Planar [58]	1	6	3.6	5	$6.3 \cdot 10^{14}$
Planar CMOS (this thesis) [21]	0.2				$4.5 \cdot 10^{12}$
Solenoid ($\phi = 100 \mu\text{m}$) [59]	0.03				$7 \cdot 10^{12}$
Solenoid ($\phi = 20 \mu\text{m}$) [59]	0.1				$2 \cdot 10^{12}$
Solenoid ($\phi = 100 \mu\text{m}$) [60]	0.03				$5 \cdot 10^{12}$
Solenoid ($\phi = 20 \mu\text{m}$) [60]	0.1				$3 \cdot 10^{12}$

Table 1.1: Performance and topology of reported mass limited NMR probes. V_s is the sample volume, used as main parameter to classify the different probes. LOD and N_{min} are reported accordingly to the the discussion presented above and normalized at 600 MHz.

Stripline and Microslot

Since their first appearance [52] stripline probes have raised a large interest in the NMR community. The idea behind this probe topology is to implement a high quality factor resonator using standard circuit microfabrication processes (PCB-like) and employ, as NMR excitation/detection element, a strip embedded in the self-resonating circuit. In terms of spectroscopy performance the stripline approach has some intrinsic advantage linked to its geometry. First, the sample chamber is often made by a cavity that separates the sensing strip from ground planes. As explained in [52, 65] such configuration allows for an homogeneous excitation field B_1 . A second advantage of this geometry is the minimized amount of susceptibility mismatch surfaces that cross the field direction. This leads to a sample chamber where minimal field distortions, having relatively predictable geometries, can be shimmed to obtain spectral resolutions in the order of 1 ppb [66, 67]. A third advantage is the high degree of integration of stripline probes with microfluidics within the embedded multistep fabrication process [42, 66, 67].

As shown in Table 1.1 stripline probes can perform very well on sample volumes of $\approx 1 \mu\text{L}$, making them a first choice at this particular volume range: despite solenoidal probes may give an higher spin sensitivity, stripline probes take advantage of the high spectral resolution to boost the LOD and ultimately deliver more versatility for probe fabrication and integration with fluidics. One drawback of this approach is, however, its scarce scalability towards smaller probe size and sample volume: this is due to the fact that the self-resonating circuit has pretty much a fixed dimension determined by the working frequency. At NMR frequencies, stripline probes are typically cm-sized objects.

Microslot probes practically represent the downscaled implementation of the stripline approach. In this topology a high quality factor resonator is implemented with a combination of metal routing (creating large inductance) and lumped capacitors, and a restricted strip embedded in the routing is used as excitation/detection element. A hole in the excitation/detection strip acts as sample chamber: this particular feature gives origin to the term microslot. Although microslot approaches are capable of delivering high sensitivities on volumes ranging from 10 to 30 nL, they do not give evident advantages with respect to the other approaches at the same scale (see Table 1.1). Their major drawback is the large discrepancy between the probe size and the active volume as well as a not too favourable sample handling geometry.

Solenoidal Probes

The solenoidal topology is often indicated, by most NMR scientists, as the most successful in delivering the best NMR sensing capability. Indeed, the main intrinsic advantage of the solenoidal topology is that it represents a well optimized way to produce a strong magnetic field into a space region by using a conductive wire. Thanks to the relatively high inductance generated in this topology, solenoids can be properly tuned and matched in LRC resonators having relatively high quality factors. This is why it was possible to report solenoidal NMR setups down to progressively small active volumes (reaching the 100 pL range).

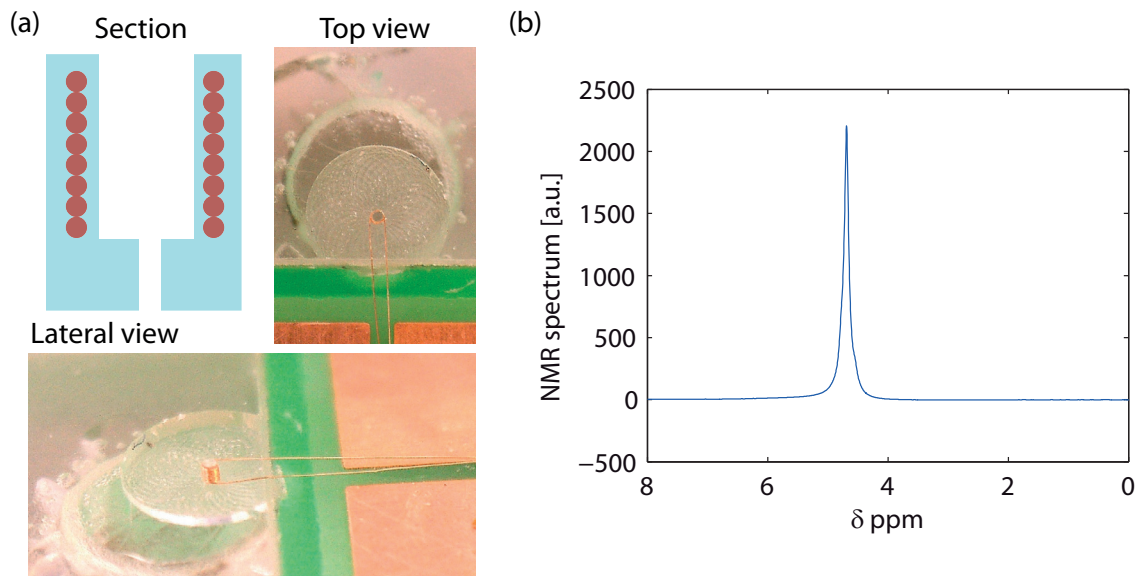


Figure 1.3: **PMMA-embedded copper microsolenoids.** (a) Section schematics: copper wires are indicated in brown and PMMA is indicated in light blue. The hole within the solenoid hosts the sample. A narrower hole connects the sample chamber to a reservoir via a microchannel. Photographs in top and lateral view show the microsolenoid at an intermediate step of the probe fabrication. The copper wire, manipulated with a wire bonder, has a diameter of $20\ \mu\text{m}$. The inner diameter of the solenoid is about $170\ \mu\text{m}$. After soldering of the solenoid to a PCB, PMMA is cast around its structure for susceptibility matching. Later, the sample chamber and the microchannel are obtained via milling with an excimer UV laser. (b) NMR spectrum of about 2 nL of water after 100 averaged scans at $\tau_{\pi/2}$ pulses with $T_R = 2\ \text{s}$.

Table 1.1 shows that solenoids always seem to be the best option if we look at the spin sensitivity: this is linked to the fact that, by producing higher magnetic fields in the sample region, higher NMR signals and thus higher sensitivities follow. However, by a more careful inspection of table 1.1, one may realize that solenoids do not always outperform their alternatives (particularly at small active volumes).

The main disadvantage of the solenoidal topology is intrinsically related to its geometry. The sample chamber is constituted by the cavity confined by the wire loops and it must be oriented perpendicularly to the external static field B_0 in order to perform an NMR experiment (the B_1 field has to be perpendicular to B_0). In this forced configuration, susceptibility mismatch surfaces (present at the surfaces in proximity of the conductor) often make life hard to the experimenter. Indeed, solenoidal setups generally require non-trivial susceptibility matching strategies in order to deliver satisfactory linewidths. The most widespread strategy is to embed to solenoid in a susceptibility matching medium (which can be a fluid or a cast polymer as shown respectively in Chapters 2 and 3) [57, 68]. Even though susceptibility matching strategies help in improving the performance of solenoidal setups, it is known that: (1) in

1.3. Sensitivity of mass-limited NMR probes

order to obtain narrow linewidths the filling factor of the solenoid should be reduced to about 35% at expense of the spin sensitivity (due to the use of a larger coil diameter) [69]; (2) the operation is more and more complicated as the sample volume (and coil size) become smaller. As shown in table 1.1, solenoids maintaining high spin sensitivities and spectral resolutions were successfully reported at a volume scale of 100 nL [50] and 5 nL [57]. However, already at 5 nL sample volumes, the spin sensitivity of a high resolution probe is smaller than, e.g., the one obtained by planar CMOS and microslot probes. On the other hand the solenoidal probe reported in [54], which reports the highest spin sensitivity in the 10 nL volume region, is affected by a relatively large linewidth (on samples in their liquid state). These trends reflect the trade-off between resolution and sensitivity characterizing solenoidal probes.

During the course of my PhD we could experimentally prove other major drawbacks of the solenoidal approach when its aim is the analysis of sub-nL samples via NMR spectroscopy. For this same aim a NMR probe should exhibit, besides a high spin sensitivity, high versatility in terms of sample manipulation and high control of background signals (sub-nL NMR spectroscopy obviously requires long time averaging). Recent contributions describe the systematic and reproducible fabrication of micro-solenoids via wire bonding [68, 70]. Inspired by these techniques, we have implemented miniaturized hollow PMMA-embedded copper microsolenoids whose cross section is described in fig. 1.3a. The idea was to beat the performance of the probe shown in Fig. 1.2b, particularly for the aim of performing spectroscopy of sub-nL ova (see Chapter 4). Fig. 1.3a also shows photographs at an intermediate step during the fabrication of the probe. At the end of the fabrication (i.e., after wire soldering, PMMA casting, microdrilling via UV laser and packaging) it was possible to obtain PMMA-embedded copper microsolenoids and test their use in comparison to the CMOS planar probe. Fig. 1.3b shows a measurement on water, where a spin sensitivity of about $2 \cdot 10^{13}$ spins/ $\sqrt{\text{Hz}}$ was obtained together with a linewidth of about 30 Hz (coherently with what previously shown over sample volumes of 10 nL in very similar conditions [68]). However, this approach has shown huge flaws for spectroscopy purposes over long averaging times. The combination of the presence of a parasitic sensitive region (as in Fig. 1.2a), the need of a liquid environment for the sample, the unfavourable geometry of susceptibility mismatches (exasperated at this scale), and the necessary use of different materials (even though matched in susceptibility [71]) yielded NMR performance unfit for scopes other than the spectroscopy of high spin concentrations in the liquid state (at water susceptibility). First, over long times, background signals in the order of 1/1000 of the water peak are visible and unstable (attributed to water infiltration around the sensitive volume and/or in the materials within the parasitic active volume). Second, upon insertion of samples unmatched with water the resulting field distortions were unshimmable due to their small scale and not reproducible. The sum of these problems greatly reduces the utility of solenoidal setups at the sub-nL scale, especially for scopes such as the analysis of sub-nL biological samples.

Overall, solenoidal setups may be regarded as optimal choice for volume sizes of 100 – 300 nL, and as valid alternative down to about the 10 nL range (with drawbacks in terms of versatility). As it can be seen from table 1.1, at sub-nL scales solenoidal setups do not show a great advantage in terms of sensitivity and their drawbacks are exasperated as described above.

Planar Probes

The planar topology essentially consists in making the excitation/detection inductor with metals routing on a surface. Planar coils can be obtained via standard microfabrication processes such as electroplating on glass substrates. The conductor is generally shaped in a spiral way and the contacts to the external circuitry typically require at least a second level of metallization, being one extremity of the spiral in the inner side. By approaching the sample to the surface of the inductor NMR experiments can be conducted with the static magnetic field oriented parallel to the coil surface.

The planar topology and the resulting probe geometry have advantages and disadvantages that are complementary to the ones belonging to striplines and solenoids. On one side the minimum amount of mismatch surfaces perpendicular to the static field makes planar probes suitable for high resolutions without too complicated susceptibility matching strategies (comparably to striplines, and in advantage with respect to solenoids). On the other hand, the spiral form given by nested loops of different diameter typically yields a B_1 excitation field which is more inhomogeneous with respect to both solenoids and striplines. Consequently, applications where B_1 homogeneity is crucial can be possible only accepting small filling factors (at expense of sensitivity). One advantage that characterizes planar microcoils is their scalability over a large range of scales at practically no expense in terms of versatility and resolution performance (contrarily to the solenoidal case).

As shown in table 1.1 the performance shown by planar microcoils tend to improve together with their miniaturization. If at $\approx 1 \mu\text{L}$ volumes they are outperformed by the alternative approaches, at volumes of 100 – 300 nL they start to represent a valid alternative. At volume scales below the 30 nL, thanks to the extreme level of integration of CMOS technologies, planar CMOS microcoils deliver state of art sensitivity and LOD. Finally, thanks to the multilayer properties of CMOS, multilayer and non-resonant planar CMOS microcoils are shown (in this thesis work) to deliver state of art sensitivity and LOD at the sub-nL scale. Due to their basically trade-off free employment at these volumes they represent the most favourable choice in the sub-nL volume region, where the only alternative is the solenoidal approach (competitive in terms of sensitivity, but outperformed under all aspects in what concerns practical versatility). A last and crucial advantage of CMOS planar coils is, as already extensively explained in the previous section, the possibility to integrate them into ultra-compact devices. As more evident in Chapter 4, such devices deliver an unprecedented degree of versatility at the sub-nL scale together with state of art sensitivity. The combination of these facts is the reason why a first extensive NMR spectroscopy study of individual static sub-nL biological sample was enabled.

2 A broadband single-chip transceiver for multi-nuclear NMR probes

2.1 Abstract

In this chapter we describe a broadband complementary metal-oxide semiconductor (CMOS) single-chip transceiver suitable for pulsed nuclear magnetic resonance (NMR). The single-chip transceiver can be interfaced with on-chip integrated microcoils or external LC resonators and operates in the range from 1 MHz to 1 GHz. The dimension of the chip is about 1 mm^2 , and it consists of a radio-frequency (RF) power amplifier, a low-noise RF preamplifier, a frequency mixer, an audio-frequency (AF) amplifier, and fully integrated transmit-receive switches. In order to validate its broadband use, we show experiments of multi-nuclear NMR spectroscopy. When the probe employs an external resonant micro-solenoid having an active volume of 100 nL, the sensitivity on a sample of 7 M NaBF_4 in H_2O is sufficient to achieve a good SNR down to the Na Larmor frequency.

Besides the implementation of compact probes using standard high resolution micro-solenoids, within this chapter it is introduced the concept of ultra-compact NMR probe, where the co-integration of a transceiver together with a multilayer CMOS microcoil simultaneously allows for high sensitivities in sub-nL active volumes and an exceptional degree of versatility in the resulting probe. With an integrated coil of about $150 \mu\text{m}$ external diameter, a ^1H spin sensitivity of about $1.5 \cdot 10^{13}$ spins/ $\text{Hz}^{1/2}$ is achieved at 7 T. we were able to perform NMR spectroscopy of solid and static samples in volume ranges of 100 – 300 pL. Measurements on NH_4PF_6 (ammonium hexafluorophosphate) and cis-polyisoprene served as calibration of the sensor.

2.2 Introduction

NMR techniques are widely employed in chemistry, physics, biology, medicine, and material science for a large variety of studies [5, 72, 73]. Although diffused and very powerful, costs

This chapter is a minor variation of the publication "A broadband single-chip transceiver for multi-nuclear NMR probes" [21].

and dimensions of the necessary instrumentation limit its use, making of it a last resort for those cases where cheaper techniques are not available. In principle, the use of low-cost NMR spectrometers and imagers can reach a huge number of applications: from real-time diagnostics (e.g. on skin, biological samples or tendons) [10, 11, 74] to quality control of various products (e.g. elastomers or olive oils) [75, 76]. In the last few years, low-cost NMR systems were proposed on the market in the attempt of fulfilling these needs [77, 78].

Given a static external magnetic field B_0 , the NMR frequency is $\nu_0 = \gamma B_0$ where γ is the gyromagnetic ratio of the target nucleus ($\gamma \approx 42.6$ MHz/T for protons) [79]. In order to obtain a high signal-to-noise ratio (SNR) and access the information hidden in NMR spectra, strong and homogeneous magnetic fields are required [3, 80]. The realization of strong and homogeneous miniaturized magnets is the main obstacle towards low-cost portable NMR tools, possibly solved by Halbach configurations of permanent magnets [81, 82]. NMR systems also require relatively complex RF electronics for resonance excitation and signal detection. The design of electronic micro-chips for NMR purposes has the aim to shrink the size of electronics for low-cost NMR spectrometers [12, 13, 16, 18] and to combine micro-coils with integrated receivers in order to achieve probes parallelization and high spin sensitivity [26–28, 36].

The first integrated probe was proposed for magnetometry purposes and employed integrated pick-up coils coupled to receivers, with the excitation operated by a second inductively decoupled coil [29]. Receiver-only chips, with the whole electronics buried below integrated microcoils, were proposed as optimal choice for micro-imaging [28], parallel imaging arrays [26], and probes for surgical guidance [27]. The realization of integrated transceivers for NMR purposes, of which there are only a few examples [12, 13, 18], also included integrated pulse sequencers aiming at miniaturizing the size and abating the costs of the overall electronics needed to build spectrometers.

This report describes a broadband single-chip transceiver, whose combination with multi-frequency probes provides a simple, but effective and versatile, low-cost electronic interface for NMR probes. We show its employment in combination with both external and integrated microcoils. As specific examples, we performed multi-nuclear NMR spectroscopy on solids and liquids. The single-chip transceiver consists of an RF power amplifier, an RF low-noise preamplifier, a frequency mixer, an audio-frequency (AF) amplifier, and fully integrated transmit-receive switches. One issue of integrated transceivers is to connect efficiently transmission (TX) and reception (RX) electronics with the excitation-detection coil. In previous works switches were placed in series with the transmitter, implying power losses in TX mode [12, 18]. The topology used to realize the switches allows, as well as that in ref [13], power transmission without power loss. More than 50 dB isolation is provided between TX and RX and both channels operate with best performance from 1 MHz to 1 GHz.

We realized probes for samples of volumes of the order of 100 nL (using an external coil) and 250 pL (using an integrated microcoil). Recently, non-resonant microcoils were indicated as an option to realize volume-limited (25 nL) multi-nuclear NMR probes [83]. Nevertheless, at the same scale, it is still possible to use resonant micro-solenoids capable of high spectral resolution and spin sensitivity [84]. Indeed, when possible, the use of LC resonators allows a lossless intrinsic gain between the coil and the receiver, definitively advantageous in terms of

SNR [3]. An issue in multi-frequency resonant probes is to tune the same resonator at different frequencies. The single-chip transceiver is interfaced with a resonant coil via a matching network where reversed biased diodes are employed as voltage controlled capacitors, allowing for a frequency range where the ratio between the maximum and minimum frequency is up to a factor four. The fully integrated probe, on the other hand, is designed for volumes where it is hardly possible to realize multi-frequency LC resonators. Thus, a non-resonant microcoil is used. As future prospective, this work can serve as base to realize low-cost NMR interfaces and high sensitivity micro-probe arrays for micro-imaging and mass-limited spectroscopy purposes.

Sect. 1.3 is dedicated to the description of the integrated electronics and probes design. In Sect. 1.4 we recall the basics of pulsed NMR in relation to the experimental setup. In Sect. 1.5 we present multi-nuclear spectroscopy experimental results obtained with the realized probes.

2.3 Electronics design

Fig. 2.1a shows photographs of the single-chip transceivers. The chips, realized with a 2P6M CMOS 130 nm process provided by STMicroelectronics, have dimensions of about 1 mm^2 . Fig. 2.1b shows the block diagram of the single-chip transceiver where transmitter and receiver are connected to the integrated or external coil at two nodes a and \bar{a} . In what follows we give an outline of pitfalls and trade-offs in designing this instrumentation, but we defer to the final chapter for the detailed schematics at the transistor level.

2.3.1 Transmitter

The transmitter design, inspired by previous reports, consists of two differential chains of inverters [12]. Our integrated switches allow commutation between TX and RX in some ns and provide more than 50 dB isolation between the two channels. No switches are used in series with the output stage of the transmitter, which consequently operates with no power losses. Fig. 2.1b shows the case in which the TX mode is selected. In the RX mode, the two inverter chains are in stand-by, no current is drawn from their DC source, and the four last transistors of the transmitter act as open switches with impedances of about 200 k Ω . We used 2.5 V I/O transistors, which operate at the largest voltage of the technology employed. During transmission, the inverters impose differential squared waves in a and \bar{a} , both toggling between ground and 2.5 V. The output impedance of the transmitter is $Z_s = 50 \Omega$. The power delivered to the probe depends on the impedance Z between nodes a and \bar{a} in TX mode, and it is $P = V_{rms}/|Z_s + Z|$, where $V_{rms} = 1.8 \text{ V}$ for sinusoids of amplitude 2.5 V. When we use an external coil, we tune it at the working frequency and match its impedance to $R_m = 320 \Omega$. In these conditions, the transmitted current is about 10 mA and the transmitted power is about 10 mW. When we use the integrated coil, the transmitted current is about 20 mA and the transmitted power is about 20 mW at 300 MHz (see description of the integrated coil below).

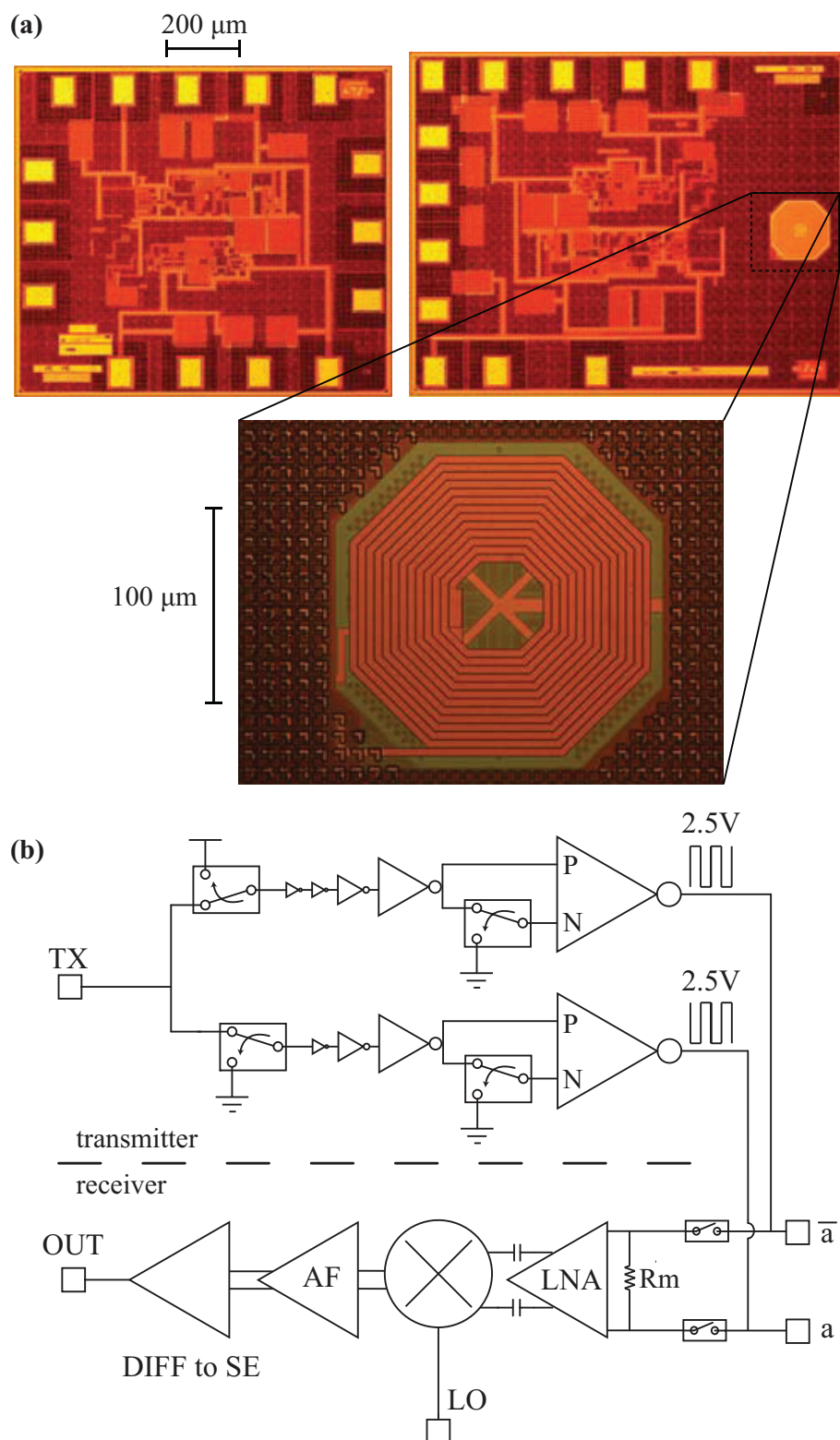


Figure 2.1: **Photograph and block diagram of single-chip transceiver.** (a) Photograph of the single-chip transceivers for both external (left) and integrated (right) coil. (b) Block diagram of the single-chip transceiver.

The transmitter current limit is 70 mA.

2.3.2 Receiver

The receiver consists of a low-noise RF amplifier (LNA), a double balanced Gilbert mixer, a Miller AF amplifier, and a last amplification stage where the signal is converted from differential to single-ended. Integrated mixed signal circuits suffer of common mode noise due to digital switching noise on the supply line. For this reason, the whole receiver is designed as a fully differential system. The differential-to-single-ended conversion is done once the common mode noise is much smaller than the amplified differential one. The detailed schematics of LNA, mixer and AF amplifier can be found in Chapter 5.

The LNA has a gain of 35 dB and it is AC coupled to the mixer in order to avoid offset problems. Mixer and AF part have gain of 19 dB. Hence the overall gain of the receiver is 54 dB. The receiver consumes a current of 14 mA from a 1.5 V DC source. The wideband fully differential LNA is the first element interfaced with the coil. Its bandwidth is 1–300 MHz and its frequency-dependent input impedance is $Z_{LNA} = 1/i\omega C_{gs}$, with C_{gs} (the gate capacitance of the input transistors) 0.5 pF. The large size of the input transistors, whose areas measure 150 (P-MOS) and 63 (N-MOS) μm^2 , is necessary to reduce the $1/f$ noise component at low frequencies. When the coil is external, a resistor $R_m = 320 \Omega$ fixes the real part of the input impedance and protects the LNA from the energy discharge associated with TX to RX switching. When the coil is integrated there is no resonator and no impedance matching, and R_m is increased to 20 k Ω to improve noise performance (see below). The impedance of the two switches connected to a and \bar{a} is about 10 Ω in RX mode and 6 k Ω in TX mode. Hence, the contribution of the switches to the electronic noise in RX mode is negligible.

2.3.3 Deadtime

During transmission the resonating RLC network stores a certain amount of energy, whose ratio with the energy dissipated per unit cycle defines the quality factor $Q = \omega L/R_C$, where ω is the resonating angular frequency, L the inductance of the coil, R_C its resistance [85]. Switching from TX to RX, the stored energy dissipates and causes the saturation of the receiver for a time which depends on both the time needed by the resonator to discharge and the time needed by the receiver to recover from its saturation condition. The combination of these two delays gives rise to the so called dead-time, defined as the time interval between the end of the excitation and the beginning of useful signal acquisition. In an optimal design the recovery of the receiver should be negligible and the dead-time should be mainly determined by the discharge time of the resonator and the gain of the electronics. The decay time of the discharging resonator is $T_d = L/R = Q/\omega_0$. The recovery time of the receiver is of the order of the inverse of its AF bandwidth, which in our case is about 4 MHz. The measured recovery time of our receiver is about 1 μs . After excitation, the NMR signal decays exponentially with the relaxation time T_2 . T_2 Relaxation times in liquids can be as large as 10 s, while solids and elastomers have relaxation times between tens of μs and some ms. It is thus clear that having

a short dead-time is necessary to allow pulsed experiments on a broad variety of samples.

2.3.4 Variable frequency probes

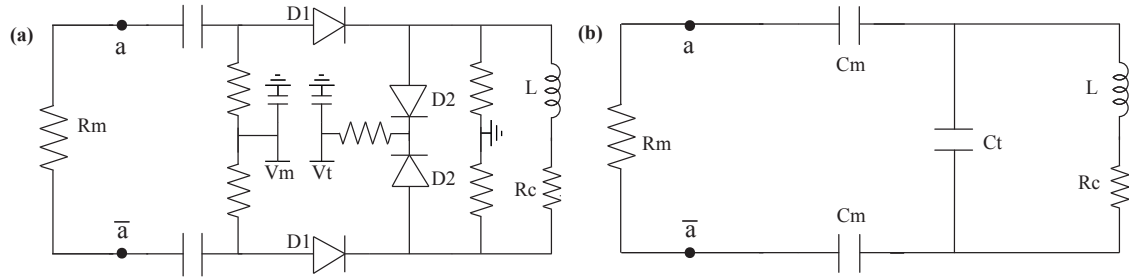


Figure 2.2: **Multi-frequency probes schematics.** (a) multi-frequency probe: the tuning and matching capacitances are given by reverse-biased varicap diodes, and are regulated by the control voltages V_m and V_t . V_m is negative and V_t positive, their absolute value ranging between 0 and 25 V. $D1$ (matching): NXP BB181, $D2$ (tuning): NXP BB182. (b) Equivalent circuit.

Fig. 2.2a shows a schematic of a multi-frequency probe, where matching and tuning capacitors C_m and C_t are adjusted by two voltage sources V_m and V_t on reverse-biased varicap diodes $D1$ and $D2$. The external probe is fully differential to reject the common mode noise. Fig. 2.2b shows the equivalent circuit where, essentially, a coil is interfaced with a real impedance R_m . Varying C_m and C_t , the impedance across nodes a and ā can be transformed until it matches R_m [85]. In this probe, C_m and C_t have a dynamic range (defined as C_{max}/C_{min}) of about 16. The main drawback in using diodes as capacitors is that, during transmission, large signals are applied across the coil inducing for limited time forward bias of the diodes, hence dissipating some transmitted power. This particular issue can have severe consequences on the performance of the probe and it is more relevant when using coils with high Q factors: a larger Q factor implies larger voltage signals across the coil and thus more undesired power dissipation (see discussion in Section 1.5).

The choice of the matched impedance is important when a fixed and relatively small power is available in transmission. Indeed, it is possible to show that (see below) the process of impedance transformation includes an intrinsic voltage gain $G_{int} \approx \sqrt{R_m/4R_c}$ from the coil to the nodes a and ā, indicating as optimal choice a high matched impedance to reduce the contribution of the noise of the electronics. It is also true (see below) that the pulse length necessary to reach the maximum signal condition is $\tau_{\pi/2} \approx \pi \sqrt{R_m R_c} / \sqrt{2} \gamma B_u V_{rms}$ indicating a small matched impedance as preferable choice. Thus, a higher matched impedance is convenient when receiving but inconvenient when transmitting with a fixed limited power. In our design, the choice $R_m = 320 \Omega$ was judged to be a good compromise between pulse lengths and noise performance.

2.3.5 External coil: intrinsic gain and pulse time

In this short paragraph we derive the expressions of the intrinsic gain G_{int} and pulse length $\tau_{\pi/2}$ in tuned and matched pulsed NMR probes as the ones described above. Fig. 2.3a shows equivalent circuits of probes in both TX and RX conditions. In Fig. 2.3a a voltage V across the nodes a and \bar{a} is imposed and we are interested in the current through the coil i (TX mode).

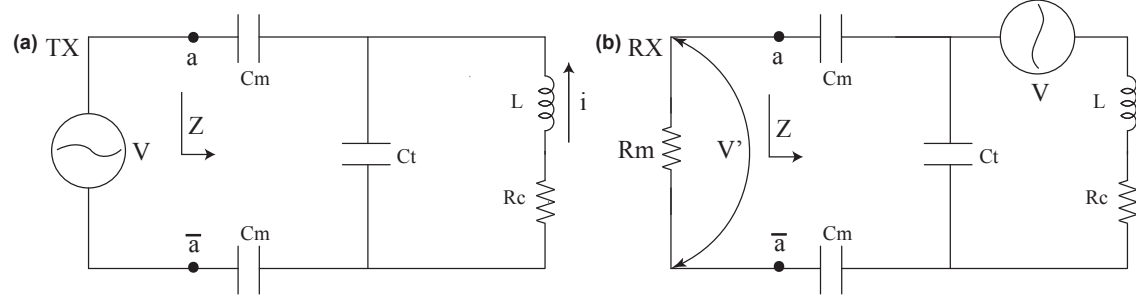


Figure 2.3: **Probes tuning and matching.** (a) Schematics representing tuned and matched probe in (a) TX mode and (b) RX mode.

In Fig. 2.3b the NMR signal is represented by an electromotive force induced in the coil and we want to calculate the voltage $V' = G_{int} V$ across the nodes a and \bar{a} (RX mode). The tuning and matching capacitances, respectively C_m and C_t , are used to transform the impedance of the coil. Being reactive elements, no noise is added by them and we can assume that during impedance transformation the SNR is preserved. If we impose that the impedance Z of the circuit on the right side of the nodes a and \bar{a} is equal to R_m (i.e., impedance matching condition) we obtain:

$$C_t = \frac{2\omega Q}{R_C} - \sqrt{\frac{4\omega^2 Q^2}{R_C^2} - 4\omega^2(1+Q^2)\left(\frac{1}{R_C^2} - \frac{1}{R_m R_C}\right)} \quad (2.1)$$

$$C_m = \frac{2}{\omega R_m Q - \omega^2 C_t Q^2 R_C R_m - \omega^2 C_t R_C R_m}$$

For simplicity, we neglected the parasitic capacitance of the LNA, whose impedance has to be compared to $R_m/2$. In our system $R_m/2 = 160 \Omega$ and the impedance of the LNA parasitic capacitance is about $1.1 \text{ k}\Omega$ at 300 MHz . Solving the circuit in Fig. 2.3a and using 2.1 we obtain the relation between V and i :

$$i_{rms} \simeq \frac{V_{rms}}{\sqrt{R_m R_C}} \quad (2.2)$$

During excitation, the effective field is $B_1 = B_u \sin(\omega_0 t)/2$. Given that $\theta = \gamma B_1 t$ the pulse duration $\tau_{\pi/2}$ required to reach the maximum signal can be written as:

$$\tau_{\pi/2} \simeq \frac{\pi \sqrt{R_m R_C}}{\sqrt{2} \gamma B_u V_{rms}} \quad (2.3)$$

Equation 2.3 shows that choosing a large value for R_m would be unattractive, while a high B_u helps in reducing the pulse length. Similarly, solving the circuit in Fig. 2.3b gives:

$$V' \simeq V \sqrt{R_m / 4R_C} \quad (2.4)$$

From equation 2.4 we obtain $G_{int} = V'/V \simeq \sqrt{R_m / 4R_C}$. As we can see, a larger R_m would be convenient in reception since a large intrinsic gain guarantees that the noise coming from the coil becomes dominant with respect to the noise of the front-end electronics n_{elec} . This observation is evident also writing the total input noise of the system, which is $n_{in} = \sqrt{2k_B T R_m + n_{elec}^2}$.

2.3.6 Integrated coil

The integrated coil shown in Fig. 2.1a is realized using the top four metals of the integrated circuit technology. The number of turns (22 in total), their diameter and their width is optimized for cubic samples with edges of 50 μm . The $\text{Si}_3\text{N}_4/\text{SiO}_2$ passivation, separating sample and coil, is 1.1 μm thick. The 13 turns in the highest metal are in aluminium, 0.9 μm thick, 3.6 μm wide. The remaining three copper metals have three turns each, 0.35 μm thick and 6.4 μm wide. The DC inductance is 54 nH and the DC resistance is 60 Ω . Since the skin depth in both copper and aluminium at 300 MHz is significantly larger than the metal thickness, the resistance at 300 MHz is marginally higher than the DC value. The inhomogeneous sensitive volume of this microcoil roughly corresponds to a deformed semi-ellipsoid having a volume of about 250 pL. We will better study this aspect later, when the results retrieved will require a more detailed analysis of the microcoil sensitivity. For the remaining of this chapter, we can consider (in very good approximation) that the sensitive volume is of about 250 pL and that the average unitary field is of about 0.2 T/A.

2.4 Experimental Setup

When placed into an external static magnetic field B_0 along a direction \hat{z} , spins of paramagnetic nuclei precess about the static field at the Larmor angular frequency $\omega_0 = \gamma B_0$ and their energy minimum favors their partial alignment along \hat{z} , giving a macroscopic magnetization $M_0 =$

2.4. Experimental Setup

$N_s(I+1)I\gamma^2\hbar^2B_0/(3k_B T)$, N_s being the density of spins, I the nuclear spin, T the temperature of the sample [72]. It is possible to exploit a resonant phenomenon by applying a field B_1 oscillating at the Larmor frequency along a direction perpendicular to \hat{z} . In doing so, the orientation in space of the sample magnetization M changes, rotating in space with an angular velocity $\omega_1 = \gamma B_1$. After an excitation time τ , the angle θ between M and \hat{z} will be $\theta = \gamma B_1 \tau$ [72]. When B_1 is suddenly shut down, the magnetization relaxes towards its thermal equilibrium condition keeping its precession at frequency ω_0 about \hat{z} . An electromotive force, which survives as long as the spins precession remains coherent, is induced by Faraday's law in any inductor placed in proximity.

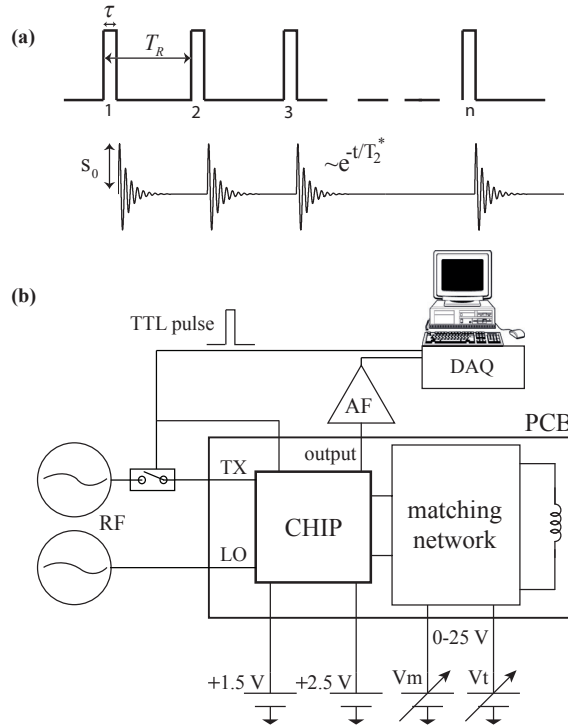


Figure 2.4: **Experimental Setup.** (a) A schematics of a pulsed NMR experiment, where n pulsed experiments are performed with pulse length τ and repetition time T_R . The signal has an amplitude s_0 and an effective relaxation time T_2^* . (b) Block diagram of the complete NMR system. RF source: Anritzu MG3633A. AF amplifier: Stanford SR560. The printed circuit board (PCB) containing the single-chip transceiver is inserted into the 54 mm room temperature bore of a Bruker 7.05 T superconducting magnet.

A basic NMR experiment uses a single coil to excite the resonance and pick-up the free induction decay signal (FID), whose initial amplitude is given by $s_0 = \omega_0 M_0 V_s B_u \sin\theta$ [3], where B_u is the field per unit current (unitary field) of the coil and V_s the sample volume. The maximum signal is obtained when the magnetization of the sample is rotated by $\theta = \pi/2$ and the excitation field B_1 must be as high as possible in order to reach this condition in a short time compared to the nuclear relaxation time [72]. Having small excitation pulse lengths (a few

μs) also guarantees uniform excitations of broad spectra. Fig. 2.4a illustrates a simple pulsed NMR experiment, where n excitation pulses of length τ and n acquisitions are consecutively performed with a repetition time T_R . After each pulse, a signal with initial amplitude s_0 and typical decay time T_2^* is acquired. For a maximal signal in each measurement, the repetition rate T_R must be significantly larger than T_1 , which is the time required to restore the thermal magnetization M_0 . Usually called longitudinal (or spin-lattice) relaxation time, T_1 depends on both the sample and the external field. From the received signal one can extract the amplitude s_0 proportional to the number of participating spins, the Larmor frequency dependent on the chemical structure [86], and the effective relaxation time T_2^* . In liquids, the effective relaxation time is mainly due to the field inhomogeneity within the sample, which facilitates the loss of coherence between spins and thus the decay of the signal. With more complicated pulse sequences (e.g., the spin echo technique) [30], one can have access to the true relaxation time T_2 , which reveals information concerning spin-spin interaction within the sample, ultimate cause of spin decoherence [87].

Fig. 2.4b shows the block diagram of the setup used for our measurements. The single-chip transceiver is wire bonded to a printed circuit board (PCB). The transceiver is inter-faced with the external excitation-detection coil via a matching network (see Fig. 2.2), while no other component is needed when the coil is integrated on-chip. For excitation and down-conversion one can choose to use a single RF generator or two separate ones. The advantage of working with two RF generators is the on-resonance transmission, allowing both the use of long pulse lengths and a down-converted frequency far from the $1/f$ noise region. When using two separate RF sources, a pre-switch of the excitation signal is preferable to eliminate the weak parasitic signal due to TX to RX leakage. The output signal is amplified before acquisition. The gain and anti-aliasing low-pass filter of the AF amplifier increase the effective dead-time of the system (up to $9\ \mu\text{s}$ with a gain of 103 and low-pass filter at 300 kHz). Four DC sources are dedicated to transmitter (2.5 V), receiver (1.5 V), tuning and matching in variable frequency probes ($\pm 25\ \text{V}$). A multifunction board (NI BNC-2110) is used for generation of TX/RX TTL switching pulse and signal acquisition. All experimental parameters T_R , τ , (V_m , V_t , for external coil) are controlled by a LabVIEW program.

2.5 Results

2.5.1 Noise and Gain

The gain of the receiver, measured by looking at the amplification of a controlled input voltage signal, is 54 dB in agreement with simulations within 2 dB in the frequency range 1 – 300 MHz. The simulated input referred noise of the receiver is $1.1\ \text{nV}/\text{Hz}^{1/2}$ within its bandwidth. When an external coil is matched to $320\ \Omega$ the equivalent impedance at LNA input is $160\ \Omega$, resulting from the parallel between $320\ \Omega$ and R_m . In these conditions, the overall receiver input noise is expected to be $2\ \text{nV}/\text{Hz}^{1/2}$. When we consider the $60\ \Omega$ integrated coil the input noise is given by n_{elec} and the coil itself. The expected input noise in this condition is $1.5\ \text{nV}/\text{Hz}^{1/2}$. Fig. 2.5 is a measurement of the input noise voltage spectral density (VSD) for both cases,

showing good agreement with the expected values.

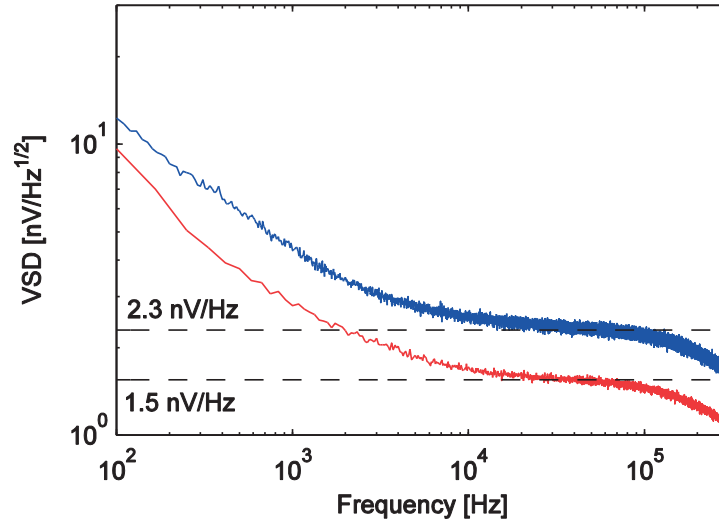


Figure 2.5: **Measured equivalent input noise voltage spectral density (VSD)**. Blue: noise with a 320 Ω resistor at receiver input. Red: noise with the integrated micro-coil at receiver input. The local oscillator (LO) frequency is 100 MHz at 0 dBm power. The acquisition is performed with sampling rate of 1.3 MHz and a 300 kHz antialiasing filter. The corner frequency is slightly dependent on the local oscillator frequency, with a value of 15 kHz at 300 MHz. The noise level measured at 50 kHz is independent from the local oscillator frequency in the range from 1 MHz to 1 GHz.

The effective noise figure can be defined as the factor by which the SNR originally given by the coil is degraded. When an external coil is matched to the real input impedance of the receiver the SNR is degraded by 3 dB, a factor paid to appropriately protect the LNA using 320 Ω at the input. A further degradation of 2 dB is added by the electronic noise of the receiver. This relatively large factor is due to the trade-off between the wide bandwidth operation (1 – 300 MHz) and the low input referred noise. The total effective noise figure with external coil is thus 5 dB. In the fully-integrated probe, the electronic noise is approximately equal to the thermal noise of the microcoil thanks to the increased R_m , giving an effective noise figure of 3 dB.

2.5.2 Multinuclear NMR spectroscopy

In this section we show the application of our single-chip transceiver to multi-nuclear NMR mass-limited spectroscopy. The multi-nuclear probe with external coil is a multi-frequency probe as shown in Fig. 2.2a, where the coil is a 14 turns solenoid made by an enameled copper wire ($\phi = 100 \mu\text{m}$) wrapped around a fused silica capillary having an external diameter of 450 μm and internal one of 320 μm . Its inductance is $L = 60 \text{ nH}$ and its unitary field is $B_u = 0.012 \text{ T/A}$ at 300 MHz. The resonator resistance is dominated by the resistance of the diodes and their connection to the coil, and it is estimated at about 2 Ω at 300 MHz. During the fabrication

no glue is used to fix the wire on the capillary. The coil is inserted into a 2 mL Eppendorf tube (BRAND® microcentrifuge tube, $\phi = 1$ cm) later filled with D_2O for susceptibility matching [84]. In our case, the best achieved full width at half maximum of the 1H spectrum goes from about 50 Hz to 6 Hz when the susceptibility matching fluid is added.

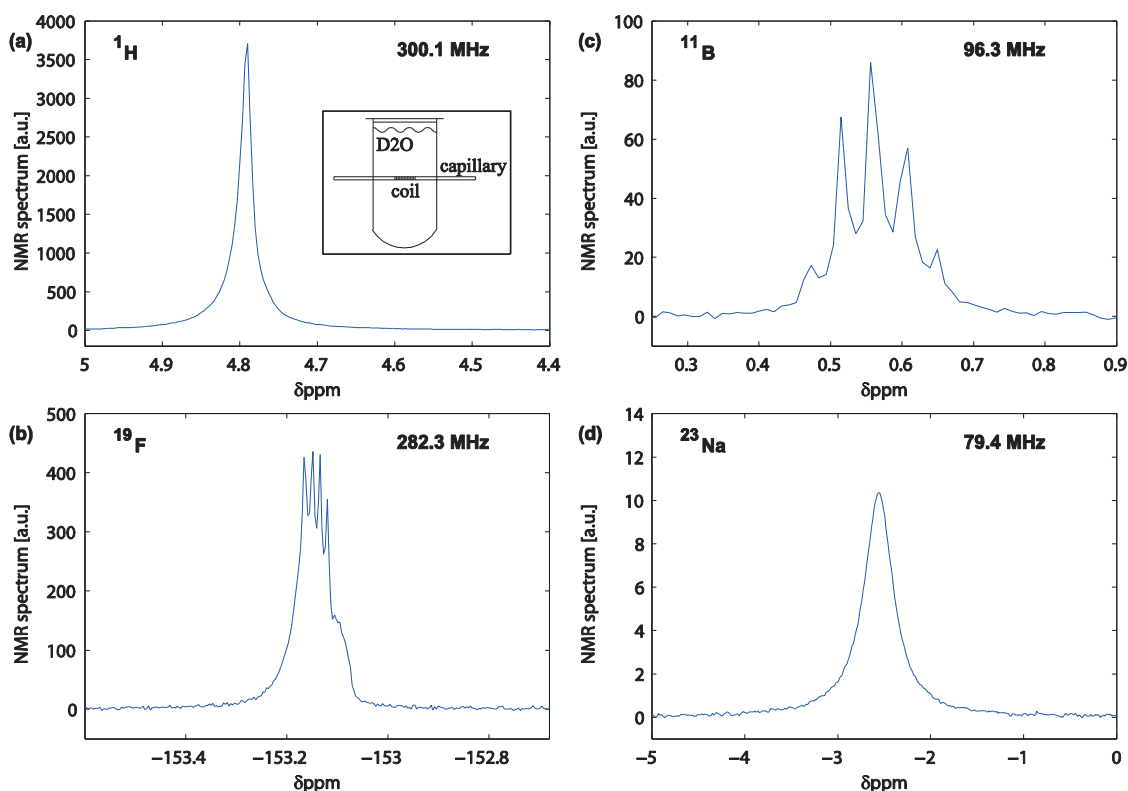


Figure 2.6: **Measurements with the external coil probe in a field $B_0 = 7.05$ T.** Spectra are real parts of the FFT. For all measurements we used a single coil matched and tuned at various frequencies using varicap diodes. The coil consists of 14 turns 100 μm diameter enameled copper wire solenoid wrapped around a fused silica capillary (from BGB) having external diameter of 450 μm and internal diameter of 320 μm . The sample volume is 100 nL and contains NaBF_4 dissolved in H_2O with a concentration of 7.5 M. The coil is inserted in a 2 mL Eppendorf tube filled with D_2O for susceptibility matching. The acquisition is performed for 800 ms with sampling rate of 500 kHz. The gain before signal acquisition is 10^2 and the antialiasing filter frequency is 100 kHz. Each signal is down-converted at about 50 kHz. 7 μs of data are rejected. (a) 1H spectrum, single measurement with $\tau = 12$ μs . (b) ^{19}F spectrum, single measurement with $\tau = 14$ μs . (c) ^{11}B spectrum, average of 20 measurements with $T_R = 15$ s and $\tau = 32$ μs . (d) ^{23}Na spectrum, average of 500 measurements with $T_R = 1$ s and $\tau = 52$ μs . In this case, an exponential matched filter with decay time 250 ms is applied.

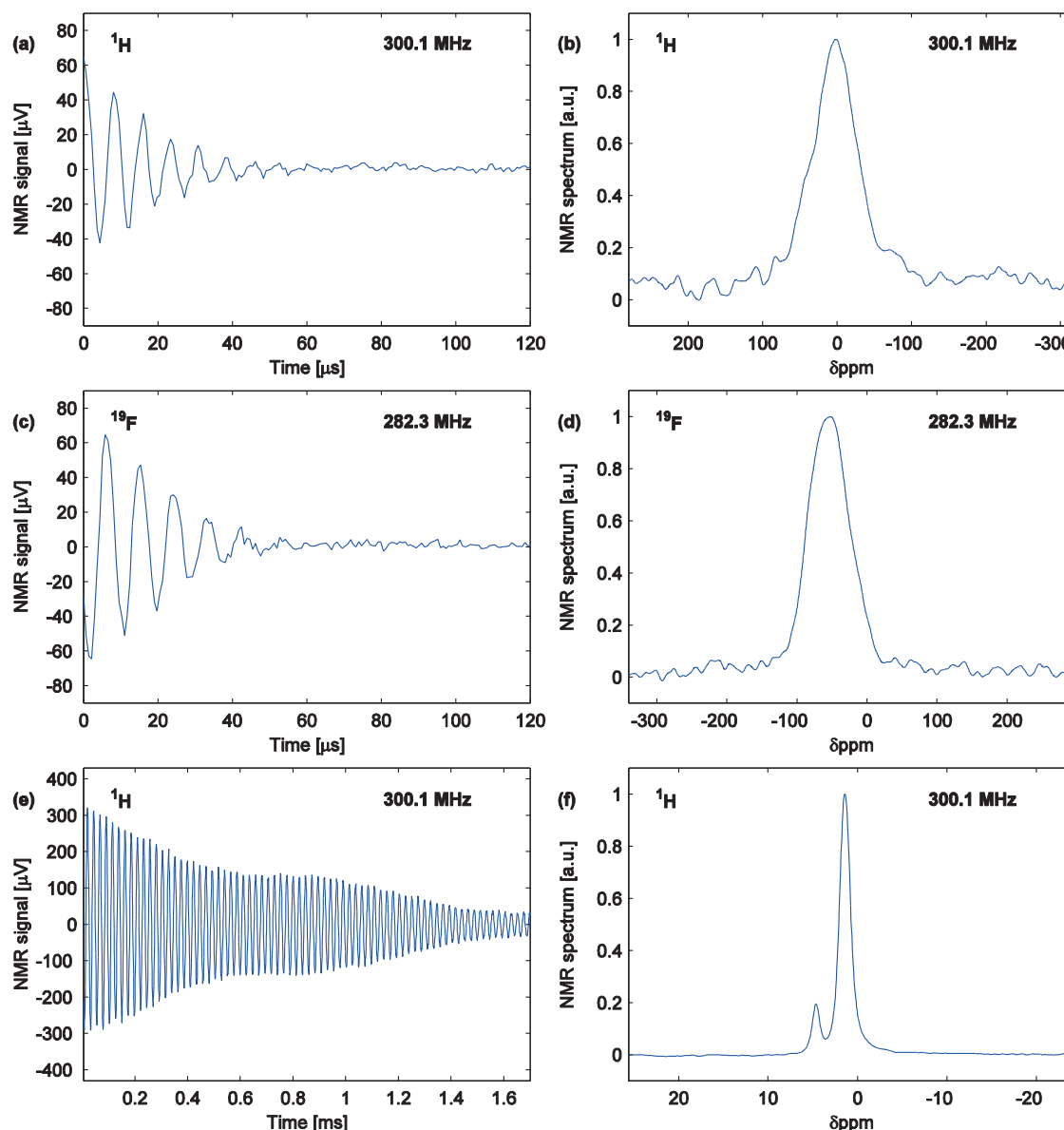


Figure 2.7: **Measurements with the integrated coil in a field $B_0 = 7.05$ T.** (a) Time domain signal of ^1H at chip output, average of 5000 measurements with $T_R = 14$ s and $\tau = 2$ μs . (b) ^1H spectrum. (c) Time domain signal of ^{19}F at chip output, average of 5000 measurements with $T_R = 8$ s and $\tau = 2$ μs . (d) ^{19}F spectrum. Spectra are real parts of the FFT obtained from a solid sample of NH_4PF_6 placed on the micro-coil shown in Fig. 2.1a. The sample is a grain of about 130 pL. An exponential matched filter with decay time 100 μs is applied. (e) Time domain signal of ^1H at chip output, average of 3000 measurements with $T_R = 1$ s and $\tau = 2$ μs . (f) ^1H spectrum. The sample is about 250 pL of solid cis-polyisoprene. An exponential matched filter with decay time 2 ms is applied. (a-d) The acquisition time is 5 ms. (e-f) The acquisition time is 20 ms. (a-f) The gain before signal acquisition is 10^3 and the antialiasing filter frequency is 300 kHz. The acquisition is performed with sampling rate of 1 MHz. 9 μs of data are rejected. Each signal is down-converted within 50 and 150 kHz.

Fig. 2.6 shows the real part of the spectra taken from a sample of 7.5 M of NaBF_4 dissolved in H_2O . NMR experiments on this system have been reported previously [88]. J-splitting of ^{19}F and ^{11}B have 1:1:1:1 primary peaks for fluorine and 1:4:6:4:1 for boron with relative shifts of about 5 Hz at 7 M concentration. These peaks arise from the J-coupling between ^{19}F ($I = 1/2$) and ^{11}B ($I = 3/2$) spins in the BF_4 molecule. Fig. 2.6a shows the ^1H spectrum due to H_2O . Fig. 2.6b shows the ^{19}F spectrum, where the four peaks due to ^{11}B are visible, while a second unresolved structure arises from the presence of ^{10}B isotope ($I = 3$). Fig. 2.6c shows the ^{11}B spectrum, with the five peaks due to the possible configurations of four equivalent ^{19}F spins. Finally, the single peak in Fig. 2.6d arises from Na^+ ions. All chemical shifts are expressed in ppm deviation from the resonance frequency of standard reference samples, using for each nucleus the values reported in Ref. [89]. Since these reference molecules were not present in our sample, we assigned a chemical shift of 4.79 ppm to the ^1H peak of H_2O , thus computing the resonance frequency of the ^1H reference sample. This allows to determine the chemical shifts for all nuclei with respect to their usual references as suggested in Ref. [89].

Fig. 2.7 shows measurements performed with the integrated microcoil of Fig. 2.1a. No stabilization system acts on the magnetic field, whose typical drift during twenty hours is below 60 nT (9 ppb) (see following chapter). In Fig. 2.7a-d the sample is a grain of ammonium hexafluorophosphate (216593, Sigma Aldrich). Both ^{19}F and ^1H signals show a relaxation time of about 30 μs . These measurements on a solid sample were possible thanks to the short dead-time of our probe. Fig. 2.7e-f show measurements on a sample of cis-polyisoprene (182141, Sigma Aldrich). Due to a relatively important chain segmental mobility, cis-polyisoprene has a ^1H -NMR resonance line significantly narrower with respect most of solid samples. Fig. 2.7f shows the real part of the FFT, to which the three groups CH, CH_2 and CH_3 contribute. The main peak is given by groups CH_2 and CH_3 , the secondary one by CH [90]. All chemical shifts are expressed in ppm deviation from the resonance frequency of standard reference samples, using for each nucleus the values reported in Ref [89]. Since these reference molecules were not present in our sample, we assigned a chemical shift of 1.5 ppm to the ^1H peak of CH_2 and CH_3 and assumed the same field B_0 for both samples.

In a pulse of length τ there are frequencies up to an offset from carrier of about $1/\tau$ and, in multi-nuclear experiments on unknown samples, the employed pulse lengths should be short enough to excite resonance at all the possible chemical shifts. Thus, the ability of transmitting power to the coil can be critical for the excitation of broad spectra. In Table 2.1 we report the measured $\tau_{\pi/2}$. For the external coil, the measured pulse lengths are in agreement with SPICE simulations of the transmission condition using, for varactor diodes, the models provided by manufacturers. By comparison with simulations performed with fixed capacitors we concluded that the use of varactor diodes increases the $\tau_{\pi/2}$ length by a factor 1.3.

In Table 2.1 we report the theoretical and experimental values of the signal amplitudes s_0 and noise VSD . Based on s_0 and VSD , it is possible to express the sensitivity of the probe in terms of nuclear spins. The spin sensitivity N_{min} , defined as $N_{min} = V_s N_s VSD / s_0$, is equal to the number of nuclear spins which give a time-domain SNR of 1 considering a noise equivalent bandwidth of 1 Hz. This quantity expresses unambiguously the capability of the probe to sense nuclear spins, independently from the effective relaxation time T_2^* and the number

of spectral lines. From the value N_{min} it is possible to compute the expected SNR in the frequency domain, once the distribution of the spectral lines of the sample and the effective relaxation time are known. We note that the sensitivity of the fully integrated probe surpasses by an order of magnitude the one of the external coil, proving the advantage of having a larger B_u . For the fully integrated probe, the unitary field in proximity to the center of the coil is $B_u = 250$ mT/A. For the external solenoid $B_u = 12$ mT/A. As shown in Table 2.1, our integrated probe achieves a ^1H spin sensitivity N_{min} of about 1.5×10^{13} spins/Hz $^{1/2}$ at 300 MHz. Since the gain and input VSD scale by approximately the same factor up to 1 GHz, we expect a ^1H spin sensitivity of 2×10^{12} spins/Hz $^{1/2}$ at 1 GHz.

External Coil (7.5 M NaBF ₄ in H ₂ O)					
	ν_0 [MHz]	$[\tau_{\pi/2}]$ [μs]	s_0 [mV]	VSD [$\mu\text{V}/\text{Hz}^{1/2}$]	N_{min} [Hz $^{-1/2}$]
^1H	300.1	12 (9)	35 (50)	0.6 (0.5)	10^{14} (8×10^{13})
^{19}F	282.3	14 (10)	15 (17.5)	0.6 (0.5)	10^{14} (8×10^{13})
^{11}B	96.3	32 (29)	6 (10)	0.9 (0.7)	8×10^{14} (4×10^{14})
^{23}Na	79.4	52 (35)	5 (8)	0.9 (0.7)	10^{15} (6×10^{14})
Integrated Coil (NH ₄ PF ₆)					
^1H	300.1	2 (2)	0.11 (0.1)	0.32 (0.35)	1.5×10^{13} (1.5×10^{13})
^{19}F	282.3	2 (2)	0.13 (0.14)	0.32 (0.35)	1.5×10^{13} (1.5×10^{13})
Integrated Coil (cis-polyisoprene)					
^1H	300.1	2 (2)	0.34 (0.36)	0.32 (0.35)	1.5×10^{13} (1.5×10^{13})

Table 2.1: Performance and characteristics of the multinuclear probes. ν_0 : resonance frequency, $\tau_{\pi/2}$: $\pi/2$ nutation pulse length, N_{min} : spin sensitivity, s_0 : signal amplitude at chip output, VSD : noise voltage spectral density at chip output. Theoretical values are in parenthesis (equations in sections above).

2.5.3 Discussion

In this work we proposed a 1 mm² broadband single-chip transceiver for multi-frequency pulsed NMR probes. On a scale of sample volumes of 100 nL we used reversed biased diodes as tuning and matching elements to realize multi-frequency LC resonators. On a scale of sample volumes smaller than 250 pL we used a non-resonant integrated microcoil. As a result, we obtained simple, but effective and versatile, low-cost electronic interfaces for NMR probes

Chapter 2. A broadband single-chip transceiver for multi-nuclear NMR probes

with high spin sensitivities.

The fully integrated TX/RX switch allows minimization of off-chip discrete components, while the broadband nature of the transceiver allows its use in multi-nuclear probes as the ones described above. We demonstrated the versatility of this approach by showing its use for multi-nuclear NMR spectroscopy on both liquid and solid samples.

Given that the use of short pulse lengths is a key feature needed by pulsed NMR probes, we discussed the problem of having a fixed limited power during transmission. We concluded that experiments in mass-limited conditions can be applied at their best in both resonant and non-resonant probes thanks to the high field per unit current produced by microcoils.

Apart from size reduction, the use of integrated CMOS transceivers for NMR pulsed probes might have many practical advantages to manufacturers, such as to avoid the search of non-magnetic electronic components and possibly reduce costs. As future prospective, our work can serve as base to realize simple low-cost NMR interfaces and high sensitivity micro-probes arrays for micro-imaging and mass limited spectroscopy purposes.

3 CMOS-based broadband NMR probes for high field magnetometry

3.1 Abstract

In this chapter we introduce a new complementary metal-oxide-semiconductor (CMOS) broadband transceiver for the implementation of nuclear magnetic resonance (NMR) probes aimed for high field magnetometry. The single-chip transceiver, interfaced with external resonators, is capable of broadband ($10\text{-}10^3$ MHz) TX/RX operation and quadrature (IQ) demodulation. In this work we demonstrate its use in combination with NMR-based commercial instruments and custom multi-channel NMR probes. The commercial application is implemented in close collaboration with Metrolab SA, which is the industrial partner of the PhD project. Besides showing a full compatibility of our transceiver with Metrolab's instrumentation at no costs in terms of performance, we show that custom probes employing water samples of 500 nL are capable of resolutions as high as 0.06 ppb/Hz^{1/2} (about 0.4 nT/Hz^{1/2}) at 7 T, and that magnetic noise due to field fluctuations can be directly measured at this resolution level. As a result, this study gives an indication of the fact that measurements at high fields may be performed at maximum precision already with relatively small samples.

3.2 Introduction

Nuclear magnetic resonance (NMR) is the method of choice for high accuracy and resolution measurements of high magnetic fields (above 0.1 T) [29, 91–97]. High field NMR magnetometers are commonly used, e.g., to quantify the inhomogeneity of magnetic resonance imaging (MRI) magnets [98], to determine the time-evolution of MRI pulsed gradients [91, 92], to measure and control high energy physics magnets [93, 94], and to calibrate other sensors (e.g. Hall sensors) [99]. NMR based methods can be used also for magnetometry down to the earth magnetic field (about 0.01 mT). At low fields hyperpolarization (optical or microwave) techniques [100, 101], flowing water pre-polarization [102], or non-inductive techniques [103–105] are necessary to achieve a sufficiently large signal-to-noise ratio (SNR).

This chapter is a preliminary version of a work that we might be able to submit in the future.

Chapter 3. CMOS-based broadband NMR probes for high field magnetometry

The NMR frequency of a nucleus in a magnetic field B_0 is $\nu_0 = (\gamma/2\pi)B_0$, where γ is the gyromagnetic ratio of the target nucleus ($(\gamma/2\pi) = 42.577\,478\,92(29)$ MHz/T for protons) [79] and ν_0 is called Larmor frequency. In NMR magnetometers, the value of the field is obtained from a frequency measurement. High field NMR magnetometry probes are commonly realized with solenoidal coils wrapped around a sample of natural rubber or water (for ^1H nuclei) [106], heavy water (for ^2H nuclei) or helium (for ^3He nuclei) [95, 97]. The coil is interfaced to the electronics via matching and tuning capacitors in order to implement a resonator at the Larmor frequency and maximize the SNR. Commercial NMR magnetometers generally consist of a main electronic unit and a set of probes capable of variable-frequency operation, whose combined range covers frequencies up to 1 GHz, corresponding to magnetic fields of about 23 T (i.e., the highest static magnetic field produced by commercial superconducting magnets today) [107, 108].

In the design and fabrication of the probes, the search for non-magnetic packaged discrete electronic components, the limited space in which these shall be placed, and their potential influence on the field homogeneity are practical problems to which manufacturers have to dedicate considerable attention. In this Chapter we show the use of complementary-metal-oxide-semiconductor (CMOS) micro-chips in probes aimed at NMR magnetometry of high fields. The electronics needed at the front end of the probe is entirely placed on a single 1 mm² chip, drastically reducing the number of components to be placed in close proximity to the sensitive volume of the probe. Besides allowing for a design with lower and/or more predictable field distortions, integrated circuit solutions reduce in the long term fabrication and design costs, especially in the implementation of multichannel probes.

The first CMOS probes for NMR magnetometry used a rubber sample placed on integrated planar microcoils [29, 96]. This approach achieved a magnetic field resolution in the order of 50 ppb/Hz^{1/2} at 7 T. Recent developments demonstrated the use of CMOS transceivers for compact NMR probes where external resonators are combined with integrated electronics [13, 16, 21]. Among these, we have previously shown the design of a broadband single-chip CMOS transceiver for multi-frequency compact probes, demonstrating its use for multi-nuclear spectroscopy [21].

In this Chapter we describe a single-chip transceiver with broadband IQ demodulation capabilities and show its use in variable frequency probes aimed for magnetometry. First, a combination of the transceiver with a modified version of the PT2026 main electronic unit (Metrolab Technology SA, Switzerland) is synthesized. We experimentally demonstrate state of art measurements having effective resolutions as high as 0.5 ppb/Hz^{1/2} of a 7 T magnetic field. Later, we show that the thermal noise floor of the coil is below the fluctuations of the magnetic field, which is the main factor limiting the measurement resolution in the experimental conditions. We thus implement a compact 2-channel probe for high resolution simultaneous magnetometry, enabling a direct measurement of the thermal noise limited magnetic field resolution. The achieved performance is of 0.06 ppb/Hz^{1/2} for probes employing samples of 500 nL of water in a magnetic field strength of 7 T.

3.3 Experimental Setup

3.3.1 Description of the integrated circuit

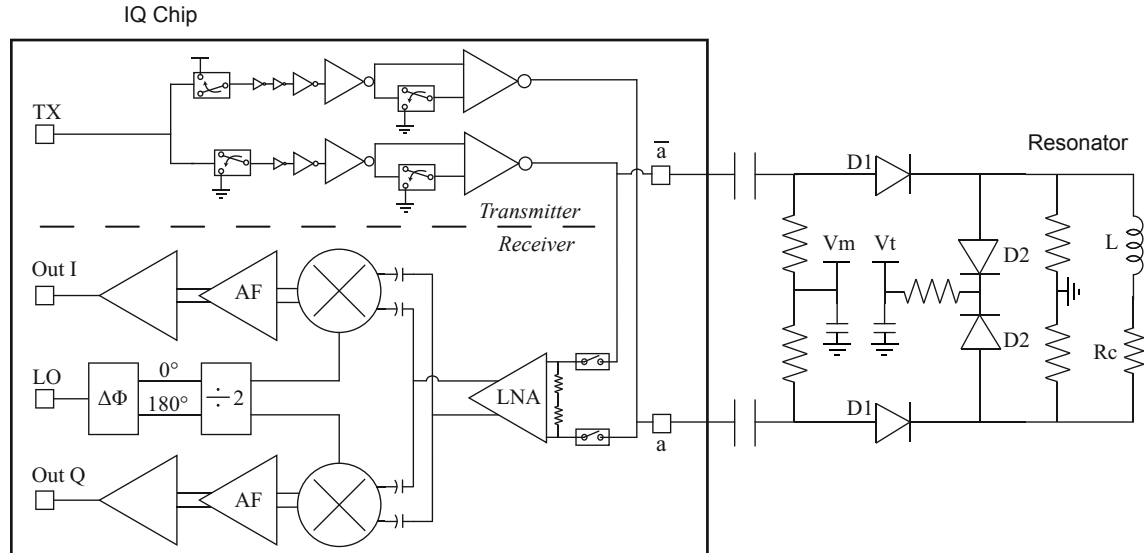


Figure 3.1: **Schematics of CMOS-based variable frequency probe.** Block diagram of our IQ transceiver and external excitation/detection resonator, where L and R_c represent the inductance and resistance of the inductor employed. The tuning and matching capacitances are given by reverse-biased D1 (matching) and D2 (tuning) varicap diodes, and are regulated by the control voltages V_m and V_t . V_m is negative and V_t positive, their absolute value ranging between 0 and 30 V. The resonator topology is the same as the one illustrated in Chapter 2.

Fig. 3.1 shows a block diagram of the probe, where the integrated electronics is interfaced with external variable-frequency resonators. The working frequency of the resonator is adjusted by DC voltages, regulated by a digital to analog converter (DAC) acting on reverse biased variable capacitance diodes (BB181 (D1) and BB182 (D2), NXP Semiconductors). The use of such variable frequency probes for multinuclear spectroscopy is described in Chapter 2. Fig. 3.2 shows a photograph of the single-chip transceiver.

The single-chip transceiver, which consumes about 40 mW, consists of an RF power amplifier, an RF low-noise preamplifier, a $(\pi/2)$ broadband phase shifter, two frequency mixers, two audio-frequency (AF) amplifiers, and fully integrated transmit-receive switches. The working principles of switches, transmitter, and receiver are described in Chapter 2 and Appendix B. The $(\pi/2)$ shifter is realised dividing by two the frequency of two counter-phase channels. First, a π phase shift is generated on-chip using two inverter chains whose number of inverters differs by a unit and a dummy inverter is used to compensate the relative delay. Then, division by two using true single-phase clocking (TSPC) dividers is implemented [109]. This topology of digital dividers is broadband, but the quality of the divided signal deteriorates rapidly for frequencies below 10 MHz [110]. In our design, we tested the phase shift between the I and Q output channels inducing a continuous signal at the receiver input, and we measured an error

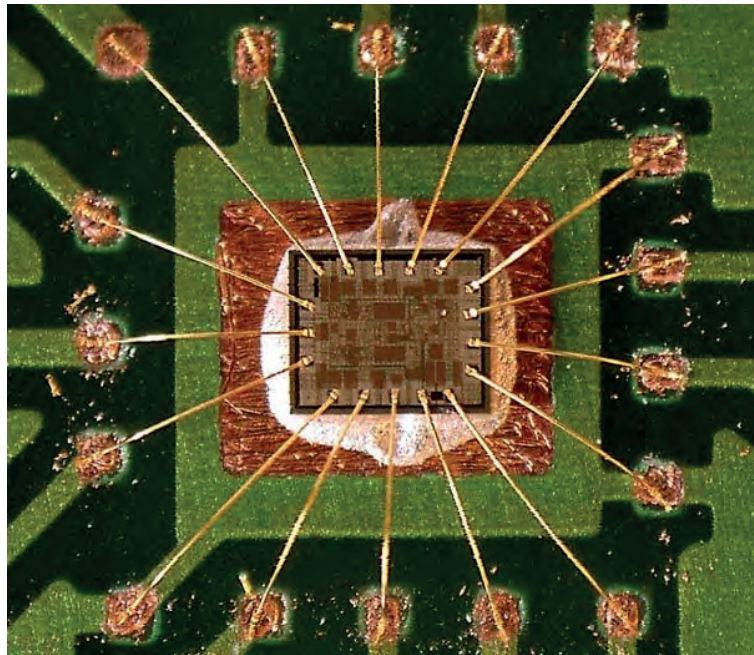


Figure 3.2: **IQ single-chip transceiver.** Photograph of the single-chip transceiver after wire bonding to the host PCB. The micro-chip is first glued with a conductive paste to a metallic ground plane and then opportunely wire-bonded. After this operation, the circuit and the bonding wires are covered with hard epoxy.

of about 4° at 3 MHz and 0.3° at 1 GHz. The transistor level schematics is shown in Appendix B.

3.3.2 Description of the main unit

Fig. 3.3a shows a picture of the PT2026 main electronic unit, Fig. 3.3b shows its $1.6 \times 1.2 \times 23 \text{ cm}^3$ probe, and Fig. 3.3c shows a block diagram of the magnetometer. A pulse generator determines pulse width and repetition rate acting on the transmit-receive (TX/RX) switches integrated on the IQ microchip. The RF generator is designed to switch between two different frequencies, one used for excitation in TX mode and the other used to demodulate the NMR signal in RX mode. Once the field is approximatively determined, the Larmor frequency ν_0 is used in TX mode avoiding off-resonance effects. This double frequency approach allows one to use pulse lengths of the order of $50 \mu\text{s}$ and intermediate frequencies (IF) of the order of 100 kHz at no costs in terms of SNR. A 16 bits, 2 MHz analog to digital converter (ADC) translates the NMR signal in the digital domain. A micro-processor (μP) and a digital signal processing (DSP) unit complete the system. An automated field-search algorithm can be used to scan over the excitation frequency in order to automatically find the value of the magnetic field.

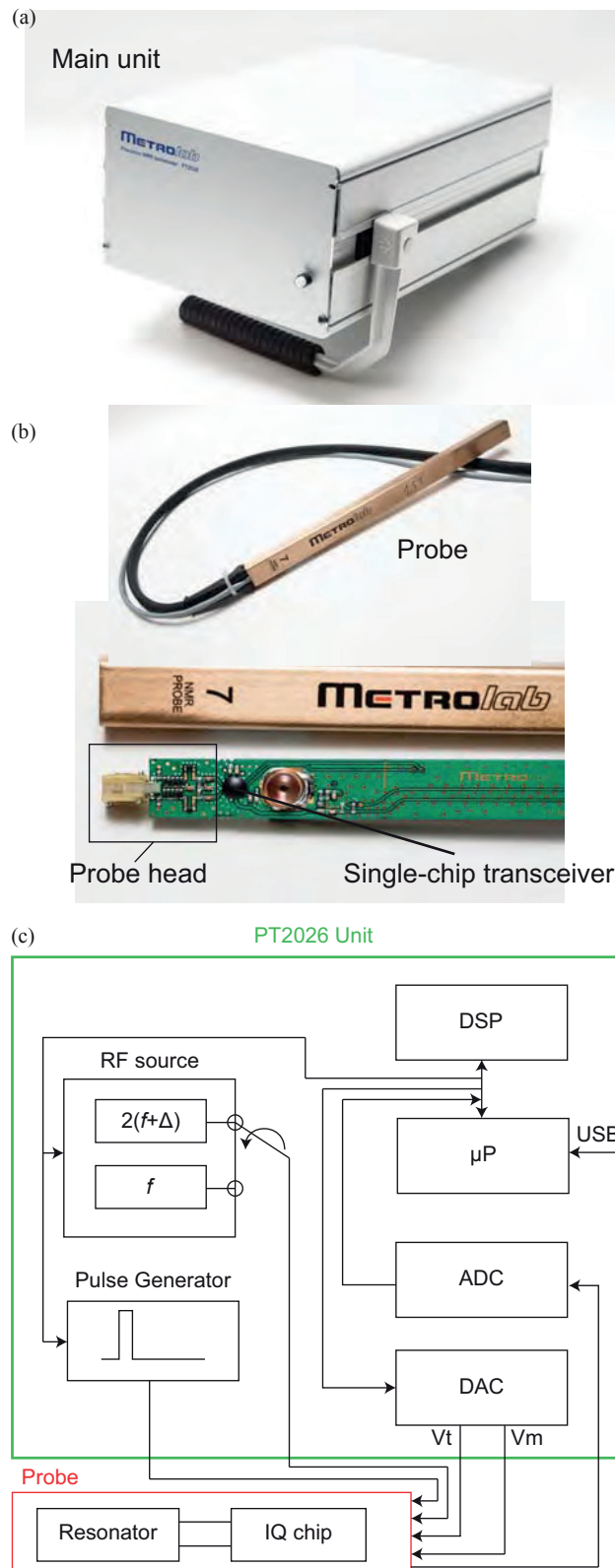


Figure 3.3: **Magnetometry unit.** (a) Picture of the PT2026 unit of MetroLab. (b) Pictures of a prototype of commercial probes employing our CMOS transceiver. (c) Block diagram of teslameter.

3.3.3 Data processing

The NMR signal decays in exponential-like fashion and with relaxation times that depend on the sample nature and on the field distortions within the sample region. Before performing the FFT the signal is multiplied by an exponentially decaying function. In order to maximize the SNR, the filter decay time T_m and the NMR relaxation time T_2^* have to be equal [62].

Once the field value is identified, the measurement is set with an IF frequency of about 80 kHz in order to escape from the $1/f$ noise (whose corner frequency is at about 20 kHz). The PT2026 typically works with one single RX input, in this case either I or Q, to perform its automated functioning. In order to fully exploit the capabilities of our devices, the I and Q NMR signal are acquired by an external NI PCE-6259 acquisition board (as shown in Fig. 3.3c) connected to a PC, which we use for on-line data processing that include matched filters (custom codes are based on National Instruments LabVIEW). The software uses the PeakFinder.vi function to determine the position of the most pronounced peak in the FFT module (which constitutes the direct measurement of the magnetic field).

We separately implemented a software to simulate our experiments and determine the expected performance for a given signal amplitude A , a signal relaxation time T_2^* , and a noise spectral density n . In these simulations the NMR signal is replaced by exponentially decaying sinusoids and the noise is pseudo-randomly generated. In this way it is possible to study what is the precision expected from a measurement as limited by the thermal and electronic noise of the probe. An analytical expression of the measurement resolution was previously derived in agreement to the Cramer-Rao lower bound [111–113]. The same expression is derivable from standard statistics by computing the uncertainty on the frequency parameter of a noisy Lorentzian fit [114–116]. In line with these observations the following expression agrees with the simulated resolutions over a large range of signal relaxation times and SNR:

$$Resolution [Hz] = \frac{n\Delta\nu^{3/2}}{s_0} \quad (3.1)$$

where $\Delta\nu$ is the linewidth of the resulting Lorentzian peak, s_0 the signal amplitude at time $t = 0$ (in Volts), n the noise floor of the FFT (in $V/Hz^{1/2}$), and a single repetition of the experiment is considered.

3.3.4 Standard Probe Heads

To evaluate the performance of the magnetometer, we tested probes at fields $B_0 \approx 7.05$ T ($\nu_0 \approx 300$ MHz) and $B_0 \approx 1.4$ T ($\nu_0 \approx 60$ MHz). Standard commercial probe heads (shown in Fig. 3.3b) consist of solenoidal coils realized with an enameled copper wire ($\phi = 100$ μm). The solenoid can contain natural rubber, sylgard (PDMS), or pure water. The probe used for lower fields can measure from 1.1 T to 3.5 T (47 MHz to 150 MHz) and its coil has 8 loops with inner diameter 3 mm. The probe used for higher fields can measure from 3.3 T to 10.6 T (140 MHz

to 450 MHz) and its coil has 2 loops with inner diameter 3 mm. The typical relaxation times obtained (at best shimming of the field) with these probes are of about 1-2 ms for natural rubber and sylgard (originated mainly by dipolar interactions within these solid materials, which are only partially averaged by motional narrowing) and 20 ms for water (originated mainly by macroscopic field distortions in the sample region).

3.4 Results

3.4.1 Resolution in DC field measurements

Experiments with excitation pulse lengths of 35 μ s and repetition times of 50 ms are acquired and averaged in groups of 20 (we fix a total time of 1 s for a single measurement). The pulse length is chosen such that the signal is maximized at steady state with the chosen repetition time. With these parameters, the corresponding signal amplitude is about 1 V with a noise floor of 8.5 μ V/Hz^{1/2} for all the probe heads. The acquisition rate is fixed at 650 kHz. The data are processed on-line, the magnetic field values are extracted as previously described, and a comparison among probes is based on 300 successive measurements (5 minutes of operation). The standard deviation of this collection of measurements corresponds to the resolution achieved over 1 s and with a bandwidth from 3 mHz to 1 Hz. In Table 3.1 we reported the resolution in Hz/Hz^{1/2}, T/Hz^{1/2}, and part per billion (ppb/Hz^{1/2}) with respect to the field magnitude. What shown in Table 3.1 corresponds to the state of art of this instrumentation [98, 107].

$B_0 = 7 \text{ T } (\nu_0 \simeq 300 \text{ MHz})$			
Sample Material	Natural rubber	Sylgard	Water
T_m, T_2^* [ms]	1.5	2	20
STD [nT/Hz ^{1/2}]	4.5 (0.09)	4.5 (0.09)	2.5 (0.003)
STD [Hz/Hz ^{1/2}]	0.2 (0.006)	0.2 (0.04)	0.1 (0.0001)
STD [ppb/Hz ^{1/2}]	0.7 (0.02)	0.7 (0.01)	0.5 (0.0004)
$B_0 = 1.4 \text{ T } (\nu_0 \simeq 60 \text{ MHz})$			
Sample Material	Natural rubber		
T_m, T_2^* [ms]	1.5		
STD [nT/Hz ^{1/2}]	14 (0.14)		
STD [Hz/Hz ^{1/2}]	0.6 (0.006)		
STD [ppb/Hz ^{1/2}]	10 (0.1)		

Table 3.1: Field measurement resolution obtained and values of the optimal matched filter decay time. In parenthesis: values simulated at parity of relaxation time, signal amplitude, noise spectral density, averaging.

Thanks to the larger number of turns of the solenoidal coil used at 1.4 T, the NMR signal

amplitude at 7 T and at 1.4 T are approximately the same. Since the input equivalent noise is very similar, the magnetic resolution values (expressed in $\text{nT}/\text{Hz}^{1/2}$ and in $\text{Hz}/\text{Hz}^{1/2}$) are also similar. In Table 3.1 we show a comparison between the resolution experimentally obtained and the one expected if limited by the thermal and electronic noise of the probe (in parenthesis). As we can see, for all probes the achieved resolution and the expected value differ by more than one order of magnitude.

We directly measured the frequency noise of DAQ board and RF generator. In order to determine the noise due to the DAQ system we acquired a 50 mV sinusoidal signal at 50 kHz from a HP 33120A arbitrary waveform generator and measured its frequency for repetitions identical to the ones used to produce Table 3.1. The equivalent frequency noise of the DAQ system was found to be better than $2 \text{ mHz}/\text{Hz}^{1/2}$. In order to measure the frequency noise due to the RF generator we have used an external second RF source to induce, with an inductor placed in proximity of the detection coil, a signal into the probe head (placed outside of the magnet). By adjusting the RF power in order to match the NMR signal amplitude and by using the same repetitions and matched filters as in Table 3.1 we were able to determine whether the frequency noise of the RF source was significantly affecting our measurements. Fig. 3.4a shows a direct comparison among the monitoring of our 7 T magnetic field (Bruker 300) and the monitoring of the frequency of an Anritzu MG3633A RF source. As we can see, the frequency noise of the RF source is significantly lower than the magnetic field noise. Fig. 3.4b shows the progressive standard deviation of the two data series. Overall, these results indicate that the main limitations to the obtained precision shown in Table 3.1 have origin in the magnetic field.

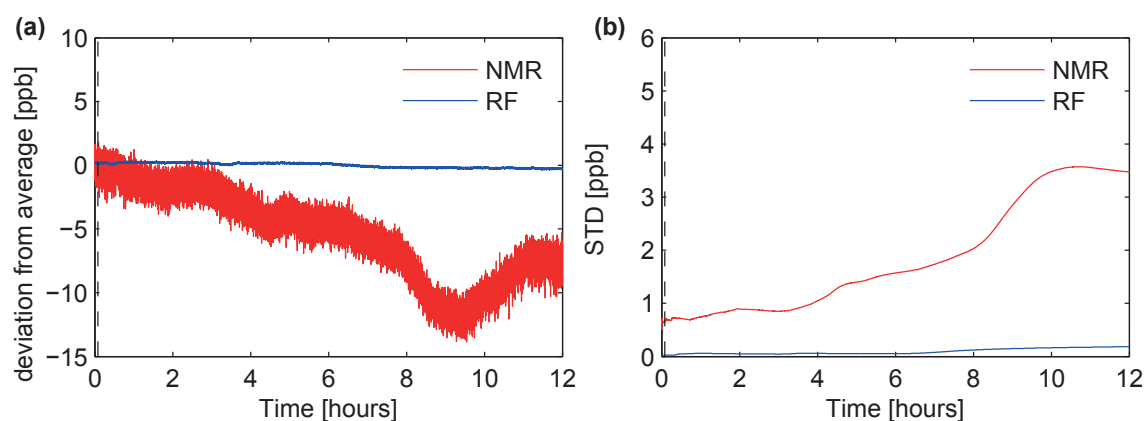


Figure 3.4: **12 hours monitoring of RF and DC field.** (a) Series of measurements of our 7 T magnetic field with a water probe (red) and monitoring of the frequency noise of an Anritzu MG3633A RF generator used as signal source (blue). Measurements are taken every second and expressed as deviation (in ppb) from an initial value set to 0. (b) Progressive standard deviation of (a). The black dashed line in (a) and (b) indicates the time scale used to produce Table 3.1.

3.4.2 Compact multichannel field monitoring probes

In order to obtain a direct measurement of the thermal noise during magnetometry operation we implemented a compact two-channel probe aimed for simultaneous DC field monitoring. The use of multiple probes is necessary to operate a subtraction of the common fluctuations, thus decoupling contributions of field fluctuations and RF frequency instability (common in the two channels) from the thermal noise (uncorrelated in the two channels).

In Table 3.1 it is shown that the water sample of a high field magnetometer may easily result oversized, since the effective experimental resolution obtained can be limited by field fluctuations. At the same time, the use of small samples is advantageous for the resulting probe dimension, and crucial for applications such as magnetic field gradient measurements in MRI magnets [91, 117]. Our 2-channel probe employs samples of 500 nL of water. Despite the small sample volume, the achieved instrument resolution of 0.06 ppb/Hz^{1/2} (defined as the thermal noise-floor limit) goes beyond the typical value of magnetic field fluctuations (see below).

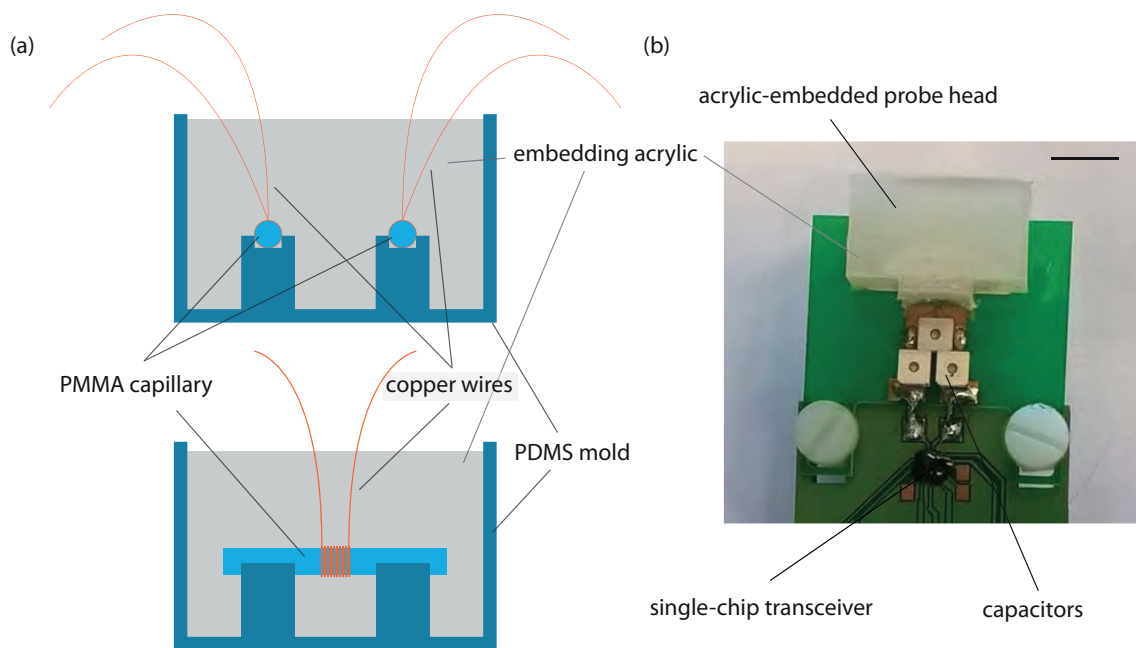


Figure 3.5: **2-channel probe for simultaneous field monitoring.** (a) Schematics in section view of the two-channels probe head at the end of the fabrication process. (b) Photograph of the resulting probe. In between (a) and (b) the PDMS mold is removed, and the acrylic embedded coils are fixed and soldered to the PCB. An identical circuit on the other surface of the PCB implements the second channel. Scale bar is 1 cm.

Each channel is based on a 10 loops enameled copper wire ($\phi = 100 \mu\text{m}$) microsolenoid wrapped around a PMMA capillary (ID=550, OD=700, paradigmoptics) filled with pure water (Sigma Aldrich). Given the small size of the sample, a susceptibility matching strategy is necessary to achieve long signal relaxation times [57]. The fabrication process consists of

four main steps: (1) A first mold aimed at structuring a second PDMS (sylgard 184) mold is 3D printed (Clear Resist, Formlabs printer), exposed to UV for 30 minutes, and hard backed at 80 °C for two hours; (2) A sylgard mold is produced by casting and curing at 80 °C for one day; (3) 10 loops microsolenoids are wrapped around PMMA capillaries, filled with pure water and sealed with a tube sealing compound (Chā-seal) at extremities; (4) The capillaries are inserted in the appositely designed sylgard slots included in the mold, and an acrylic resin (Paladur, Heraeus Kulzer, Germany) is cast to embed the solenoids in a susceptibility matched environment (Fig. 3.5a). After removal of the sylgard mold, the resulting probe head is fixed and soldered to a PCB on which variable capacitors (Johanson Manufacturing, capacitor trimmer) are used to tune and match the two resonators at the desired frequency (Fig. 3.5b). The probe head is constituted by two specular circuits, one realised with the top layer and the other with the bottom layer of the printed circuit board. Thanks to the excellent matching in terms of magnetic susceptibility between copper, acrylic, and water [71], the probe can be shimmed to obtain relatively long signal decays (about 20 ms relaxation time), similarly to what previously reported in analogous setups at similar volume scales [68]. Given the small distance between the centers of the two coils (1.5 mm), the two channels can be simultaneously shimmed.

In each channel a single RF generator is used for both excitation and down-conversion. Thanks to the small size of the coil, excitation pulses of 8 μ s are sufficient to maximize the NMR signal, thus allowing for relatively high IF frequencies (larger than the $1/f$ noise corner frequency) and negligible off-resonance effects. The two RF generators (Anritzu MG3633A and Stanford SG384) are frequency locked, and their frequency stability (affecting simultaneously each single channel) is measured at about 6 mHz/Hz^{1/2} (0.02 ppb/Hz^{1/2} of the 7 T field) over 5 minutes of operation.

Fig. 3.6a shows the time domain NMR signal (I and Q) of a single channel with no exponential filters applied. As we can see, the signal amplitude of about 1 V decays with a relaxation time of about 20 ms. The measured thermal noise floor is about 70 μ V/Hz^{1/2}, and the simulated thermal-noise limited resolution of each single channel at 7 T is about 0.03 ppb/Hz^{1/2}. Fig. 3.6b shows the real and imaginary parts of the FFT, whose modulus is used to measure the magnetic field. In Fig. 3.6c we show a series of 5 minutes of measurements (1 s per measurement) at 7 T, plotted as deviation from mean values. As we can see, the standard deviation of the field value for a single channel (red and blue data) is of about 0.16 Hz/Hz^{1/2}, corresponding to a resolution of 0.5 ppb/Hz^{1/2} (as in Table 3.1). As indicated by simulations, the use of a 500 nL water sample is already sufficient to achieve a resolution beyond the field fluctuations. We can directly visualize the real thermal noise limit of the probe by looking at the standard deviation of the difference of the two measured values (Fig. 3.5c, black data), which is expected to be about 0.04 ppb/Hz^{1/2}. The measured value of 0.08 ppb/Hz^{1/2} confirms the expectations within a factor two, and indicates a single channel thermal-noise limited resolution of 0.06 ppb/Hz^{1/2}. The difference between the expected value and the measured one may result from inevitable discrepancies between the assumptions in pseudo-random simulations and the real shape of the NMR signal.

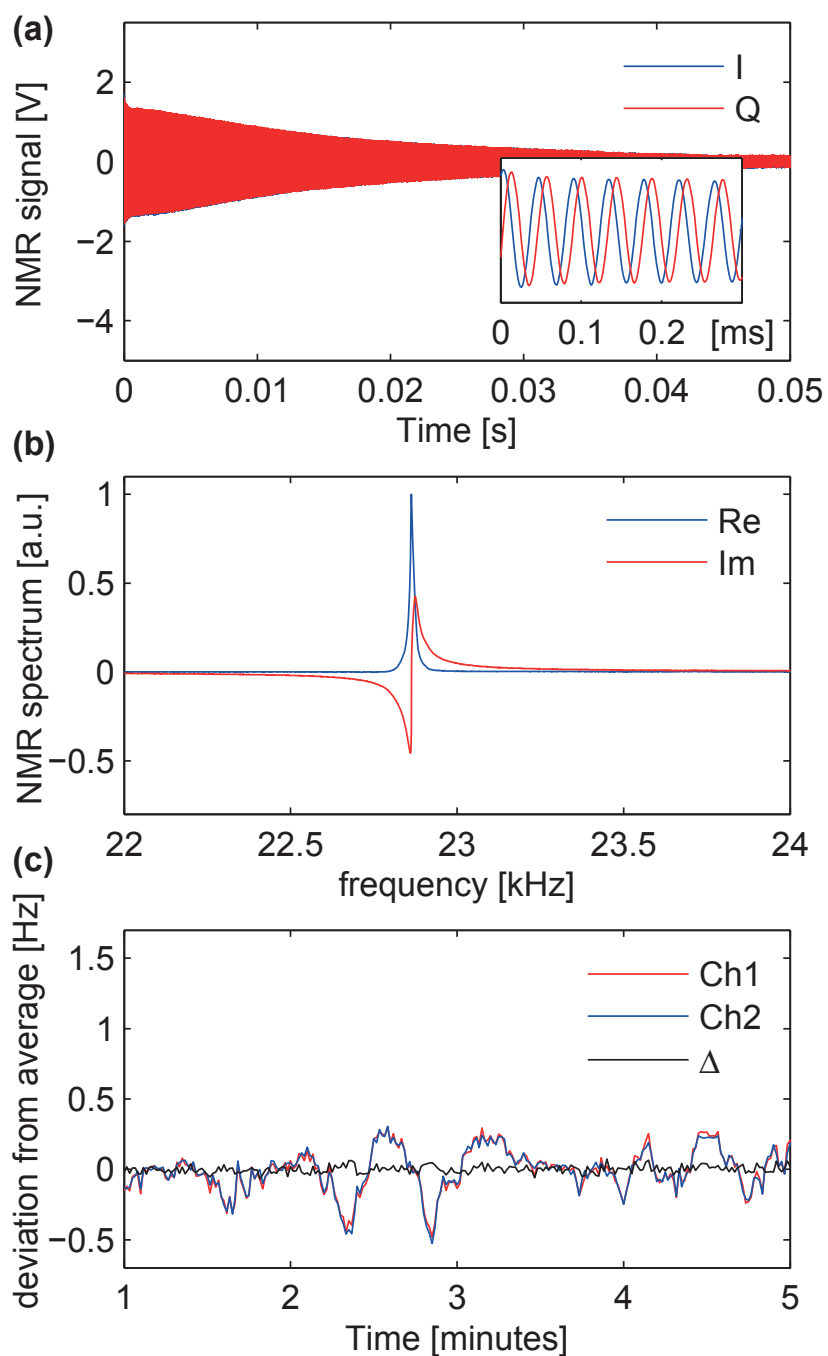


Figure 3.6: **2-channel field monitoring**. (a) Time domain I (blue) and Q (red) NMR time-domain signals resulting using the acrylic-embedded 500 nL water probe. (b) FFT real (blue) and imaginary (red) parts. (c) Channel 1 (blue), channel 2 (red), difference Δ among channels (black), resulting from a 5 minutes series of magnetic field measurements (taken every 1 s) in a Bruker 7 T cryo-magnet.

3.4.3 Absolute accuracy

The absolute accuracy of an NMR magnetometer is ultimately limited by the uncertainty in the gyromagnetic ratio value of the nucleus used (in our case ^1H). In principle, the accuracy in the value of frequency of the RF source is also a potential limiting factor. However, it is nowadays possible to obtain low cost frequency references with accuracies well beyond the uncertainty of the gyromagnetic ratio value [79]. Since in NMR magnetometry the nuclei are typically located inside molecules in the gaseous, liquid or solid state, the absolute accuracy is also limited by the uncertainty in the shielding parameter value of the nucleus under investigation in the particular chemical and physical environment. More macroscopically, the absolute accuracy is also limited by the uncertainties in the static magnetic field distortions caused by the probe elements. Such distortions depends on the susceptibility, shape, and orientation with respect to the magnetic field of sample itself and the nearby objects [93, 97, 118]. The gyromagnetic ratio of the ^1H nucleus (i.e., the proton) is given by $(\gamma/2\pi) = 42.577\,478\,92(29)$ MHz/T, which corresponds to a relative standard uncertainty of about 7 ppb [79]. Since bare protons are very unpractical for NMR magnetometry, the ^1H nuclei in a spherical sample of water at 25 °C are commonly used for high accuracy NMR magnetometry. The shielding parameter for the ^1H nucleus in this sample is $25.691(11) \cdot 10^{-6}$, giving an effective gyromagnetic ratio of $42.576\,385\,07(53)$ MHz/T, which corresponds to a relative standard uncertainty of about 13 ppb [79]. The temperature dependence of the shielding parameter is $-10.36(30) \cdot 10^{-9} \text{ }^\circ\text{C}^{-1}$ from 5 °C to 45 °C [119].

However, in our probes, the main limitation to the absolute accuracy is the lack of precise knowledge of the susceptibilities values for the materials surrounding the sample volume and of the sample itself. The largest values for the susceptibilities of ordinary diamagnetic and paramagnetic materials is about 10^{-5} [71, 120], which would determine maximum field distortions of about 10 ppm. Consequently, a rather pessimistic estimation of the absolute accuracy would be 10 ppm.

3.4.4 Conclusions

In this work we have seen that broadband CMOS single-chip transceivers are valid and versatile tools to assist the manufacturing of NMR probes aimed for high field magnetometry. A combination of single-chip transceivers and standard commercial probe-heads shows state of art performance. The use of CMOS transceivers to implement NMR probes for high field magnetometry is trade-offs free in terms of performance, and it offers technology-related practical advantages.

One practical advantage is the reduced size of the overall electronics needed, and the consequent replacement of numerous components in proximity of the probe head. Due to the small size of the micro-chip, and to its low power consumption, the introduced field and temperature-related distortions are reduced, and thus expected to be advantageous for eventual high accuracy measurements. A second advantage concerns the costs in the long term, reduced by both materials costs and human power needed to implement each probe: a proce-

dure considerably simplified since a single chip can be used to cover the whole high field range. Finally, the use of single-chip transceivers is certainly expected to ease the implementation of array of probes (we have shown an example of compact robust 2-channel probe), currently used to map MRI magnets, and under study for the monitoring of MRI field gradients [121].

4 NMR spectroscopy of single sub-nL ova with ultra-compact single-chip probes

4.1 Abstract

Nuclear magnetic resonance (NMR) spectroscopy enables non-invasive chemical studies of intact living matter. However, the use of NMR at the volume scale typical of microorganisms is hindered by sensitivity limitations, and experiments on single intact organisms have so far been limited to entities having volumes larger than 5 nL. In this chapter we use the ultra-compact single-chip probe presented in Chapter 2 to make a very first NMR-based spectroscopic experimental study of individual sub-nL ova of microorganisms: here we show NMR spectroscopy experiments conducted on single intact ova of 0.1 and 0.5 nL (i.e. 10 to 50 times smaller than previously achieved), thereby reaching the relevant volume scale where life development begins for a broad variety of organisms, humans included. Performing experiments with an inductive ultra-compact single-chip NMR probe we demonstrate that the achieved limit of detection (about 5 pmol of ^1H nuclei) is sufficient to detect endogenous compounds. Given the high number of species developing at the sub-nL scale, we could study ova of two different species of microorganisms. As hard facts, we show both spectral differences among the two species and among individual samples. We argue that endogenous compounds other than lipids are detected. We state that the sensitivity achieved in this study corresponds to the level of metabolic variations in developing mammalian embryos, clearly opening the way for the application of NMR spectroscopy to the non-invasive study of individual subnanoliter zygotes and their metabolism. Overall, the findings suggest that single-chip probes like the one presented in this thesis are promising candidates to enable NMR-based study and selection of microscopic entities at biologically relevant volume scales.

This chapter is a minor variation of the publication "NMR spectroscopy of single sub-nL ova with ultra-compact single-chip probes" [122].

4.2 Introduction

Nuclear magnetic resonance (NMR) is a well established spectroscopic technique widely employed in physics, chemistry, medicine, and biology. It allows for experiments on living matter [123, 124], whose relevance in biology is proven by developments such as *in vivo* protein structure determination [125], metabolic profiling [126], visualization of gene expression [127], and latent phenotype characterization [128]. Despite its advantages, NMR suffers from a significantly lower sensitivity with respect to other methods. As a result, experiments are often restricted to large ensembles of cells [123, 125, 126, 128].

Single cell studies are necessary to investigate heterogeneous phenomena within a cell population [129–131]. Recently, a number of techniques were applied to intracellular metabolic profiling at single cell scale, all having different limitations and degree of invasivity. For instance, mass spectrometry and fluorescence labeling allow for high sensitivities, but require cellular content extraction or selective labeling with fluorophores [129, 131]. Questions concerning invasivity stimulated the coin of the biological equivalent of the so called observer effect, referring to the inability to separate a measurement from its potential influence on the observed cell [131]. In this regard, NMR is one of the most promising techniques for studies of intracellular compounds in untouched living entities (i.e., with extremely weak physical and chemical perturbations) [123, 129].

The application of NMR to intact individual microscopic biological entities was previously reported down to a volume of 5 nL. The first single-cell NMR experiments were performed on *Xenopus laevis* ova [132] which have volumes of about 1 μ L. Later, single giant neurons of *Aplysia californica*, with volumes of approximately 10 nL, were studied [133]. The particularly large volumes of these cells allowed several pioneering studies such as the profiling of highly concentrated metabolites and their subcellular localization [134, 135], imaging of *Xenopus laevis* cleavage [136] and neurons structure [137], and study of water diffusion properties within the cytoplasm and nucleus [132, 133, 138–140]. Recently, also spectroscopy of a single adult *C. elegans* worm (about 5 nL volume) was reported [141].

In this chapter we report, for the first time, NMR-based spectroscopy of single untouched sub-nL ova, specifically describing experiments on the tardigrade *Richtersius coronifer* (*Rc*) and the nematode *Heligmosomoides polygyrus bakeri* (*Hp*). These ova are just two of the many models present at the sub-nL scale (Fig. 4.1a), which include numerous species of microorganisms, echinoderms, and mammals (humans included) [142]. *Rc* ova are spherical with conical processes on the cuticular surface of the egg shell and have a typical volume of 0.5 nL (Fig. 4.1b). *Hp* ova are ellipsoidal and have a typical volume of about 0.1 nL (Fig. 4.1c). NMR spectroscopy of sub-nL biological samples is both a volume and concentration limited problem, setting severe constraints on the required spin sensitivity. Here we employ a recently developed single-chip integrated inductive NMR probe [21] (this reference corresponds to the content previously presented in Chapter 2) entirely realized with a commercially accessible complementary-metal-oxide-semiconductor (CMOS) technology, where the combination of a low noise transceiver and a multilayer microcoil allows for high spin sensitivities in sub-nL volumes (Fig. 4.1d). In brief, the entire NMR probe occupies an area of about 1 mm², it has

a sensitive region of about 200 pL (on top of the microcoil) with a spin sensitivity at 7 T of about 1.5×10^{13} spins/Hz^{1/2}, and its planar geometry allows for a relatively easy access to the sensor. In order to use the device for the spectroscopy of sub-nL ova of microorganisms, we manually placed the sample in the sensitive region of the probe using a polystyrene cup filled by agarose gel (see Methods). Figure 4.1e describes the assembled probe where single ova are in contact with the microcoil surface and embedded in the gel. This setup systematically allows for experimental times as long as one day.

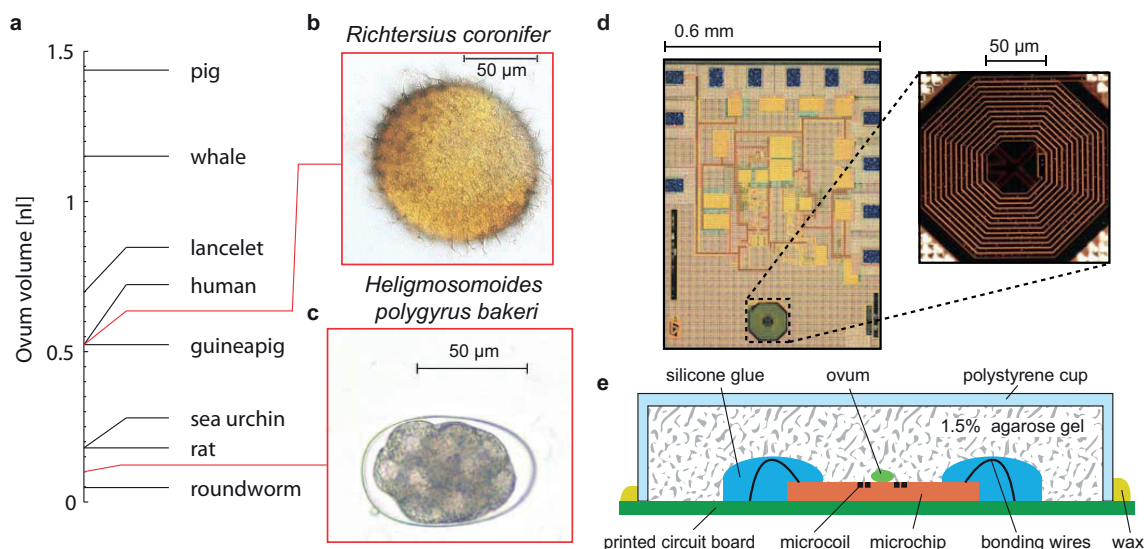


Figure 4.1: **Samples and Setup.** (a) Approximate volumes of ova of selected animals. (b-c) Typical bright field images of the ova studied in this work. (d) Photographs of the integrated microchip and microcoil (details in Ref. [21]). (e) Schematic representation of the single ovum probe in section view.

4.3 Results

4.3.1 Linewidth in *Rc* ova

Figure 4.2a shows three ¹H NMR spectra obtained at 7 T (300 MHz) from single *Rc* ova embedded in H₂O-based agarose gels. Due to a measured linewidth of about 70 Hz, the strong water signal (used as internal chemical shift reference at 4.7 ppm [139]) overlaps with nearby resonance lines. The relatively short spin-spin relaxation times typically observed in oocytes explain only partially these broad lines [135, 139, 140] that must be caused by susceptibility mismatches. In order to investigate the origin of the field distortions we performed measurements with an alternative setup enabling the spectroscopy of these samples in pure water and with controlled and reduced hardware-related field distortions (see next subsection). Repeated experiments suggest that the linewidth measured in *Rc* ova is intrinsically related to the sample, probably resulting from microscopic constituents of the ovum introducing susceptibility mismatches whose typical spatial distribution impedes field shimming in the

intracellular region. In line with this observation, previous studies limited to the vegetal cytoplasm of intact *Xenopus laevis* ova attributed similarly broad linewidths (about 0.3 ppm) to the presence of yolk platelets, or other organelles with paramagnetic components, generating local susceptibility mismatches [135]. However, despite the relatively low spectral resolution that characterizes *Rc* ova, the achieved LOD (advantageous in the setup employing the integrated single-chip probe) is sufficient for a qualitative detection of intracellular compounds (Fig. 4.2a).

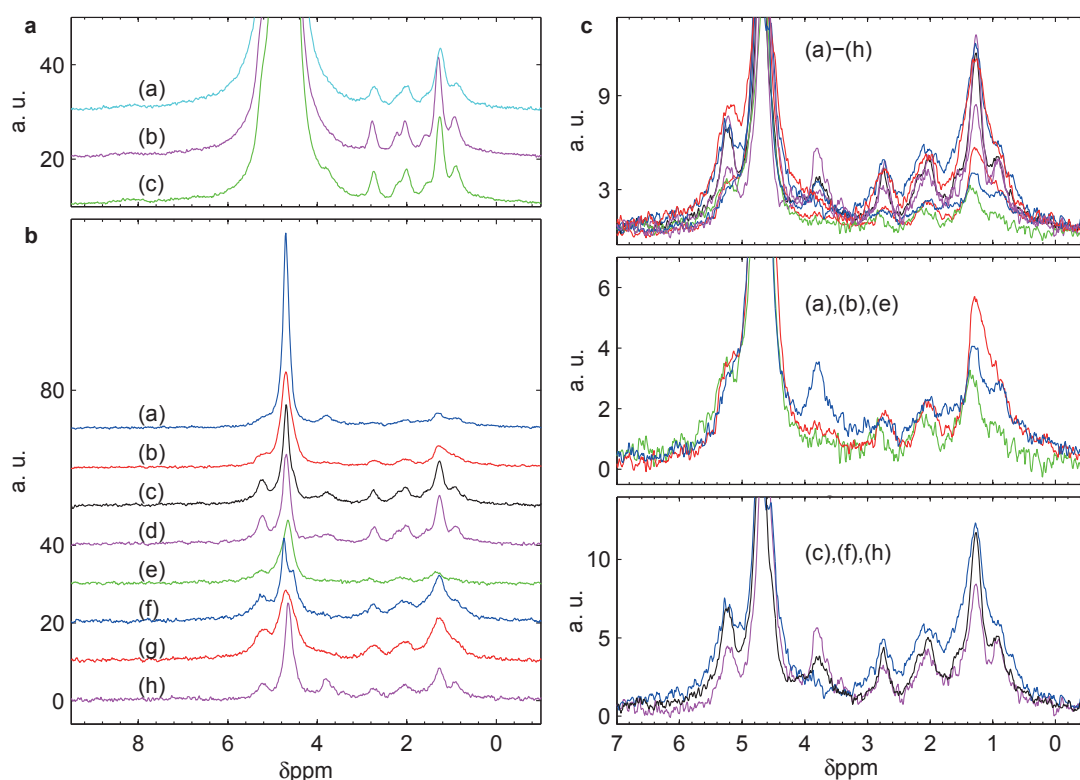


Figure 4.2: NMR spectroscopy of single *Richtersius coronifer* (*Rc*) ova. (a) Three *Rc* single ovum experiments in H₂O-based gels realized by dispersing 1.5% agarose in either M9 buffer (a) or pure H₂O (b-c). (b) Eight *Rc* single ovum experiments in D₂O-based gels realized by dispersing 1.5% agarose in pure D₂O. (c) Detailed comparison of *Rc* ova in D₂O-based gels. Colors refer to the same spectra as in (b).

4.3.2 Experiments on *Rc* ova with an alternative setup

Micro-fabricated microcoils whose copper loops are fully embedded in SU-8 photo epoxy (Bruker Biospin) probably represent the best commercially available alternative to CMOS microcoils. Among the products offered, we selected planar microcoils characterized by 5 copper loops and internal diameter of 50 μm . The resonating microcoil, fine-tuned with variable capacitors (2322-1G, Johanson), is connected to a single chip transceiver identical

to the one used in the fully integrated probe. On top of the microcoil a few microns thick bio-compatible layer acts as protective layer and working surface. In order to analyze liquid samples and single ova, 150 μm diameter PET capillaries having 6 μm thick walls (Venton Medical) are placed on the top of the microcoil in the same direction as the vertical static magnetic field. This particular configuration allows for measured linewidths as narrow as 3 Hz in pure water. Figure 4.3 shows the typical spectra of the liquid within the capillary at a distance of about 1 mm from the ovum and at the ovum position, both after shimming of the magnetic field. The room temperature shim system of our magnet, whose maximum gradient corresponds to about 0.4 Hz/ μm , resulted very effective when the sensitive region was occupied by the liquid sample. On the contrary, when the ovum was aligned to the microcoil, lineshape and linewidth of the water signal remained substantially unchanged for any setting of the shimming system. The measured linewidth at the ovum position is about 0.3 ppm, i.e. about a factor 30 larger than the water peak measured at 1 mm distance from the ovum within the same capillary. This experience, repeated five times, suggests that the linewidth measured in *Rc* ova results from mismatches localized within the sample, whose typical spatial distribution impedes field shimming in the sample region fixing lineshape and linewidth independently from the applied gradients.

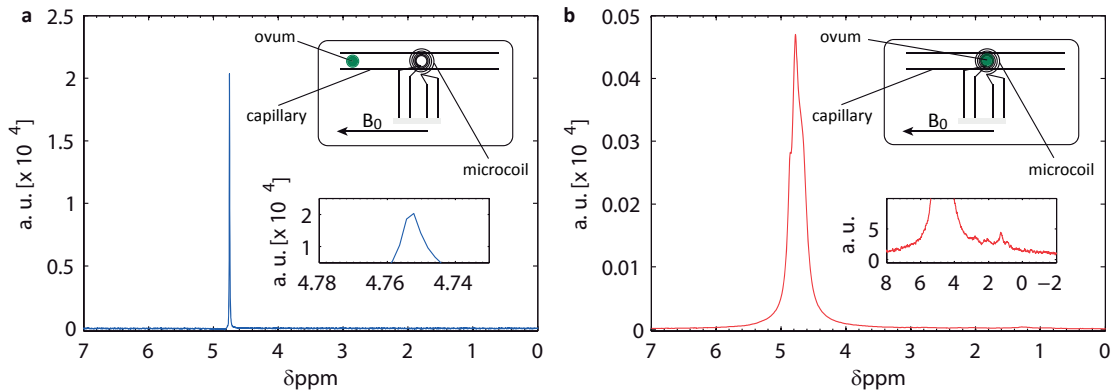


Figure 4.3: **Additional experiments of single *Richtersius coronifer*.** (a) (*Rc*) ova in pure H_2O . Spectrum of about 800 μl of H_2O at about 1 mm from the ovum position resulting from 30 averaged scans. The acquisition time is 1.6 s, and no filters are applied on the time domain signal. The resulting linewidth is about 0.01 ppm, i.e. about 3 Hz (see inset). (b) Spectrum at the ovum position resulting from 18000 averaged scans. The acquisition time is 0.8 s. The resulting linewidth is about 0.3 ppm, i.e. about 90 Hz. Details of the single ovum spectrum are shown in the inset (the time domain data were post-processed by applying an exponential filter with decay of 50 ms in order to improve the signal-to-noise). Both spectra in (a) and (b) are acquired at the best shimmed magnetic field. The experiments are performed with a repetition time of 2 s and a pulse length of 2.5 μs (maximizing the signal).

4.3.3 *Rc* ova spectroscopy

In presence of susceptibility mismatches broadening the water signal it is difficult to apply water suppression techniques without introducing significant spectral artifacts [143]. As an alternative to the use of water suppression techniques we embedded the biological sample in gels based on heavy water (D_2O), thus eliminating the water signal by replacement of water with D_2O . In D_2O -based agarose gels, HDO is formed by proton exchange with the OH groups in the agarose molecule. HDO resonates at about 0.03 ppm relative to the H_2O chemical shift [144] and contributes to the only background signal that is visible in our experimental conditions and time scales (Fig. 4.4). The weaker background signal in D_2O gels (about 100 times smaller than in H_2O gels) is reproducible, allows one to better resolve the resonance lines close to water, and can be used as internal chemical shift reference (at 4.7 ppm as water). We do not exclude that, in presence of the sample, the peak at 4.7 ppm results also from leftover H_2O within the ova.

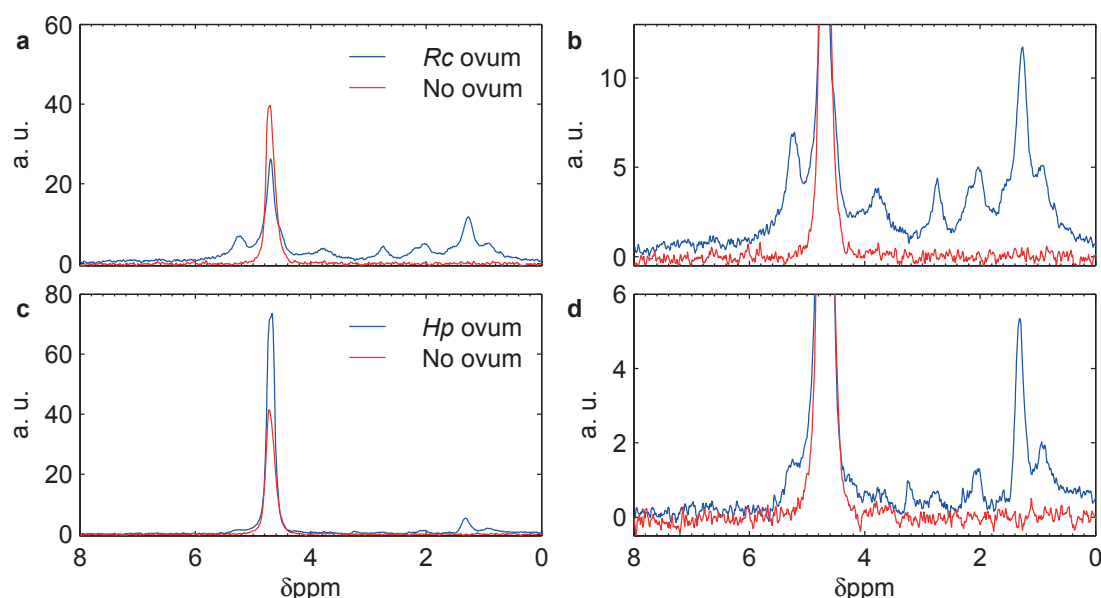


Figure 4.4: **Comparison between single ova experiments in D_2O -based gel and D_2O -based gel background.** (a) Spectra of a single *Rc* ovum in D_2O -based gel and of a D_2O -based gel. (b) Detailed comparison. (c) Spectra of a single *Hp* ovum in D_2O -based gel and of a D_2O -based gel. (d) Detailed comparison.

Figure 4.2b shows NMR spectra of eight single *Rc* ova in D_2O -based gels obtained by dispersing agarose in pure heavy water. These spectra exhibit linewidths and chemical shifts compatible with the ones observed in H_2O -based gels. A detailed comparison among spectra of different ova seem to indicate that the *Rc* ova exhibit a certain degree of spectral heterogeneity (Fig. 4.2c). In what follows we discuss the possible experimental artifacts that could lead to artificial spectral diversities and show a reproducibility study of single ova spectra.

Rc ova are randomly selected from a population where there is no control over fertilization

and/or development stage. Their volume is approximately spherical, with a diameter naturally varying from 100 to 130 μm . As shown in detail by the sensitivity maps described below, the most sensitive region of our excitation/detection microcoil roughly corresponds to a deformed semi-ellipsoid of about 200 pl, i.e. smaller than the *Rc* ova volume. Consequently, the signal amplitude does not depend linearly on the ovum volume. In order to quantitatively estimate the dependence of the signal amplitudes on the natural variability of ova volumes, we performed a numerical integration of the effective sensitivity shown below over spherical volumes (representing *Rc* ova) having diameters of 100 and 130 μm , placed on top of the microcoil, in which an homogeneous spin density is considered. The result of this calculation indicate that the maximum variability of signal amplitude due to different ova volumes is of about 25%. This value slightly increase to about 30% when the smaller sphere is laterally displaced by 15 μm with the respect to center of the microcoil. From this estimation, we deduce that the variability in terms of signal amplitudes shown in Fig. 4.2 (as large as 350%) cannot be explained by the natural variability of ova volumes and/or the ovum-to-microcoil misalignment.

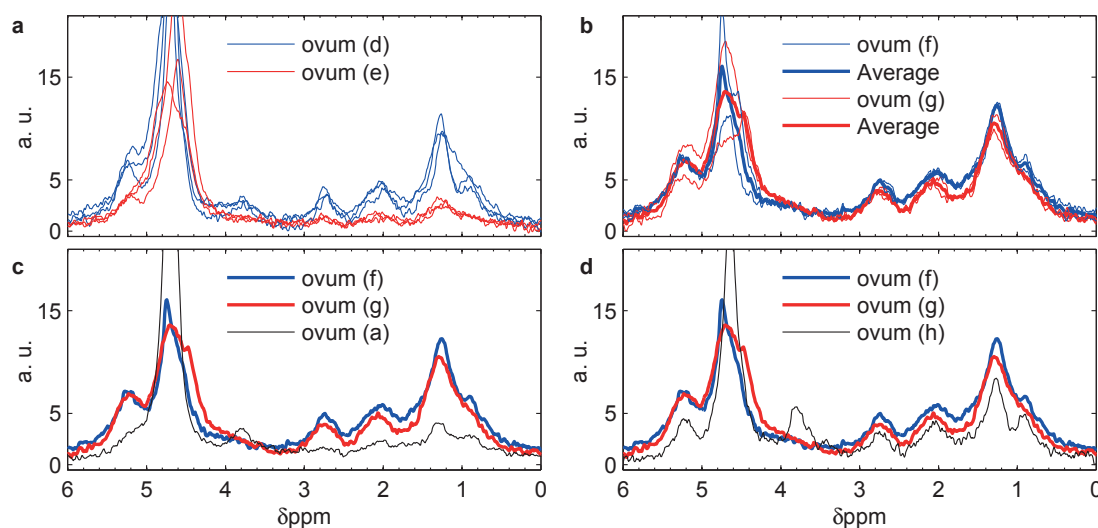


Figure 4.5: **Reproducibility study of *Richtersius coronifer* (*Rc*) spectra.** (a) Measurements of two ova, ovum (d) and ovum (e) as indicated in Fig. 4.2b. Each ovum was arbitrarily repositioned three times within the respective spent gels. Each spectrum results from 12 hours of averaging. (b) Measurements of two ova, ovum (f) and ovum (g) as indicated in Fig. 4.2b. Each ovum was arbitrarily repositioned twice within fresh gels. Each spectrum results from 12 hours of averaging. (c) Comparison of averaged spectra of ova (f) and (g) with spectrum of ovum (a) as indicated in Fig. 4.2b. (d) Comparison of averaged spectra of ova (f) and (g) with spectrum of ovum (h) as indicated in Fig. 4.2b.

Other factors that might provoke artificial heterogeneity among these NMR spectra can be: (1) the non-homogeneous coil sensitivity combined with a non-uniform intracellular chemical composition; (2) the random orientation of the ovum within the structural field inhomogeneous.

generosity of the setup; (3) the presence, upon sample placing, of invisible air bubbles at the microchip-sample-gel interface (see Methods for assembly procedure). In order to investigate these possible sources of artefacts, we performed six additional experiments on four *Rc* ova, in particular on the ova which produced the spectra (d), (e), (f) and (g) shown Fig. 4.2b. Figure 4.5a shows spectra of ovum (d) and ovum (e) after three arbitrary repositioning, realized delicately rotating the ova within the respective spent gels. Although we observe some variations of the linewidths as well as of the signal amplitudes, the dominant spectral features (i.e. the ones between 0 and 4 ppm) are conserved upon sample rotation and change of local environment. Fig. 4.5b shows the result of experiments where both ovum (f) and (g) are repositioned in a fresh gel. As we can see, the dominant spectral features were conserved also upon transfer into fresh gels. Fig. 4.5c and 4.5d compare the averaged spectra of ova (f) and (g) to spectra of ova (a) and (h), showing that the variability in spectra of different ova can be larger than the variability of repeated experiments on the same ovum. Overall, Fig. 4.5 suggests that the observed diversity among spectra of *Rc* ova cannot be attributed only to the manipulation and positioning of the ovum but must be caused, at least partially, by its intrinsic properties.

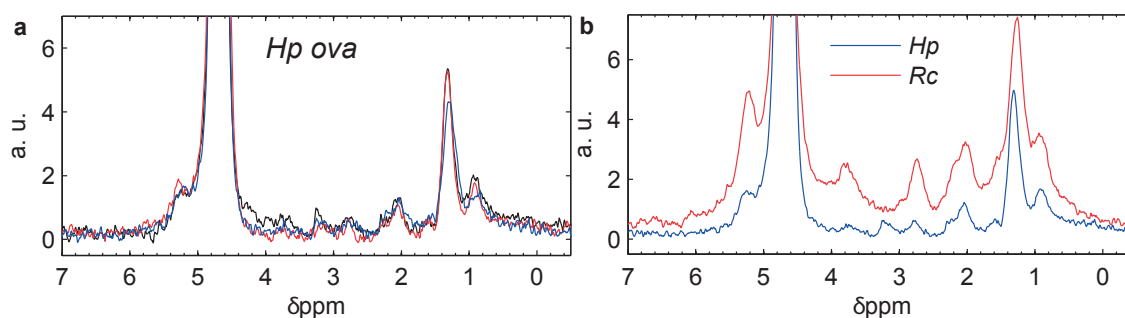


Figure 4.6: NMR spectra of single *Heligmosomoides polygyrus bakeri* (*Hp*) ova and averaged spectra of *Richtersius coronifer* (*Rc*) and *Hp*. (a) Three *Hp* single ovum experiments in D₂O-based gels. (b) Comparison between average spectra of five *Rc* ova (red) and three *Hp* ova (blue) in D₂O-based gels.

4.3.4 *Hp* ova spectroscopy

Figure 4.6a shows ¹H NMR spectra obtained from three different single *Hp* ova placed in D₂O-based gel, resulting from 36 hours of averaging and characterized by a linewidth of about 0.25 ppm. *Hp* ova, whose ellipsoidal shape was systematically oriented horizontally on the gel, were always entirely contained within the most sensitive region of the probe (see Fig. 4.1c and microcoil sensitivity maps below) allowing for a full exploitation of the microcoil high sensitivity. Contrarily to the case of *Rc* ova, in these measurements on *Hp* ova we do not observe a clear indication of heterogeneity despite the study is performed at comparable effective sensing capability. With a typical volume of about 0.1 nl the *Hp* ovum is, to date, the smallest intact biological sample in which intracellular compounds are detected with NMR spectroscopy. Figure 4.6b shows averaged NMR spectra obtained from experiments on *Rc* and

Hp ova in D₂O-based gels. These spectra indicate that, at our level of sensitivity, the averaged intracellular chemical compositions of *Rc* and *Hp* ova are similar, with only small eventual differences at 3.2 and 3.8 ppm between the two species.

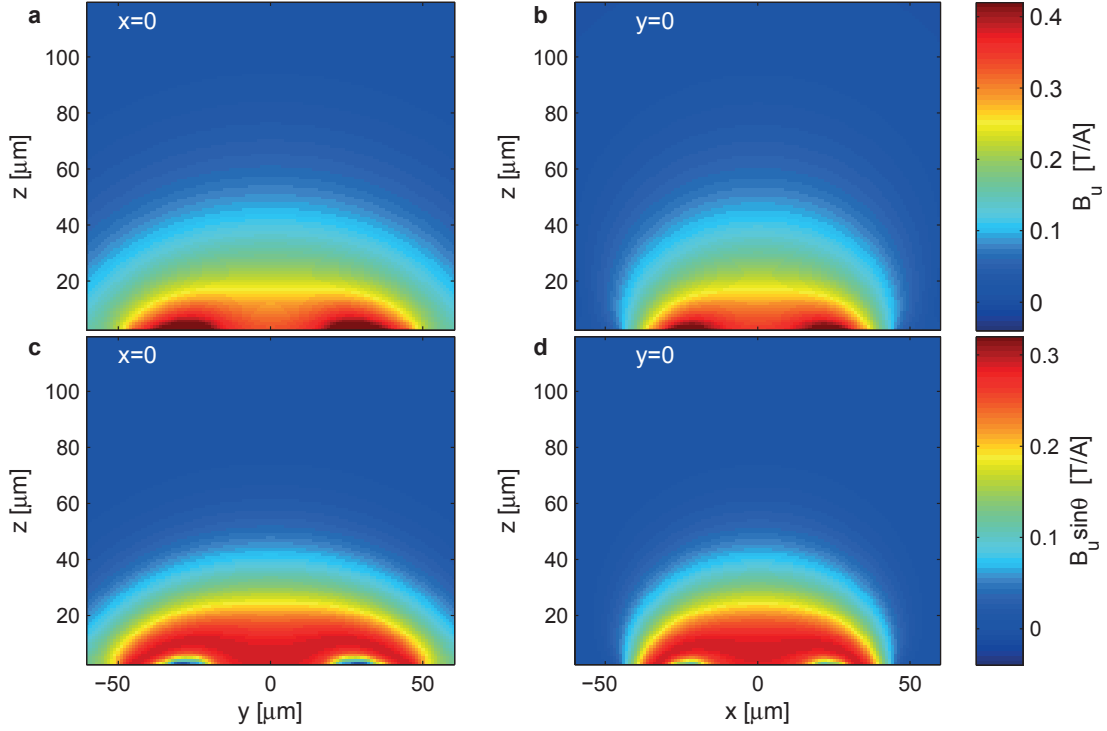


Figure 4.7: **Maps of effective unitary field and effective sensitivity of the integrated microcoil.** (a-b) Maps of the effective unitary field $B_u = (B_{u,z}^2 + B_{u,y}^2)^{1/2}$ at $x = 0$ cross-section (a) and $y = 0$ cross-section (b). (c-d) Maps of the effective coil sensitivity in conditions of maximum total signal ($\tau = 2.5 \mu\text{s}$) at $x = 0$ cross-section (c) and $y = 0$ cross-section (d).

4.3.5 Sensitivity (with maps) of the single-chip probe

In Fig. 4.7 we computed sensitivity maps and unitary field maps of the integrated microcoil. The static B_0 field is oriented along the \hat{x} axis. The octagonal loops of the microcoil are approximated with circular ones. The detailed description of the microcoil structure is available in Ref. [21]. The unitary field, defined as the field produced by a current of 1 A in the coil loops, is computed via the Biot-Savart law. The effective unitary field B_u is the component orthogonal to the static field. The effective coil sensitivity is computed taking into account the effect of the non-homogeneity of the nutation angle $\theta = \gamma B_1 \tau$. The resulting effective sensitivity is proportional to $B_u \sin\theta$. The pulse length that maximizes the signal ($\tau = 2.5 \mu\text{s}$), is measured experimentally and is matched by simulations that assume a current $i = 9 \text{ mA}$ through the coil in TX mode.

Due to the planar geometry of the excitation/detection coil, our probe has an effective spin

Chapter 4. NMR spectroscopy of single sub-nL ova with ultra-compact single-chip probes

sensitivity which depends on the sample volume, shape, and distance from the coil surface. Our experimental conditions are characterized by a spectral resolution of about 0.3 ppm and a field strength of 7 T. In the case of a spherical sample of 30 μm diameter in contact with the chip surface, the time-domain spin sensitivity of about 1.5×10^{13} spins/Hz^{1/2} corresponds to a limit of detection (LOD) in the frequency domain of about 700 pmol of ¹H nuclei per single scan (quantity of ¹H nuclei that gives a signal-to-noise ratio of three). In this example the sensing capability of the microcoil is fully exploited as the sample is contained within the most sensitive region of the detector (see maps above). In the case of a spherical sample of 100 μm diameter in contact with the chip surface, the spin sensitivity is reduced to about 4×10^{13} spins/Hz^{1/2}, corresponding to an LOD in the frequency domain of about 1900 pmol of ¹H nuclei per single scan (the spins intended to be distributed homogeneously within the whole sample). In terms of LOD, the performance of our single-chip probe are competitive with the most sensitive inductive NMR devices so far reported [145–148].

4.3.6 Chemical shifts in *Rc* and *Hp* ova.

In this study the relatively small number of samples available (see Methods) poses significant and non-trivial technical challenges to studies of ova collections aimed at the elucidation of proton peaks assignment (see Discussion). In our experiments the peak assignment is hindered by the combination of a small number of spins with a relatively poor spectral resolution. Nevertheless, a few qualitative observations can be done by comparison to previously reported NMR spectra of intact *C. elegans* worms [149] and *Xenopus laevis* ova [135, 139]. Although these NMR-based studies analyze biological entities that are different from the ones investigated in this work, they probably represent the closest term of comparison available in literature in terms of volume size and samples nature. The NMR signals in *Xenopus laevis* [135, 139] at about 0.9, 1.3, 2.1, 2.8, 5.2 ppm were attributed to highly concentrated yolk lipids (in particular triglycerides [135, 150]). These results well explain the origin of the dominant features in both *Rc* and *Hp* ova spectra. In Figs. 4.6a and 4.6b, a peak at about 3.2 ppm seems to discriminate the intracellular content of *Hp* ova from the one of *Rc* ova. Prominent resonances at about 3.2 ppm were previously assigned to a relatively restricted group of metabolites in intact *C. elegans* worms, which are nematodes as *Hp* [149].

As shown in Fig. 4.2 a visible signal at 3.8 ppm is present in some *Rc* ova. A resonance at about 4 ppm was assigned to the glycerol backbone in *Xenopus laevis*, typically lower and broader with respect to the other lipid signals (to which this compound is strictly related) [135]. Hence, this resonance is hardly related to yolk lipids. The presence of a highly concentrated endogenous compound is a more likely explanation for the signal detected at this particular chemical shift.

4.4 Discussion

In this study we reported on the use of a state of art sub-nL NMR probe for the analysis of single sub-nL ova of microorganisms, indicating the limits of the technique for the non-invasive detection of intracellular compounds within ova as small as 0.1 nL. The results shown may be used as a starting point to extrapolate the realistic experimental possibilities offered by NMR tools for applications such as the non-invasive selection of microscopic entities based on the direct quantification of highly concentrated endogenous compounds. In terms of spin sensitivity performance that future setups may offer, a straightforward improvement is the use of a higher field. Moving from 7 T to 23.5 T (the highest field commercially available) with the same microcoil should improve the spin sensitivity by a factor of six if the linewidth originates entirely from magnetic susceptibility issues (see Appendix C). In these conditions it is reasonable to achieve limits of detection on ^1H nuclei in the order of 7 pmol in 10 minutes and 0.9 pmol in 10 hours for samples having a volume below 100 pL and linewidths as large as 0.3 ppm. Further improvements are obvious for samples exhibiting typical linewidths narrower than the ones observed in this study.

Improved spectral resolutions may be obtained by MAS techniques [135, 141, 151]. A few explorations on microscopic intact biological samples report linewidths of about 0.1 ppm in *Xenopus laevis* eggs at 14 T [135] and *C. elegans* at 23.5 T [141]. Experiments on large collections of *C. elegans* and bovine tissues demonstrate linewidths as narrow as 0.05 ppm [141, 151]. It seems therefore reasonable to obtain significant narrowing of the line via MAS. Although MAS probes are not yet optimized for maximum sensitivity at the sub-nL scale, its application at larger volume scales (few tens of nL) may already provide tools supporting the study of sub-nL ova. In wider terms, static and/or spinning probes analyzing 10 nL collections of rare or precious sub-nL ova would allow for proton assignments (elucidating eventual heterogeneities detected among individual samples at the single ovum level) and a better characterization of the spin-spin relaxation properties without need of excessive sample accumulation. However, the realization of such tools is hindered by significant technical challenges, simultaneously requiring small sensitive volumes, high filling factors, high resolution, MAS, and sample loading and manipulation capabilities.

The results shown above, obtained at a relatively weak field of 7 T, suggest that a LOD of about 5 pmol of ^1H nuclei within a sub-nL region (in this study specifically corresponding to sensitivities ranging from 20 to 50 mM in terms of intracellular concentration) is sufficient for the detection of the most concentrated compounds in individual ova of microorganisms having volumes below 1 nL. Curiously, signals at chemical shifts that are not typical of yolk lipids are visible. This indication seems, at first sight, in contradiction with the previous NMR spectroscopic studies of intact *Xenopus laevis* ova [135], where yolk lipids explain all the spectroscopic features, which are essentially identical to those of the yolk of an hen egg [152]. In order to detect metabolites in these samples it was indeed necessary the use of magic angle spinning probes at 14 T loaded with more than one ovum [135]. However, the *Xenopus laevis* ovum (the smallest previously analyzed with NMR spectroscopy) might not be the best term of comparison, as its typical volume (about 1 μL) is larger by a factor ranging from 10^3 to 10^4

Chapter 4. NMR spectroscopy of single sub-nL ova with ultra-compact single-chip probes

with respect to the ova studied in this work.

A peculiar class of sub-nL ova that justifies the interest in approaches for the non-invasive intracellular spectroscopy of individual samples is constituted by the mammalian zygotes. Recent studies demonstrate, using techniques other than NMR, that in sheep [153] and human [154] oocytes the uptake or production rates of metabolites such as lactate, pyruvate, and glucose can reach 100 pmol/oocyte/h and change radically along the natural development. It is worth noting that these results concern exchange rates measured in the extracellular medium and, hence, do not provide a direct quantification of the intracellular content and its time evolution. Spectrophotometry of intracellular extracts, on the other hand, has shown that up to 30 pmol/oocyte of glutathione (GSH) are contained in oocytes of goat [155] and pig [156, 157] and can change in reaction to environment and developmental stage [158]. Variations of a few pmol/oocyte of GSH in time scales of the order of several hours have been reported in hamster [159] and rat [160] oocytes. In these studies, the intracellular GSH content and its evolution is directly measured, but the ensemble measurements hide possible heterogeneities among single entities. These findings indicate that the sensitivity achievable with high sensitivity miniaturized inductive NMR probes should be sufficient for a non-invasive real-time intracellular monitoring of GSH in single mammalian zygotes. The application of NMR spectroscopy to the analysis of spent culture media was recently proposed to aid the selection of viable human embryos for in vitro fertilization purposes [161]. The direct application of NMR on single embryos using miniaturized high sensitivity probes is potentially advantageous for this aim. We suggest that systematic and extensive NMR studies on single cultured ova may provide new data that could shed light on cryptic processes involved in embryonic development [153–160] and provide new methodologies to estimate embryonic health [158, 161].

The hardware used in this work is an ultra-compact integrated probe entirely realized with commercially accessible complementary-metal-oxide-semiconductor (CMOS) technologies that might open to the realistic possibility of implementing relatively low-cost arrayed miniaturized probes. However, improvements for what concern samples manipulation are required, especially for applications aiming at studying precious samples such as mammalian embryos. Recently, many efforts were successfully dedicated to the microfabrication of devices for manipulation and culture of individual living embryos [162, 163]. Both integrated circuits and microfluidics are suitable for arrays implementation, and their combination has been demonstrated in applications such as single cell magnetic manipulation [164] and flow cytometry [165]. We believe that this combination can be extended to NMR applications for the realization of arrayed high sensitivity NMR probes, enabling simultaneous studies on a large number of single biological entities in the same magnet.

4.5 Methods

4.5.1 Single ovum probe mounting.

Figure 4.8 shows a schematic representation of the probe mounting procedure. The ova were first transferred, using a 100 μL pipette, from the tube into a Petri dish filled by 1.5% H_2O -based agarose gel. Often more than one ovum was found on the Petri dish, in which case the additional samples were left isolated on the gel for eventual later use and stored at 4°C between successive experiments. Single ova were transferred into a 1.5% agarose gel-filled polystyrene cup using two eyelashes. No visible damage to the ova was provoked during this procedure. The concentration of agarose was carefully chosen, based on repeated assemblies of ova, such that the resulting gel was hard enough to allow a stable placement of the ovum but still sufficiently soft to avoid ovum rupture during the setup assembly (typically happening for gels with more than 3% of agarose). The gel matrix was providing a deformable soft surface to embed and hold the ovum. When placed on the gel, the ovum was protruding from the surface by about half of its volume, hence ensuring an initial physical contact between the ovum and the surface of the microcoil upon placing. Later, the cylindrical polystyrene cup, containing the gel with the ovum on its surface, was positioned on top of the microchip in such a way that the ovum was precisely aligned over the microcoil. The local depletion of any visible air bubble was relatively easy and reproducible. The cup was fixed to the printed circuit board with candle wax. The gel keeps the sample in close contact with the coil for days without physically damaging it, whereas the wax prevents gel drying. The microchip was wire bonded to a printed circuit board, with bonding wires electrically isolated by a silicone glue. Figure 4.1e describes the assembled probe.

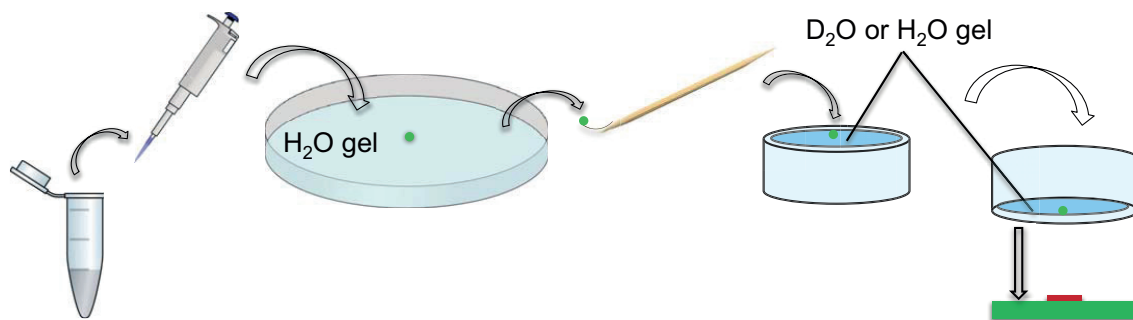


Figure 4.8: **Schematic representation of the probe mounting procedure.**

4.5.2 Tardigrade *Richtersius coronifer* (*Rc*).

Eggs of *Rc* were extracted from a moss sample collected in Öland (Sweden) by washing the substrate, previously submerged in water for 30 min, on sieves under tap water and then individually picking up eggs with a glass pipette under a dissecting microscope. The eggs were shipped within 24 hours in sealed tubes with water and subsequently stored at -20°C before use. The embryonic development of *Rc* ova is relatively slow, with the eggs hatching in

Chapter 4. NMR spectroscopy of single sub-nL ova with ultra-compact single-chip probes

more than 50 days [166]. All experiments were carried out within a week after tube opening. The tube was stored at 4 °C between separated experiments. The NMR experiments were performed in H₂O, M9, and D₂O. It is known that prolonged exposure to a high concentration of D₂O affects living organisms to different extents, from lethal to marginal [167, 168]. In order to test the effects of D₂O exposure on *Rc* specimens, 16 eggs and 10 animals were submerged in D₂O (at 15 °C) for 36 and 24 hours respectively and then transferred in H₂O. A control group of 16 eggs was kept in H₂O. The effects of the exposition to D₂O on the survival of the specimens were not negligible but definitively not systematically lethal: all the animals survived, and a hatching of 84% in the control group and of 63% in those exposed to D₂O was observed after a time of approximately 2 months. The total amount of *Rc* ova available for this study was of about 120 units.

4.5.3 Nematode *Heligmosomoides polygyrus bakeri* (*Hp*).

Eggs of *Hp* were collected from faeces of infected mice. Faeces were first dissolved in water and then washed with a saturated NaCl solution. Floating eggs were collected from the top layer of the solution and washed twice. Final centrifugation in water for 5 minutes at 2000 rpm sedimented clean eggs at the bottom of the tube. The amount of ova typically available at each extraction varied from tens to a few hundred depending on the host organism response to the infection. Fecundated ova of *Hp* develop into a fully embryonated state within 24 hours and within two days stage 1 larvae begin to emerge [169]. In H₂O-based gels *Hp* ova regularly hatched after a few hours, the emerging larvae migrating far from the sensitive region of the microcoil. In D₂O-based gels the ova never hatched within two days of observation, hence allowing for the necessary long averaging time. All experiments were carried out within two days after sample extraction. The tube was stored at 4 °C between separated experiments.

4.5.4 NMR experimental details.

NMR experiments were performed in the 54 mm room temperature bore of a Bruker 7.05 T (300 MHz) superconducting magnet. The electronic setup was identical to the one described in details in Ref. [21]. All experiments employing the single-chip probe were performed with a repetition time of 2 s, a $\pi/2$ pulse length of 2.5 μ s, and an acquisition time of 400 ms. The time domain data were post-processed by applying an exponential filter with decay of 50 ms. The alphabetic order in Fig. 4.2b corresponds to the chronological order of the measurements. Chemicals. H₂O (Sigma Aldrich, 270733). D₂O (Acros Organics, 166301000). Agarose (BioConcept, Standard Agarose LE-7-01P02-R). Silicone glue (Momentive, RTV118). Polystyrene cup (Semadeni, 10 mm diameter, 5 mm height). The M9 buffer is prepared as in Ref. [170].

5 Appendix: supplementary, designs

Appendix A: Derivation of equation (1.12)

In this appendix we explicitly derive equation (1.12), which expresses the noise fluctuations in the frequency domain for a finite acquisition time. The integral to be solved is:

$$\bar{n}_f = \left\{ \frac{1}{F} \int_0^T n^2(t) e^{-\frac{2t}{T_m}} dt \right\}^{1/2} \quad (5.1)$$

We can focus on the integral I:

$$I = \frac{1}{F} \int_0^T n^2(t) e^{-\frac{2t}{T_m}} dt \quad (5.2)$$

From eq. (1.11) we know that:

$$TFn_{sd}^2 = \int_0^T n^2(t) dt \quad (5.3)$$

Integrating (5.2) by parts and defining $f' = n^2(t)$ one has $f(t) = tFn_{sd}^2$ from eq. (5.3). Develop-

ing (5.2) we obtain:

$$\begin{aligned}
 I &= \left[t n_{sd}^2 e^{-\frac{2t}{T_m}} \right]_0^T + \frac{2}{T_m} \int_0^T t n_{sd}^2 e^{-\frac{2t}{T_m}} dt \\
 &= T n_{sd}^2 e^{-\frac{2T}{T_m}} + \frac{2 n_{sd}^2}{T_m} \int_0^T t e^{-\frac{2t}{T_m}} dt \\
 &= T n_{sd}^2 e^{-\frac{2T}{T_m}} + \frac{2 n_{sd}^2}{T_m} \left\{ \left[t \left(-\frac{T_m}{2} e^{-\frac{2t}{T_m}} \right) \right]_0^T + \frac{T_m}{2} \int_0^T e^{-\frac{2t}{T_m}} dt \right\} \\
 &= T n_{sd}^2 e^{-\frac{2T}{T_m}} + \frac{2 n_{sd}^2}{T_m} \left(-T \frac{T_m}{2} e^{-\frac{2T}{T_m}} \right) - \frac{T_m n_{sd}^2}{2} \left[e^{-\frac{2t}{T_m}} \right]_0^T \\
 &= \frac{T_m n_{sd}^2}{2} \left(1 - e^{-\frac{2T}{T_m}} \right)
 \end{aligned} \tag{5.4}$$

From eq. (5.1) and (5.2) we have $\sqrt{I} = \bar{n}_f$, which gives (in accordance to (1.12)):

$$\bar{n}_f = n_{sd} \sqrt{\frac{T_m}{2} \left(1 - e^{-\frac{2T}{T_m}} \right)} \tag{5.5}$$

Appendix B: IC schematics

In this section we report the block diagram and the detailed transistor level schematics of the successful designs made during my PhD thesis. Overall, the whole work can be resumed in two different designs for what concerns the active electronics. Both the designs have been previously presented in Chapter 2 and 3. First, we describe in details the TX/RX which has been realized first, which does not have IQ demodulation capabilities. This transceiver was used to implement the ultra-compact single-chip probe used for the measurements shown in Chapter 4.

Single-channel broadband transceiver

Figure 5.1 shows a photograph of the single-chip transceiver together with its block diagram schematics. This design is for interface with external excitation/detection probe heads as shown in Chapter 2.

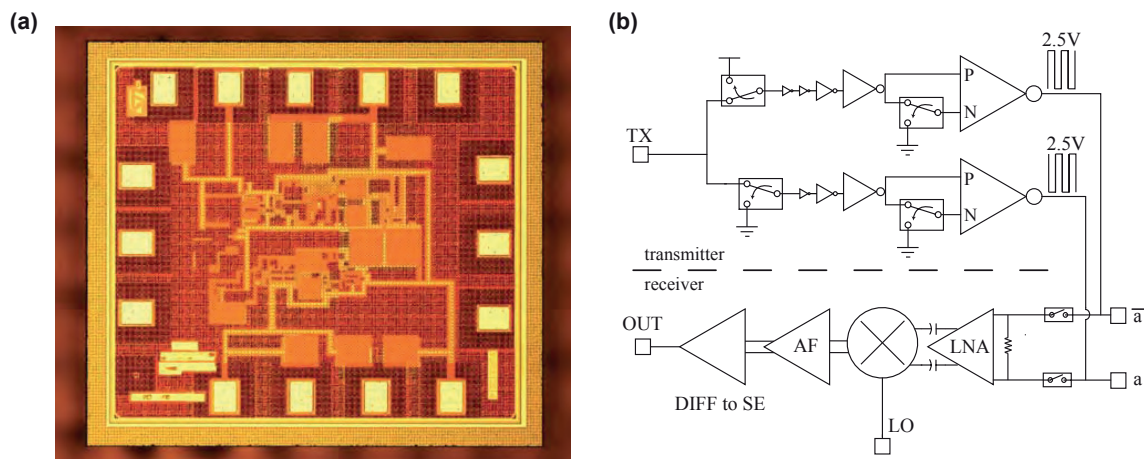


Figure 5.1: **Single-channel transceiver, 2014.** (a) Photograph of the first broadband CMOS transceiver realized at LMIS1. This version of the transceiver is for use with external excitation/detection probe heads. (b) Block diagram schematics of the active electronics. Nodes a and \bar{a} indicate where the excitation/detection head is connected. The block diagram shows TX mode, where squared waves of 2.5 V amplitude are sent to the probe head.

The main transistor level design challenge is to trade-off between the wide bandwidth (1-300 MHz) and the low input referred noise (about $1 \text{ nV/Hz}^{1/2}$). In integrated circuits high frequency operation (i.e. in the GHz range) is achieved by using small area transistor sizes. Small devices have smaller parasitic capacitance and hence better speed performance allowing for operation at high frequency. On the other hand they have larger flicker noise with corner frequency in the MHz range limiting their functionality for low frequency operation with satisfactory noise performance. In Fig. 5.2 it is shown the transistor level schematics of the low noise amplifier. The bias voltages V_{B1} , V_{B2} , and V_{B3} are set by system of current mirrors, together

with the currents flowing through the amplification stage and the common mode feedback. V_{DD} indicates the DC power source which corresponds to 1.5 V.

The device amplifies the small NMR signal in order to make the noise contribution of the following down-conversion device (mainly the frequency mixer) negligible. For the external coil case the minimum input noise is about $1.8 \text{ nV/Hz}^{1/2}$, set by the 160Ω equivalent input impedance in matched conditions. Since the noise of a frequency mixer is in the order of few tens of $\text{nV/Hz}^{1/2}$, the 39 dB gain of the LNA is enough to not deteriorate the SNR in the following circuitry. The chosen scheme is a current reuse differential transconductance, loaded with a pseudo-cascode. The voltage gain, input referred noise and main frequency pole can be expressed, in first approximation, by the following equations:

$$\begin{aligned}
 A &= (gm_p + gm_n)R_L \\
 f_{p1} &= \frac{1}{2\pi R_L C_L} \\
 f_{p2} &= \frac{gds_p + gds_n}{2\pi C_i} \\
 v_n^2 &= \frac{4k_B T \xi}{gm_p + gm_n} + \frac{K_{fn}}{f(WL)_n} + \frac{K_{fp}}{f(WL)_p} + \frac{4k_B T \xi gm_m}{(gm_p + gm_n)^2} + \frac{K_f gm_m^2}{f(WL)_m (gm_p + gm_n)^2} + \frac{4k_B T R_L}{A^2}
 \end{aligned} \tag{5.6}$$

where gm_p , gm_n , gds_p and gds_n are the gate-drain and drain-source transconductances of the input devices (M_{n1} , M_{n2} , M_{p1} , M_{p2}), R_L is the output resistance, ξ is a technological constant approximately equal to 0.6, gm_m is the transconductance of the current mirror devices (M_{p3} , M_{p4} , M_{p5} , M_{p6}), K_{fn} and K_{fp} are the flicker noise constants of n and p devices, C_L and C_i are the sum of the capacitances connected to the output and input nodes including the MOS parasitics. Equation (5.6) points out that, maximizing the input transconductance and designing the current mirror devices in strong inversion (i.e. with small aspect ratio, small g_m), it is possible to reduce the noise due to transistors other than the input transistor. Furthermore, noises of cascode devices and load resistances are made negligible thanks to parameter optimization and to the voltage gain division of the first stage. We followed as design strategy: (1) to trade-off between noise and speed a g_m/I ratio of 10 was chosen as a starting point for the input devices; (2) the minimum input transistor area is set by the noise performances at low frequency (flicker noise); (3) the minimum transconductance is set by the thermal noise floor (i.e. for frequencies typically above 20 MHz). To maximize the transconductances per unit area, the devices are designed with short lengths and large widths. The supply current is then used to tune the transconductance in order to achieve the wanted noise. After designing the input transconductance, the resistive load is decided in function of the desired gain. Since the structure is fully differential, a feedback is added to ensure the stability of the output common mode voltage. This is done by mean of transistors (M_{n5} , M_{n6} , M_{p7} , M_{p8}) which set the output DC voltage at a level which is about 1 V.

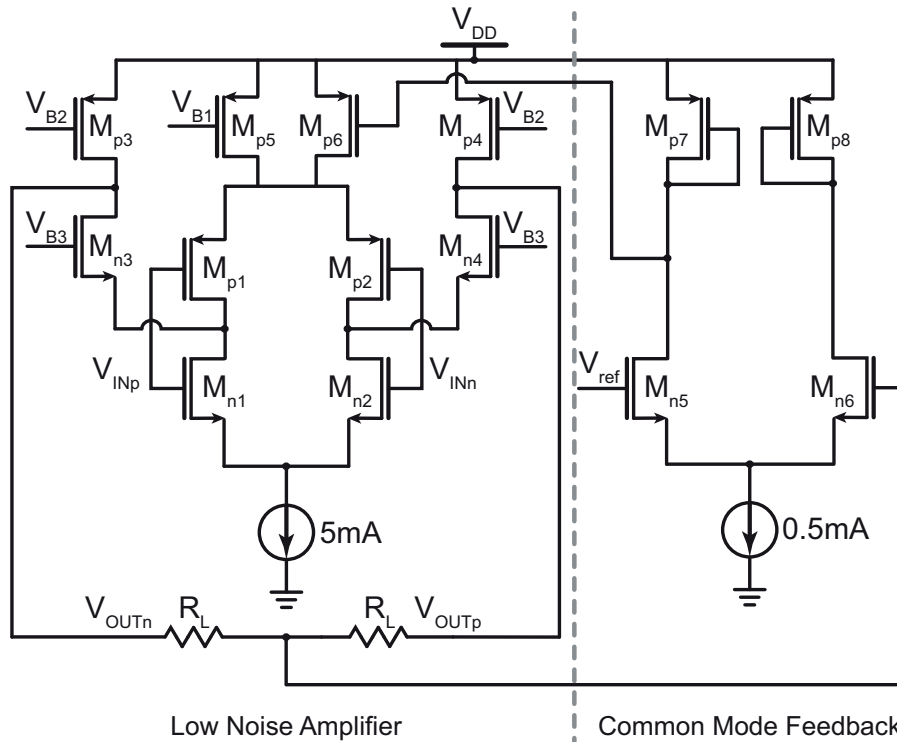


Figure 5.2: **LNA**. Transistor level schematics of the low noise amplifier. Physical dimensions in Table 5.1.

Fig. 5.3 shows the transistor level schematics of the double balance Gilbert cell. This active mixer is chosen among others for its simplicity and for noise performances, which are better if compared with the passive counterpart. Transistors M_{n1} and M_{n2} together with R_{s1} and R_{s2} act as transconductance, converting the voltage signal coming from the LNA into a current. Transistors M_{n3-6} , driven by the local oscillator, multiply the current signal by a square wave. The resulting signal is composed by sinusoids with frequency equal to the sum and difference of the one driving the mixer. The sum component is filtered out by the load filter, leaving a sinusoid oscillating at the difference in frequency between the signal and the local oscillator. Again, the minimum size of the input devices is chosen to keep the input referred noise in a reasonable range (10 nV) and the transistor M_{n3-6} are sized to behave as hard switches when driven by a 1.5 V peak-to-peak square wave at 1 GHz. With this assumption the voltage gain can be written as $A = \frac{4R_L}{\pi R_s}$. At the output a low pass filter with frequency equal to $f_p = \frac{1}{2\pi R_f C_F}$ is added to filter out the sum component. In figure 5.4 the audio-frequency amplifier following the mixer is detailed. The design rules considered to size the transistors are similar to the ones described for the LNA. A resistive feedback is added to control the voltage gain and bandwidth.

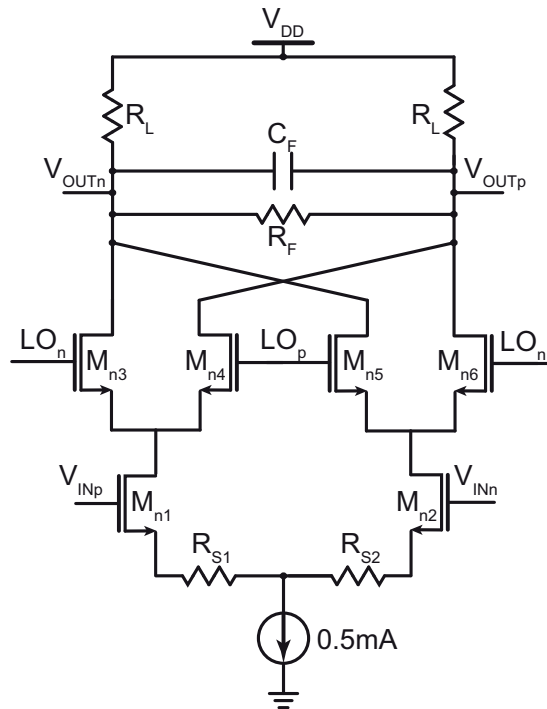


Figure 5.3: **Mixer**. Transistor level schematics of the Gilbert mixer. Physical dimensions in Table 5.1.

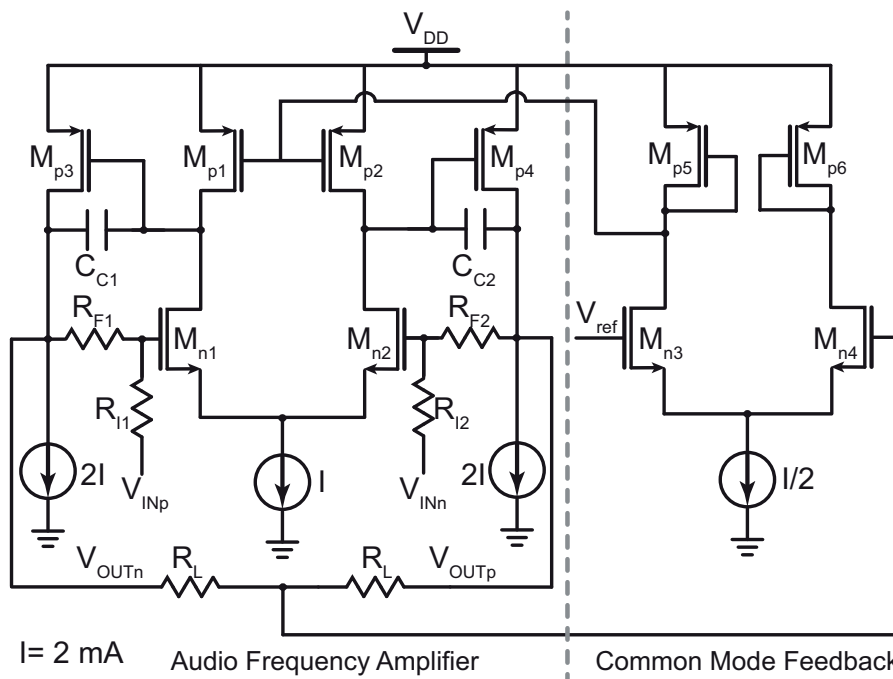


Figure 5.4: **AF Amplifier**. Transistor level schematics of the AF amplifier. Physical dimensions in Table 5.1.

The transistor level schematics of the transmitter is fully described by Fig. 5.1. Essentially, the transmitter is constituted by two chains of inverters that operate in a differential way. In order to reduce the time delay of the differential paths one dummy inverter is inserted along the chain which contains the lower number of inverters. The power amplification of this design is not big. For this reason, the transmitter is preceded by an amplifying stage constituted by a self-biased inverter topology. In this work we could obtain transmitters operating with input power as low as -3 dBm and delivering about 10 dBm (depending on the output impedance). For reasons of noise contamination and transmitted power the DC power source of the transmitter is physically separated by the one of the receiver electronics and it has a value of 2.5 V. One element of novelty of this work with respect to the previously reported transceiver architectures is the fully integrated system of switches that allow to interface the chip to excitation/detection probe heads via two nodes only. In Fig. 5.5 we show the detailed schematics of such switches, which affect both the topology of the transmitter and the input stage of the receiver. The schematic shows how the interface between transmitter and receiver is realized for one of the two differential inverters chains. In the case shown, the total number of inverters is even and a few straightforward adjustments have to be done to construct the other differential pair (whose number of inverters is odd). When the control signal is $s=2.5$ V ($\bar{s}=0$) we are selecting the RX mode and the inverter chain is in stand-by (no power is drawn from the source). In the opposite configuration the inverters are transmitting power to the probe and the switches on the receiver side protect the LNA.

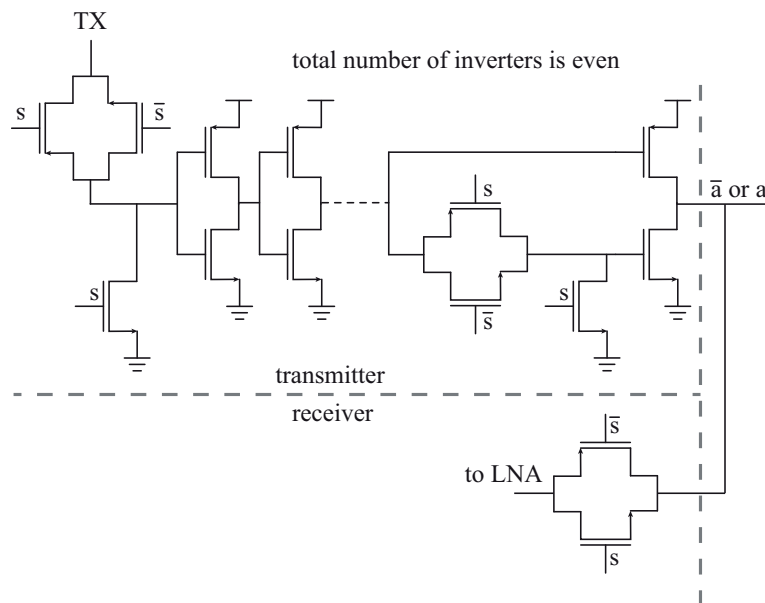


Figure 5.5: **Switches.** Transistor level schematics of the fully integrated transmit-receive switches.

Dimensions in figs. 5.4, 5.3, 5.2

LNA		
Object name	Width (μm)	Length (μm)
M_{n1}, M_{n2}	350	0.18
M_{n3}, M_{n4}	70	0.13
M_{n5}, M_{n6}	40	0.13
M_{p1}, M_{p2}	840	0.18
M_{p3}, M_{p4}	150	0.2
M_{p5}	450	0.25
M_{p6}	290	0.25
M_{p7}, M_{p8}	45	0.25

MIXER		
Object name	Width (μm)	Length (μm)
M_{n1}, M_{n2}	15	0.4
$M_{n3}, M_{n4}, M_{n5}, M_{n6}$	50	0.13
R_{S1}, R_{S2}	300Ω	
R_L	$2 \text{ k}\Omega$	
R_F	$100 \text{ k}\Omega$	
C_F	20 pF	

AF Amplifier		
Object name	Width (μm)	Length (μm)
M_{n1}, M_{n2}	100	3
M_{n3}, M_{n4}	30	0.3
M_{p1}, M_{p2}	70	4
M_{p3}, M_{p4}	60	0.5
M_{p5}, M_{p6}	35	4
R_{I1}, R_{I2}	$6 \text{ k}\Omega$	
R_{F1}, R_{F2}	$18 \text{ k}\Omega$	
R_L	$10 \text{ k}\Omega$	
R_{Z1}, R_{Z2}	400Ω	
C_{C1}, C_{C2}	3 pF	

Table 5.1: Physical dimensions of transistors used in LNA, Mixer, AF Amplifier.

Chips bonding and use

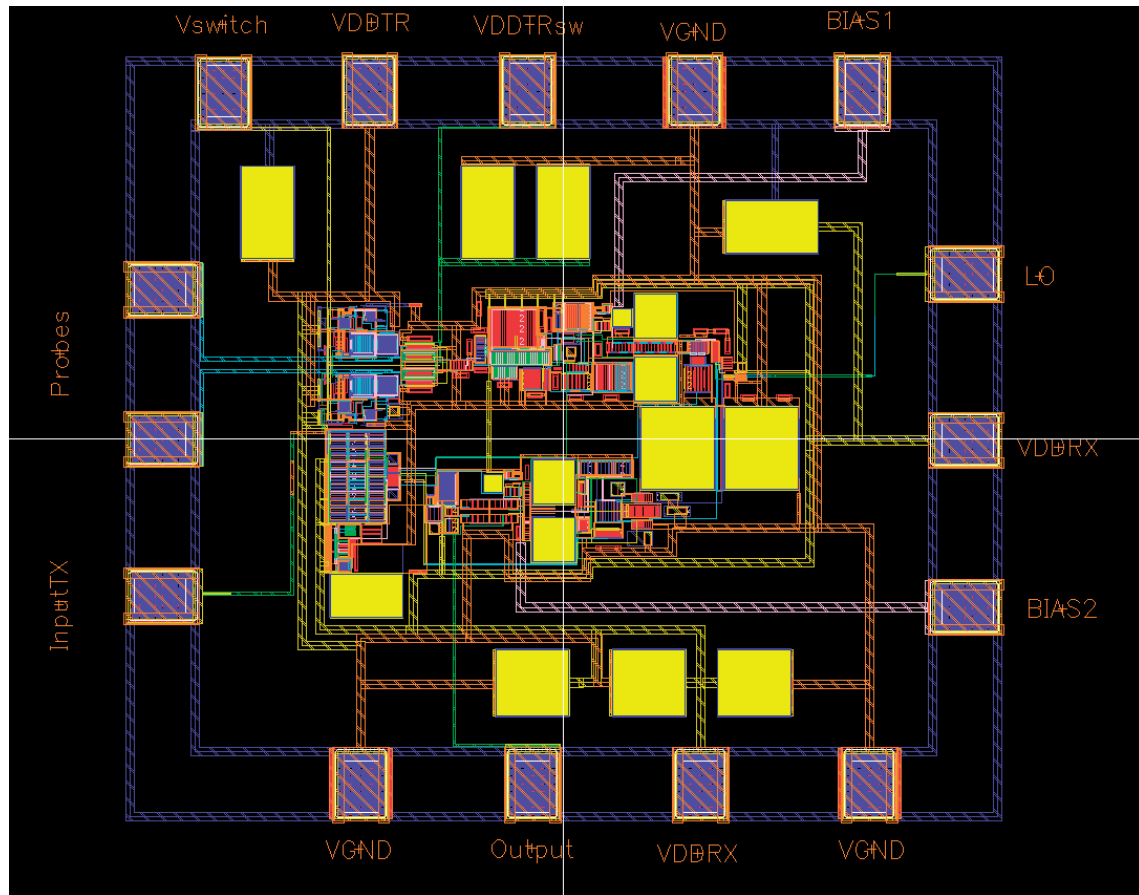


Figure 5.6: **Single-channel transceiver, 2014.** Virtuoso Layout view of the designed single-channel transceiver. This version of the chip interfaces to external excitation/detection resonators.

Figure 5.6 shows the Cadence Virtuoso view of the final layout of the single-channel transceiver designed to interface with external excitation/detection probe heads. Here we want to describe the role of each pin to enable future use of this design.

Probes The two nodes indicated as probes correspond to the nodes a and \bar{a} (see figure 5.1 and chapter 2). Any PCB routing should consider that the nodes are differential.

InputTX This node is the RF input of the transmitter. The RF source needs to be AC coupled, and the input node has to be DC biased at about 1.25 V. To do so we typically connect this node to an inductance of about 60 nH that picks a voltage of 1.25 V. In the designed PCBs the 1.25 V is generated dividing by two the 2.5 V power source (see below) via two resistors. The InputTX node has a 1.2 k Ω resistance to ground. Thus, we typically use a

Chapter 5. Appendix: supplementary, designs

resistance to 2.5 V of 1.2 k Ω and a resistance of 120 k Ω to ground in order to obtain the needed 1.25 V. RF power should be around 3 dBm.

Vswitch This node manages the transceiver TX to RX switching. When equal to 2.5 V the transceiver is in RX mode. When equal to ground the transceiver is in TX mode. To interface Vswitch to an external standard TTL signal we typically use an inverter fed by 2.5 V before the pin.

VDDTR and VDDTRsw These two nodes were separated for testing, but they should be connected on the PCB routing. Here we feed the switches and transmitter with a 2.5 V power source.

VGND All pins with this name are connected to ground.

BIAS1 and BIAS2 The two nodes connect to bias points within the receiver and can be used for testing only. They can be connected to floating pads on the PCB and can be used to check the presence of 1 V on each. They can be left floating too if testing is not needed.

LO This node is the RF input of the local oscillator. The RF source needs to be AC coupled, and the input node has to be DC biased at about 0.75 V. To do so we typically connect this node to an inductance of about 60 nH that picks a voltage of 0.75 V. In the designed PCBs the 0.75 V is generated dividing by two the 1.5 V power source (see below) via two resistors. The InputTX node has a 1.2 k Ω resistance to ground. Thus, we typically use a resistance to 1.5 V of 1.2 k Ω and a resistance of 120 k Ω to ground in order to obtain the needed 0.75 V. RF power should be around 0 dBm.

VDDRX Here we feed the whole receiver with a 1.5 V power source.

Output The output pin of the receiver gives a single-ended signal. The DC value has to be about 1 V. The maximum output is about 300-400 mV. We typically interface this pin to an AC coupled AF amplifier. The output is proved to directly drive coaxial cables as long as 2-3 meters.

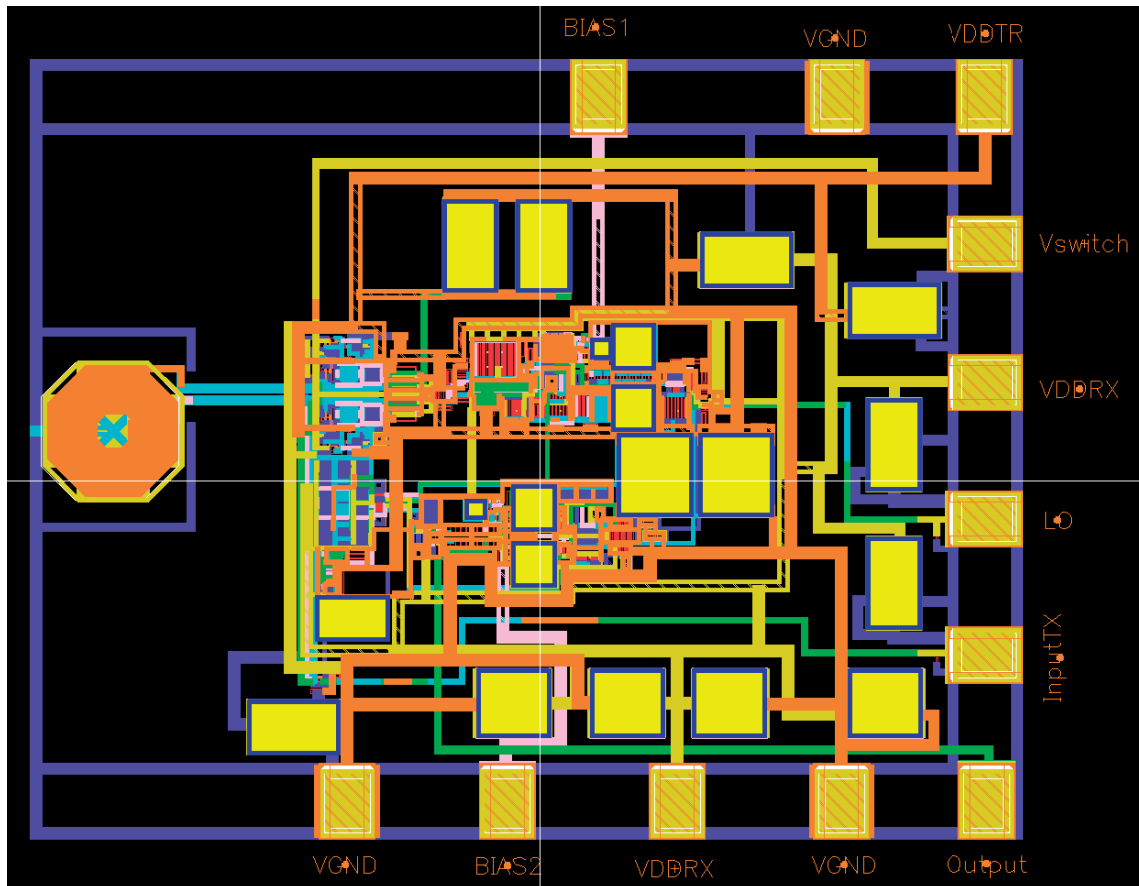


Figure 5.7: **Ultra-compact single-chip probe, 2014.** Virtuoso Layout view of the designed ultra-compact single-chip sub-nL probe.

Figure 5.7 shows the Cadence Virtuoso view of the final layout of the ultra-compact single-chip probe described in chapter 2 and 4. Here we want to describe the role of each pin to enable future use of this design. The TX/RX architecture is practically identical to the one shown above. All the sub-nL ultra-compact probes have this same pin layout. Note that this layout is designed to work with only 8 pins wire bonded (the 8 on the right-end side of the chip). When bonded this way there is maximum space around the microcoil to ease the use of the probe.

InputTX This node is the RF input of the transmitter. The RF source needs to be AC coupled, and the input node has to be DC biased at about 1.25 V. To do so we typically connect this node to an inductance of about 60 nH that picks a voltage of 1.25 V. In the designed PCBs the 1.25 V is generated dividing by two the 2.5 V power source (see below) via two resistors. The InputTX node has a 1.2 k Ω resistance to ground. Thus, we typically use a resistance to 2.5 V of 1.2 k Ω and a resistance of 120 k Ω to ground in order to obtain the needed 1.25 V. RF power should be around 3 dBm.

Vswitch This node manages the transceiver TX to RX switching. When equal to 2.5 V the transceiver is in RX mode. When equal to ground the transceiver is in TX mode. To interface Vswitch to an external standard TTL signal we typically use an inverter fed by 2.5 V before the pin.

VDDTR Here we feed the switches and transmitter with a 2.5 V power source.

VGND All pins with this name are connected to ground. Some can be left floating in order to enable an easier use of the chip by leaving more space around the microcoil.

BIAS1 and BIAS2 The two nodes connect to bias points within the receiver and can be used for testing only. They can be connected to floating pads on the PCB and can be used to check the presence of 1 V on each. They can be left floating too if testing is not needed in order to enable an easier use of the chip by leaving more space around the microcoil.

LO This node is the RF input of the local oscillator. The RF source needs to be AC coupled, and the input node has to be DC biased at about 0.75 V. To do so we typically connect this node to an inductance of about 60 nH that picks a voltage of 0.75 V. In the designed PCBs the 0.75 V is generated dividing by two the 1.5 V power source (see below) via two resistors. The InputTX node has a 1.2 k Ω resistance to ground. Thus, we typically use a resistance to 1.5 V of 1.2 k Ω and a resistance of 120 k Ω to ground in order to obtain the needed 0.75 V. RF power should be around 0 dBm.

VDDRX Here we feed the whole receiver with a 1.5 V power source.

Output The output pin of the receiver gives a single-ended signal. The DC value has to be about 1 V. We typically interface this pin to an AC coupled AF amplifier with a gain of 1000. The output is proved to directly drive coaxial cables as long as 2-3 meters.

IQ broadband transceiver

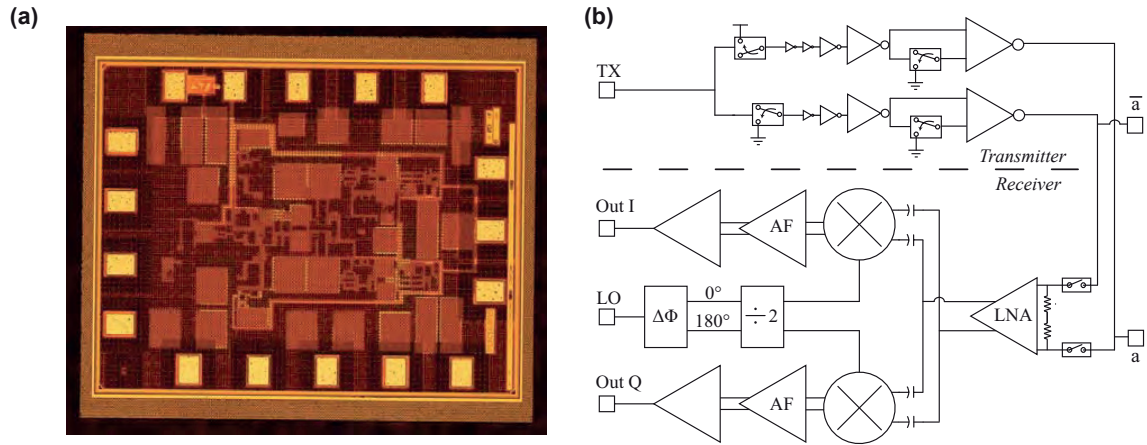


Figure 5.8: **IQ transceiver, 2015.** (a) Photograph of the IQ broadband CMOS transceiver realized at LMIS1. This version of the transceiver is for use with external excitation/detection probe heads. (b) Block diagram schematics of the active electronics. Nodes a and \bar{a} indicate where the excitation/detection head is connected. Transmitter, LNA, Mixers, AF Amplifier have been recycled from the design presented above.

Figure 5.8 shows a photograph of the single-chip transceiver together with its block diagram schematics. This design is for interface with external excitation/detection probe heads as shown in Chapter 3. The transmitter, LNA, Mixers, AF amplifier are identical to the ones implemented in the design shown in Fig. 5.1. The main difference between the IQ transceiver and the single-channel one is the capability of performing the detection in quadrature. Quadrature detection requires to demodulate the signal with two mixers fed by RF having a phase shift of 90° . In this design we had to implement such a phase shift starting from a single RF signal and in a broadband fashion. This is realized (as described briefly in Chapter 3) by first implementing a 180° phase shift on the RF, and later by implementing a division by 2, resulting in signals that have a phase shift of 90° . These RF lines are then amplified by chains of inverters and sent to the two mixers. The main challenge in this design was to guarantee the broadband operation: it is indeed known that the frequency division is problematic in digital circuits at low frequency, due to the leakage currents that are present in the MOSFETs. However, the design detailed here is capable of operation from 3 MHz (yielding a phase error of 3°) up to 1 GHz (yielding a phase error of 0.3°). The design was optimized via simulations in Cadence. Figure 5.9 shows the transistor level schematics of the 180° phase shifter, which is essentially constituted by two differential inverter chains where a dummy inverter equalizes eventual path delays. Figure 5.10 shows the schematics of the dividers, whose topology is the TPSC. An inverter interfaces the divider to the successive stage.

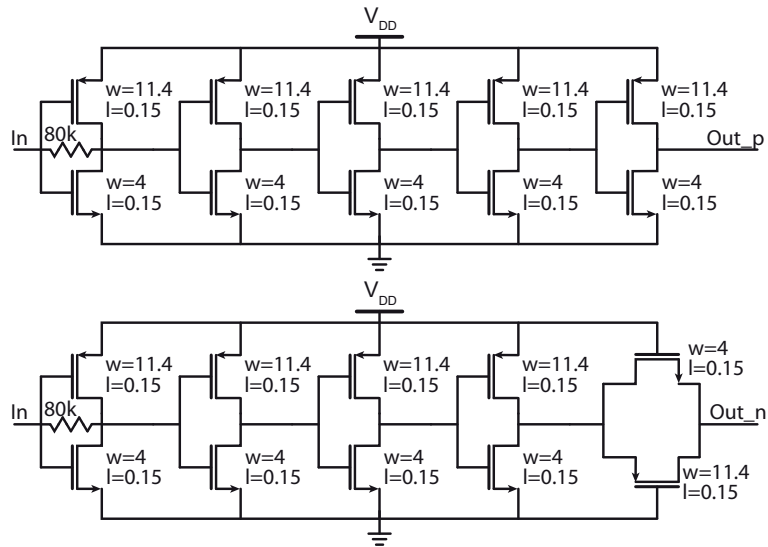


Figure 5.9: **180° Shift.** Transistor level schematics of the 180° phase shifter.

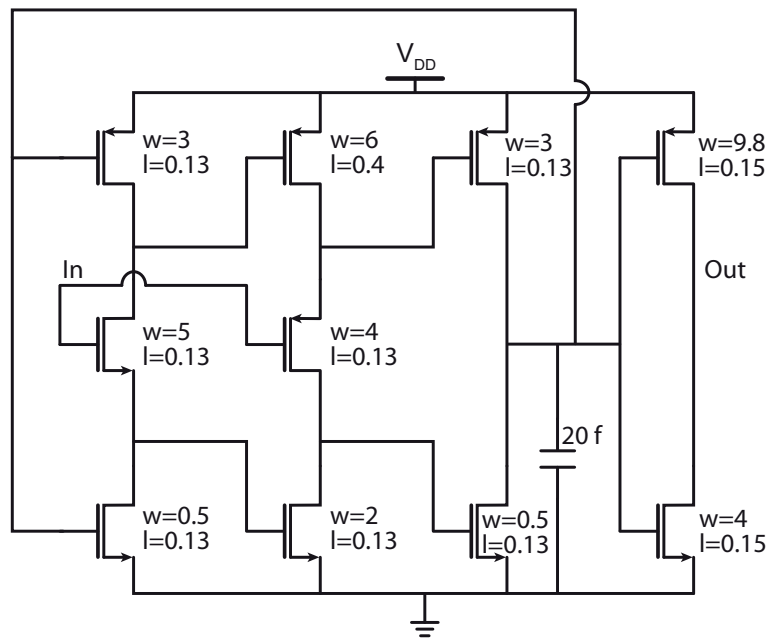


Figure 5.10: **Divider.** Transistor level schematics of the broadband divider.

Chips bonding and use

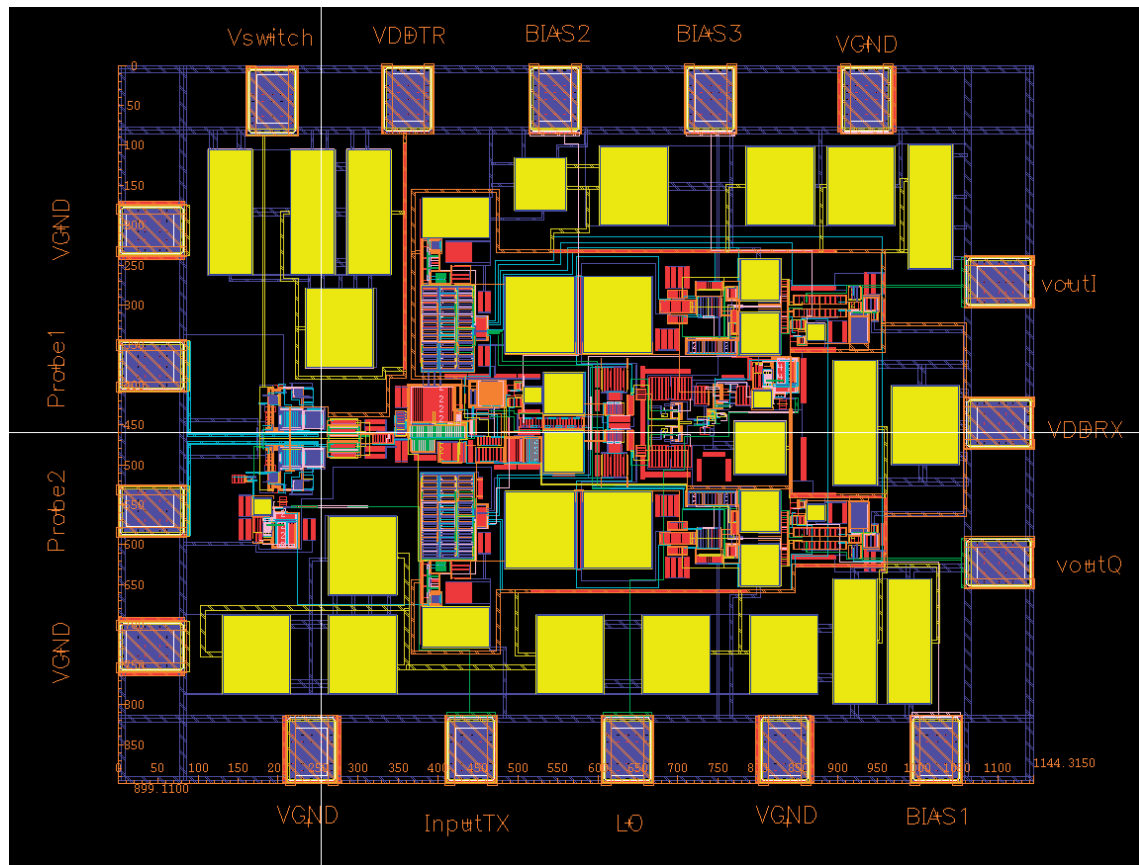


Figure 5.11: **IQ transceiver, 2015.** Virtuoso Layout view of the designed IQ transceiver. This version of the chip interfaces to external excitation/detection resonators.

Figure 5.11 shows the Cadence Virtuoso view of the final layout of the IQ transceiver designed to interface with external excitation/detection probe heads. Here we want to describe the role of each pin to enable future use of this design.

Probe1 and Probe2 The two nodes indicated as probes correspond to the nodes a and \bar{a} (see fig. 5.8 and chapter 3). Any PCB routing should consider that the nodes are differential.

InputTX This node is the RF input of the transmitter. The RF source needs to be AC coupled with a capacitance of 100 pF (or similar). The input is self biased. RF power can be as low as -3 dBm.

Vswitch This node manages the transceiver TX to RX switching. When equal to 2.5 V the transceiver is in RX mode. When equal to ground the transceiver is in TX mode. To

Chapter 5. Appendix: supplementary, designs

interface Vswitch to an external standard TTL signal we typically use an inverter fed by 2.5 V before the pin.

VDDTR Here we feed the switches and transmitter with a 2.5 V power source.

VGND All pins with this name are connected to ground.

BIAS1, BIAS2, and BIAS3 These nodes connect to bias points within the receiver and can be used for testing only. They can be connected to floating pads on the PCB and can be used to check the presence of 1 V on each. They can be left floating too if testing is not needed.

LO This node is the RF input of the local oscillator. The RF source needs to be AC coupled with a capacitance of 100 pF (or similar). The input is self biased. RF power can be as low as -3 dBm (depending on the working frequency).

VDDRX Here we feed the whole receiver with a 1.5 V power source.

voutI and voutQ The IQ output pins of the receiver. The DC value has to be about 1 V. The maximum output is about 300-400 mV. We typically interface this pin to an AC coupled AF amplifier. The output is proved to directly drive coaxial cables as long as 2-3 meters. Make sure the electronic paths are identical for these two channels.

Appendix C: Extrapolation of sensitivity of our single-chip probe at higher fields

The free induction decay (FID) NMR signal consists of several contributions at slightly different frequencies. Each contribution has an angular frequency $\omega_0 = \gamma_{eff} B_0$, where γ_{eff} is the effective gyromagnetic ratio of the probed nuclei and depends on their chemical environment. In general, the signal contribution at each frequency is $s(t) = s_0 \cos(\omega_0 t) e^{-t/T_2^*}$, where T_2^* is the effective decay time depending on the spin-spin relaxation time and the field inhomogeneity in the sample volume. As described in Chapter 1, the NMR signal is $s_0 = \omega_0 M_0 B_u V_s \sin(\theta)$ accordingly to eq. (1.6), where V_s is the sample volume, B_u is the magnetic field generated by a current of 1 A in the detection coil (i.e., the so called unitary field). It is worth to note here that the term M_0 is proportional to the value of the static field B_0 , as shown in eq. (1.2). As shown in Chapter 1, the SNR for a single scan is maximized by multiplying the time-domain signal by an exponential function whose decay match T_2^* . After this operation and for an acquisition time $T \gg T_2^*$ the SNR in the frequency domain is given by eq. (1.20):

$$SNR_f = \frac{s_0}{n_{sd}} \sqrt{\frac{T_2^*}{2}} \quad (5.7)$$

where n_{sd} is the noise spectral density of the detector. Assuming that in our experiments on single ova reported in Chapter 4 the measured linewidth are due to field distortions caused by susceptibility mismatches (sort of a worst-case scenario), we have that the linewidth increases linearly with the static field (i.e., $T_2^* \propto \frac{1}{B_0}$). Since s_0 scales quadratically with the static field (i.e., $s_0 \propto B_0^2$), the SNR in eq. (5.7) scales as $B_0^{3/2}$. Hence, for a field change from 7 T to 23.5 T, we expect a SNR improvement of about a factor six. In this extrapolation of the sensitivity at higher fields, we assumed that the noise spectral density does not depend on the operating field and that the same coil (i.e., same B_u) can be used. This is a good assumption for microcoils having a self-resonance frequency above the operating frequency and a coil metal thickness similar or smaller than the skin depth, as in the case of the integrated microcoil used in this work.

6 Conclusions and Outlook

Conclusions

In this thesis we described the design, implementation and use of both compact and ultra-compact NMR probes based on broadband 1 mm² CMOS single-chip transceivers.

We described the use of CMOS transceivers in combination with external excitation/detection probe heads to obtain versatile designs of what we may call compact probes (i.e. probes where the overall size is dominated by the excitation/detection resonator itself). In this frame we showed two applications. In one case we combined CMOS transceivers and microsolenoids having an active volume of 100 nL. We used a variable frequency probe design to perform multi-nuclear NMR detection with a single coil on ¹H, ¹⁹F, ¹B, ²³Na. In this work we showed that a combination of CMOS transceivers and microsolenoids can be used to obtain good performance in terms of spin sensitivities and, eventually, spectral resolution. A second compact design stemmed from the combination of our transceivers with commercial teslamer probe heads (from Metrolab SA). In this work we realized prototypes of commercial probes aimed for high field magnetometry, and showed that even in this case the use of CMOS transceivers allows for performance that compares well to the state of art. Moreover, we used our transceivers to build a custom 2-channel probe for simultaneous field monitoring on more than one channel and used this tool to corroborate two facts: one is that a sample of pure water of 500 nL is sufficient to detect magnetic field noise inside the bore of our 7 T Bruker magnet, another is that CMOS chips ease significantly the design and implementation of compact NMR probes.

We also described the use of CMOS transceivers in combination with on-chip multilayer non-resonant microcoils to obtain versatile designs of what we may call ultra-compact NMR probes. We showed a calibration of such sensor via ¹H and ¹⁹F NMR spectroscopy of solid samples. As a result, we reported a spin sensitivity of $1.5 \cdot 10^{13}$ spins/Hz^{1/2} at 7 T within an active volume of about 200 pL. We noted that the volume scale reached with this approach is

biologically relevant in terms of the diversity of samples present in nature. The spin sensitivity compares well to the state of art of sub-nL NMR probes and the resulting ultra-compact planar device shows an exceptional degree of versatility. Thanks to its robustness and its planar geometry we could, indeed, perform a first extensive NMR spectroscopic study of untouched sub-nL individual static ova. We carried out this investigation in a relatively weak field of 7 T. We selected ova of two species of microorganisms, namely *Richtersius coronifer* and *Heligmosomoides polygyrus bakeri*, and showed that a LOD of about 5 pmol of ^1H nuclei is sufficient for the detection of the most concentrated compounds in individual ova of microorganisms having volumes below 1 nL. The results shown may be used as a starting point to extrapolate the realistic experimental possibilities offered by NMR ultra-compact probes for applications such as the non-invasive selection of microscopic entities based on the direct quantification of highly concentrated endogenous compounds.

Outlook

The observed spectroscopy of sub-nL ova seem to indicate that ultra-compact CMOS probes can achieve sensitivities sufficient for the detection of endogenous compounds. Another indication is that spectral heterogeneities can be detected already at 7 T and with LODs of about 5 pmol. Sensitivity performance can improve with the use of a higher field. At 1 GHz it is reasonable to achieve limits of detection on ^1H nuclei in the order of 7 pmol in 10 minutes and 0.9 pmol in 10 hours for samples having a volume below 100 pl and linewidths as large as 0.3 ppm. Further improvements are obvious for samples exhibiting typical linewidths narrower than the ones observed by us. Different coil designs and an improved electronics might, at higher frequencies, allow for going beyond this simple projection. Overall, the achievement of LODs in the mM range over objects having volumes in the sub-nL region is a first future challenge and follow up of this work. Such performance will allow for in-vivo NMR spectroscopy at metabolic concentrations on relevant biological samples. A peculiar class of sub-nL ova that justifies the interest in approaches for the non-invasive intracellular spectroscopy of individual samples is constituted by the mammalian zygotes. As referenced in Chapter 4, the direct application of NMR on single embryos using miniaturized high sensitivity probes is potentially useful to provide new data that could shed light on cryptic processes involved in embryonic development and provide new methodologies to estimate embryonic health.

The hardware used in this work is an ultra-compact integrated probe entirely realized with commercially accessible complementary-metal-oxide-semiconductor (CMOS) technologies that might open to the realistic possibility of implementing relatively low-cost arrayed miniaturized probes. However, improvements for what concern samples manipulation are required, especially for applications aiming at studying precious samples such as mammalian embryos. Both integrated circuits and microfluidics are suitable for arrays implementation. We believe that this combination can be extended to NMR applications for the realization of arrayed high

sensitivity NMR probes, enabling simultaneous studies on a large number of single biological entities in the same magnet.

Last, CMOS microchips have been proven to work at cryogenic temperatures above 20 °K. Another interesting future challenge is to realize fully functional CMOS cryogenic transceivers for broadband cryo-NMR operation. Such implementation would allow for eased electronics designs of various cryo-cooled NMR probes with exceptional noise performance.

Acknowledgement

First, I would like to thank Giovanni for his supervision, and in particular for his consistent technical knowledge often at service in the laboratory. The success of many experiments strictly depended on his presence, his will to push the limits, and his enthusiastic attitude towards his job.

Second, I would like to thank Gabriele for guiding me into the design of integrated circuits, opening to me the door into a new world that gave me so much in the past four years.

Thank you Enrica for being always there to share ideas, and thank you Alessandro for being such a good office mate.

I want to express my gratitude to all members of LMIS1 making the environment of this laboratory so nice and calm: the perfect playground to develop new technologies and new science. Thank you Jürgen for managing this laboratory taking care of all details, thank you Severine for being always available for any issue, thank you Samuel, Mathieu, Qiyuan, Mohammad, Thomas, Henry, Ya, Jonas, Mattia, and all those that I may have forgot in this probably too short list.

A special acknowledgement goes to the people from Villanueva's group: Annalisa, Andrea, Kaitlin, Tom.

A big thank you goes to Franck Vincent for his interest and high consideration of my work, and for the nice collaboration we had together.

A special acknowledgement goes to the team of Metrolab, and in particular to Pascal, Jacques, Simon, Philip.

Thank you Esra for being always available for a chat enjoying a coffee together, making a few days a bit lighter than they were.

A special thank you goes to Orlando and Benjamin, always making an effort to meet my needs. Without your support my whole PhD would have been much less inspired and exciting.

A big thank you goes to my family, who always supported me since when I was a kid to pursue my inner instinct at any cost. Mamma, Papà, Luigi, Matteo, I am the very first doctor in our big family! I am proud of where I stand now. But I am much more proud of where I am coming from. And this is certainly because of you: thank you.

Finally, a huge thank you goes to my soul mate Erika, who gave me unparalleled support during these years. Thank you for being just the way you are. You are a great woman.

Bibliography

- [1] Felix Bloch. Nuclear induction. *Physical review*, 70(7-8):460, 1946.
- [2] F Bloch, M Packard, and WW Hansen. The nuclear experiment. *Physical Review*, 70:474–485, 1946.
- [3] David I Hoult and RE Richards. The signal-to-noise ratio of the nuclear magnetic resonance experiment. *Journal of Magnetic Resonance (1969)*, 24(1):71–85, 1976.
- [4] Richard R Ernst, Geoffrey Bodenhausen, Alexander Wokaun, et al. *Principles of nuclear magnetic resonance in one and two dimensions*, volume 14. Clarendon Press Oxford, 1987.
- [5] Paul T. Callaghan. *Principles of nuclear magnetic resonance microscopy*. Oxford University Press on Demand, 1993.
- [6] Anatole Abragam and HY Carr. *The principles of nuclear magnetism*. AIP, 1961.
- [7] Malcolm H Levitt. *Spin dynamics: basics of nuclear magnetic resonance*. John Wiley & Sons, 2001.
- [8] Nan Sun, Yong Liu, Ling Qin, Hakho Lee, Ralph Weissleder, and Donhee Ham. Small nmr biomolecular sensors. *Solid-State Electronics*, 84:13–21, 2013.
- [9] Ka-Meng Lei, Hadi Heidari, Pui-In Mak, Man-Kay Law, Franco Maloberti, and Rui P Martins. A handheld high-sensitivity micro-nmr cmos platform with b-field stabilization for multi-type biological/chemical assays. *IEEE Journal of Solid-State Circuits*, 2016.
- [10] Hakho Lee, Eric Sun, Donhee Ham, and Ralph Weissleder. Chip-nmr biosensor for detection and molecular analysis of cells. *Nature medicine*, 14(8):869–874, 2008.
- [11] Ka-Meng Lei, Pui-In Mak, Man-Kay Law, and Rui P Martins. Nmr-dmf: a modular nuclear magnetic resonance-digital microfluidics system for biological assays. *Analyst*, 139(23):6204–6213, 2014.
- [12] Nan Sun, Tae-Jong Yoon, Hakho Lee, William Andress, Ralph Weissleder, and Donhee Ham. Palm nmr and 1-chip nmr. *IEEE Journal of Solid-State Circuits*, 46(1):342–352, 2011.

Bibliography

- [13] Dongwan Ha, Jeffrey Paulsen, Nan Sun, Yi-Qiao Song, and Donhee Ham. Scalable nmr spectroscopy with semiconductor chips. *Proceedings of the National Academy of Sciences*, 111(33):11955–11960, 2014.
- [14] Ka-Meng Lei, Pui-In Mak, Man-Kay Law, and Rui P Martins. A palm-size μ nmr relaxometer using a digital microfluidic device and a semiconductor transceiver for chemical/biological diagnosis. *Analyst*, 140(15):5129–5137, 2015.
- [15] Yong Liu, Nan Sun, Hakho Lee, Ralph Weissleder, and Donhee Ham. Cmos mini nuclear magnetic resonance system and its application for biomolecular sensing. In *Solid-State Circuits Conference, 2008. ISSCC 2008. Digest of Technical Papers. IEEE International*, pages 140–602. IEEE, 2008.
- [16] Nan Sun, Yong Liu, Hakho Lee, Ralph Weissleder, and Donhee Ham. Cmos rf biosensor utilizing nuclear magnetic resonance. *IEEE Journal of Solid-State Circuits*, 44(5):1629–1643, 2009.
- [17] Nan Sun, Tae-Jong Yoon, Hakho Lee, William Andress, Ralph Weissleder, and Donhee Ham. Palm nmr and 1-chip nmr. *IEEE Journal of Solid-State Circuits*, 46(1):342–352, 2011.
- [18] Jaehyup Kim, Bruce Hammer, and Ramesh Harjani. A 5–300mhz cmos transceiver for multi-nuclear nmr spectroscopy. In *Custom Integrated Circuits Conference (CICC), 2012 IEEE*, pages 1–4. IEEE, 2012.
- [19] Ka-Meng Lei, Pui-In Mak, Man-Kay Law, and Rui P Martins. A μ nmr cmos transceiver using a butterfly-coil input for integration with a digital microfluidic device inside a portable magnet. *IEEE Journal of Solid-State Circuits*, 51(10):2274–2286, 2016.
- [20] Ka-Meng Lei, Hadi Heidari, Pui-In Mak, Man-Kay Law, Franco Maloberti, and Rui P Martins. A handheld 50pm-sensitivity micro-nmr cmos platform with b-field stabilization for multi-type biological/chemical assays. In *Solid-State Circuits Conference (ISSCC), 2016 IEEE International*, pages 474–475. IEEE, 2016.
- [21] Marco Grisi, Gabriele Gualco, and Giovanni Boero. A broadband single-chip transceiver for multi-nuclear nmr probes. *Review of Scientific Instruments*, 86(4):044703, 2015.
- [22] Jens Anders, Jonas Handwerker, Maurits Ortmanns, and Giovanni Boero. A fully-integrated detector for nmr microscopy in 0.13 μ m cmos. In *Solid-State Circuits Conference (A-SSCC), 2013 IEEE Asian*, pages 437–440. IEEE, 2013.
- [23] Jens Anders, Jonas Handwerker, Maurits Ortmanns, and Giovanni Boero. A low-power high-sensitivity single-chip receiver for nmr microscopy. *Journal of Magnetic Resonance*, 266:41–50, 2016.
- [24] Jens Anders and Giovanni Boero. A low-noise cmos receiver frontend for mri. In *Biomedical Circuits and Systems Conference, 2008. BioCAS 2008. IEEE*, pages 165–168. IEEE, 2008.

-
- [25] Jens Anders, Paul SanGiorgio, and Giovanni Boero. An integrated cmos receiver chip for nmr-applications. In *Custom Integrated Circuits Conference, 2009. CICC'09. IEEE*, pages 471–474. IEEE, 2009.
- [26] Jens Anders, Giuseppe Chiaramonte, Paul SanGiorgio, and Giovanni Boero. A single-chip array of nmr receivers. *Journal of Magnetic Resonance*, 201(2):239–249, 2009.
- [27] Jens Anders, Paul SanGiorgio, Xeni Deligianni, Francesco Santini, Klaus Scheffler, and Giovanni Boero. Integrated active tracking detector for mri-guided interventions. *Magnetic resonance in medicine*, 67(1):290–296, 2012.
- [28] Jens Anders, Paul SanGiorgio, and Giovanni Boero. A fully integrated iq-receiver for nmr microscopy. *Journal of Magnetic Resonance*, 209(1):1–7, 2011.
- [29] G Boero, J Frounchi, B Furrer, P-A Besse, and RS Popovic. Fully integrated probe for proton nuclear magnetic resonance magnetometry. *Review of Scientific Instruments*, 72(6):2764–2768, 2001.
- [30] Erwin L Hahn. Spin echoes. *Physical review*, 80(4):580, 1950.
- [31] Saul Meiboom and David Gill. Modified spin-echo method for measuring nuclear relaxation times. *Review of scientific instruments*, 29(8):688–691, 1958.
- [32] Andrew G Webb. Radiofrequency microcoils in magnetic resonance. *Progress in Nuclear Magnetic Resonance Spectroscopy*, 31(1):1–42, 1997.
- [33] Sunderarajan S Mohan, Maria del Mar Hershenson, Stephen P Boyd, and Thomas H Lee. Simple accurate expressions for planar spiral inductances. *IEEE Journal of solid-state circuits*, 34(10):1419–1424, 1999.
- [34] Hossein Pourmodheji, Ebrahim Ghafar-Zadeh, and Sebastian Magierowski. A multi-disciplinary approach to high throughput nuclear magnetic resonance spectroscopy. *Sensors*, 16(6):850, 2016.
- [35] Hossein Pourmodheji, Ebrahim Ghafar-Zadeh, and Sebastian Magierowski. Active nuclear magnetic resonance probe: A new multidisciplinary approach toward highly sensitive biomolecular spectroscopy. In *Circuits and Systems (ISCAS), 2015 IEEE International Symposium on*, pages 473–476. IEEE, 2015.
- [36] Tewfik Cherifi, Nacer Abouchi, Guo-Neng Lu, Latifa Bouchet-Fakri, Laurent Quiquerez, Brice Sorli, J-F Chateaux, M Pitaval, and Pierre Morin. A cmos microcoil-associated preamplifier for nmr spectroscopy. *IEEE Transactions on Circuits and Systems I: Regular Papers*, 52(12):2576–2583, 2005.
- [37] V Badilita, K Kratt, N Baxan, J Anders, D Elverfeldt, G Boero, J Hennig, JG Korvink, and U Wallrabe. 3d solenoidal microcoil arrays with cmos integrated amplifiers for parallel mr imaging and spectroscopy. In *Micro Electro Mechanical Systems (MEMS), 2011 IEEE 24th International Conference on*, pages 809–812. IEEE, 2011.

Bibliography

- [38] Jaehyup Kim, Bruce Hammer, and Ramesh Harjani. A low power cmos receiver for a tissue monitoring nmr spectrometer. In *VLSI Circuits (VLSIC), 2010 IEEE Symposium on*, pages 221–222. IEEE, 2010.
- [39] Mazin Jouada, Oliver G Gruschke, and Jan G Korvink. A new fully integrated multichannel receiver design for magnetic resonance imaging. *Concepts in Magnetic Resonance Part B: Magnetic Resonance Engineering*, 46(3):134–145, 2016.
- [40] Walker J Turner and Rizwan Bashirullah. A 4.7 t/11.1 t nmr compliant 50 nw wirelessly programmable implant for bioartificial pancreas in vivo monitoring. *IEEE Journal of Solid-State Circuits*, 51(2):473–483, 2016.
- [41] AG Goloshevsky, JH Walton, MV Shutov, JS De Ropp, SD Collins, and MJ McCarthy. Development of low field nuclear magnetic resonance microcoils. *Review of scientific instruments*, 76(2):024101, 2005.
- [42] Graeme Finch, Ali Yilmaz, and Marcel Utz. An optimised detector for in-situ high-resolution nmr in microfluidic devices. *Journal of Magnetic Resonance*, 262:73–80, 2016.
- [43] K Ehrmann, M Gersbach, P Pascoal, F Vincent, C Massin, D Stamou, P-A Besse, H Vogel, and RS Popovic. Sample patterning on nmr surface microcoils. *Journal of Magnetic Resonance*, 178(1):96–105, 2006.
- [44] Oliver G Gruschke, Nicoleta Baxan, Lars Clad, Kai Kratt, Dominik von Elverfeldt, Andreas Peter, Jürgen Hennig, Vlad Badilita, Ulrike Wallrabe, and Jan G Korvink. Lab on a chip phased-array mr multi-platform analysis system. *Lab on a Chip*, 12(3):495–502, 2012.
- [45] C Massin, F Vincent, A Homsy, K Ehrmann, G Boero, P-A Besse, A Daridon, E Verpoorte, NF De Rooij, and RS Popovic. Planar microcoil-based microfluidic nmr probes. *Journal of Magnetic Resonance*, 164(2):242–255, 2003.
- [46] Jonathan D Trumbull, Ian K Glasgow, David J Beebe, and Richard L Magin. Integrating microfabricated fluidic systems and nmr spectroscopy. *IEEE Transactions on Biomedical Engineering*, 47(1):3–7, 2000.
- [47] K Yamauchi, JWG Janssen, and APM Kentgens. Implementing solenoid microcoils for wide-line solid-state nmr. *Journal of Magnetic Resonance*, 167(1):87–96, 2004.
- [48] L Renaud, M Armenean, L Berry, P Kleimann, P Morin, M Pitaval, J O’Brien, M Brunet, and H Saint-Jalmes. Implantable planar rf microcoils for nmr microspectroscopy. *Sensors and Actuators A: Physical*, 99(3):244–248, 2002.
- [49] C Massin, G Boero, F Vincent, J Abenheim, P-A Besse, and RS Popovic. High-q factor rf planar microcoils for micro-scale nmr spectroscopy. *Sensors and Actuators A: Physical*, 97:280–288, 2002.

-
- [50] R Subramanian, MM Lam, and AG Webb. Rf microcoil design for practical nmr of mass-limited samples, 1998.
- [51] Vlad Badilita, Kai Kratt, Nicoleta Baxan, Mohammad Mohmmadzadeh, Tobias Burger, Hans Weber, Dominik v Elverfeldt, Jürgen Hennig, Jan G Korvink, and Ulrike Wallrabe. On-chip three dimensional microcoils for mri at the microscale. *Lab on a Chip*, 10(11):1387–1390, 2010.
- [52] PJM Van Bentum, JWG Janssen, APM Kentgens, J Bart, and JGE Gardeniers. Stripline probes for nuclear magnetic resonance. *Journal of Magnetic Resonance*, 189(1):104–113, 2007.
- [53] Yael Maguire, Isaac L Chuang, Shuguang Zhang, and Neil Gershenfeld. Ultra-small-sample molecular structure detection using microslot waveguide nuclear spin resonance. *Proceedings of the National Academy of Sciences*, 104(22):9198–9203, 2007.
- [54] Kevin R Minard and Robert A Wind. Picoliter 1 h nmr spectroscopy, 2002.
- [55] Hans Georg Krojanski, Jörg Lambert, Yilmaz Gerikalan, Dieter Suter, and Roland Hergenröder. Microslot nmr probe for metabolomics studies. *Analytical chemistry*, 80(22):8668–8672, 2008.
- [56] John A Rogers, Rebecca J Jackman, George M Whitesides, Dean L Olson, and Jonathan V Sweedler. Using microcontact printing to fabricate microcoils on capillaries for high resolution proton nuclear magnetic resonance on nanoliter volumes. *Applied physics letters*, 70(18):2464–2466, 1997.
- [57] Dean L Olson, Timothy L Peck, Andrew G Webb, Richard L Magin, and Jonathan V Sweedler. High-resolution microcoil 1h-nmr for mass-limited, nanoliter-volume samples. *Science*, 270(5244):1967, 1995.
- [58] JE Stocker, TL Peck, AG Webb, M Feng, and RL Magin. Nanoliter volume, high-resolution nmr microspectroscopy using a 60-/spl mu/m planar microcoil. *IEEE Transactions on biomedical engineering*, 44(11):1122–1127, 1997.
- [59] DA Seeber, RL Cooper, L Ciobanu, and CH Pennington. Design and testing of high sensitivity microreceiver coil apparatus for nuclear magnetic resonance and imaging. *Review of Scientific Instruments*, 72(4):2171–2179, 2001.
- [60] Timothy L Peck, Richard L Magin, and Paul C Lauterbur. Design and analysis of microcoils for nmr microscopy. *Journal of Magnetic Resonance, Series B*, 108(2):114–124, 1995.
- [61] Harry Nyquist. Thermal agitation of electric charge in conductors. *Physical review*, 32(1):110, 1928.

Bibliography

- [62] Richard G Spencer. Equivalence of the time-domain matched filter and the spectral-domain matched filter in one-dimensional nmr spectroscopy. *Concepts in Magnetic Resonance Part A*, 36(5):255–265, 2010.
- [63] Vlad Badilita, Robert Ch Meier, Nils Spengler, Ulrike Wallrabe, Marcel Utz, and Jan G Korvink. Microscale nuclear magnetic resonance: a tool for soft matter research. *Soft Matter*, 8(41):10583–10597, 2012.
- [64] Michael E Lacey, Raju Subramanian, Dean L Olson, Andrew G Webb, and Jonathan V Sweedler. High-resolution nmr spectroscopy of sample volumes from 1 nl to 10 μ l. *Chemical reviews*, 99(10):3133–3152, 1999.
- [65] J Bart, JWG Janssen, PJM Van Bentum, APM Kentgens, and JGE Gardeniers. Optimization of stripline-based microfluidic chips for high-resolution nmr. *Journal of Magnetic Resonance*, 201(2):175–185, 2009.
- [66] Jacob Bart, Ard J Kolkman, Anna Jo Oosthoek-de Vries, Kaspar Koch, Pieter J Nieuwland, Hans Janssen, Jan van Bentum, Kirsten AM Ampt, Floris PJT Rutjes, Sybren S Wijmenga, et al. A microfluidic high-resolution nmr flow probe. *Journal of the American Chemical Society*, 131(14):5014–5015, 2009.
- [67] Herbert Ryan, Alison Smith, and Marcel Utz. Structural shimming for high-resolution nuclear magnetic resonance spectroscopy in lab-on-a-chip devices. *Lab on a Chip*, 14(10):1678–1685, 2014.
- [68] R Kamberger, A Moazen-zadeh, JG Korvink, and OG Gruschke. Hollow microcoils made possible with external support structures manufactured with a two-solvent process. *Journal of Micromechanics and Microengineering*, 26(6):065002, 2016.
- [69] AG Webb and SC Grant. Signal-to-noise and magnetic susceptibility trade-offs in solenoidal microcoils for nmr. *Journal of Magnetic Resonance, Series B*, 113(1):83–87, 1996.
- [70] Andreas C Fischer, Jan G Korvink, Niclas Roxhed, Göran Stemme, Ulrike Wallrabe, and Frank Niklaus. Unconventional applications of wire bonding create opportunities for microsystem integration. *Journal of Micromechanics and Microengineering*, 23(8):083001, 2013.
- [71] Matthias C Wapler, Jochen Leupold, Iulius Dragonu, Dominik von Elverfeld, Maxim Zaitsev, and Ulrike Wallrabe. Magnetic properties of materials for mr engineering, micro-mr and beyond. *Journal of Magnetic Resonance*, 242:233–242, 2014.
- [72] A Abragam. The principles of magnetic resonance. clarendon, 1961.
- [73] Ian L Pykett. Nmr imaging in medicine. *Scientific American*, 246(5):78–88, 1982.
- [74] R Haken and B Blümich. Anisotropy in tendon investigated in vivo by a portable nmr scanner, the nmr-mouse. *Journal of Magnetic Resonance*, 144(2):195–199, 2000.

- [75] H Kühn, M Klein, A Wiesmath, DE Demco, B Blümich, J Kelm, and PW Gold. The nmr-mouse®: quality control of elastomers. *Magnetic resonance imaging*, 19(3):497–499, 2001.
- [76] Raffaele Sacchi, Francesco Addeo, and Livio Paolillo. 1h and 13c nmr of virgin olive oil. an overview. *Magnetic Resonance in Chemistry*, 35(13), 1997.
- [77] <http://www.picospin.com/>.
- [78] <http://www.nmr-mouse.de/>.
- [79] Peter J Mohr, David B Newell, and Barry N Taylor. Codata recommended values of the fundamental physical constants: 2014. *Journal of Physical and Chemical Reference Data*, 45(4):043102, 2016.
- [80] HS Gutowsky, LH Meyer, and RE McClure. Apparatus for nuclear magnetic resonance. *Review of Scientific Instruments*, 24(8):644–652, 1953.
- [81] Klaus Halbach. Design of permanent multipole magnets with oriented rare earth cobalt material. *Nuclear instruments and methods*, 169(1):1–10, 1980.
- [82] Ernesto Danieli, Juan Perlo, Bernhard Blümich, and Federico Casanova. Small magnets for portable nmr spectrometers. *Angewandte Chemie International Edition*, 49(24):4133–4135, 2010.
- [83] Raluca M Fratila, M Victoria Gomez, Stanislav Šykora, and Aldrik H Velders. Multinuclear nanoliter one-dimensional and two-dimensional nmr spectroscopy with a single non-resonant microcoil. *Nature communications*, 5, 2014.
- [84] Dean L Olson, Timothy L Peck, Andrew G Webb, Richard L Magin, and Jonathan V Sweedler. High-resolution microcoil 1h-nmr for mass-limited, nanoliter-volume samples. *Science*, 270(5244):1967, 1995.
- [85] Thomas H Lee. *The design of CMOS radio-frequency integrated circuits*. Cambridge university press, 2003.
- [86] WG Proctor and FC Yu. The dependence of a nuclear magnetic resonance frequency upon chemical compound. *Physical Review*, 77(5):717, 1950.
- [87] Nicolaas Bloembergen, Edward Mills Purcell, and Robert V Pound. Relaxation effects in nuclear magnetic resonance absorption. *Physical review*, 73(7):679, 1948.
- [88] Karl Kuhlmann and David M Grant. Spin-spin coupling in the tetrafluoroborate ion^{1a}. *The Journal of Physical Chemistry*, 68(11):3208–3213, 1964.
- [89] Robin K Harris, Edwin D Becker, Sonia M Cabral De Menezes, Pierre Granger, Roy E Hoffman, Kurt W Zilm, et al. Further conventions for nmr shielding and chemical shifts iupac recommendations 2008. *Solid state nuclear magnetic resonance*, 33(3):41–56, 2008.

Bibliography

- [90] Hisaya Sato and Yasuyuki Tanaka. 1h-nmr study of polyisoprenes. *Journal of Polymer Science: Polymer Chemistry Edition*, 17(11):3551–3558, 1979.
- [91] Nicola De Zanche, Christoph Barmet, Jurek A Nordmeyer-Massner, and Klaas P Pruessmann. Nmr probes for measuring magnetic fields and field dynamics in mr systems. *Magnetic resonance in medicine*, 60(1):176–186, 2008.
- [92] P Sipilä, D Lange, S Lechner, W Löw, P Gross, M Baller, G Wachutka, and F Wiesinger. Robust, susceptibility-matched nmr probes for compensation of magnetic field imperfections in magnetic resonance imaging (mri). *Sensors and Actuators A: Physical*, 145:139–146, 2008.
- [93] Xiang Fei, VW Hughes, and Ralf Prigl. Precision measurement of the magnetic field in terms of the free-proton nmr frequency. *Nuclear Instruments and Methods in Physics Research Section A: Accelerators, Spectrometers, Detectors and Associated Equipment*, 394(3):349–356, 1997.
- [94] R Prigl, Ulrich Haerberlen, K Jungmann, G Zu Putlitz, and P Von Walter. A high precision magnetometer based on pulsed nmr. *Nuclear Instruments and Methods in Physics Research Section A: Accelerators, Spectrometers, Detectors and Associated Equipment*, 374(1):118–126, 1996.
- [95] JL Flowers, BW Petley, and MG Richards. A measurement of the nuclear magnetic moment of the helium-3 atom in terms of that of the proton. *Metrologia*, 30(2):75, 1993.
- [96] G Boero, C de Raad Iseli, PA Besse, and RS Popovic. An nmr magnetometer with planar microcoils and integrated electronics for signal detection and amplification. *Sensors and Actuators A: Physical*, 67(1-3):18–23, 1998.
- [97] Andreas Maul, Peter Blümmler, Werner Heil, Anna Nikiel, Ernst Otten, Andreas Petrich, and Thomas Schmidt. Spherical fused silica cells filled with pure helium for nuclear magnetic resonance-magnetometry. *Review of Scientific Instruments*, 87(1):015103, 2016.
- [98] V Reymond. Magnetic resonance techniques. 1998.
- [99] C Schott, RS Popovic, S Alberti, and MQ Tran. High accuracy magnetic field measurements with a hall probe. *Review of scientific instruments*, 70(6):2703–2707, 1999.
- [100] C Gemmel, W Heil, S Karpuk, K Lenz, Ch Ludwig, Yu Sobolev, K Tullney, M Burghoff, W Kilian, S Knappe-Grüneberg, et al. Ultra-sensitive magnetometry based on free precession of nuclear spins. *The European Physical Journal D-Atomic, Molecular, Optical and Plasma Physics*, 57(3):303–320, 2010.
- [101] N Kernevez and H Glenat. Description of a high sensitivity cw scalar dnp-nmr magnetometer. *IEEE Transactions on magnetics*, 27(6):5402–5404, 1991.

-
- [102] BC Woo, CG Kim, Po Gyu Park, CS Kim, and VY Shifrin. Low magnetic field measurement by a separated nmr detector using flowing water. *IEEE Transactions on magnetics*, 33(5):4345–4348, 1997.
- [103] Haroon Aman and Taras Plakhotnik. Accuracy in the measurement of magnetic fields using nitrogen-vacancy centers in nanodiamonds. *JOSA B*, 33(3):B19–B27, 2016.
- [104] VM Acosta, E Bauch, MP Ledbetter, C Santori, K-MC Fu, PE Barclay, RG Beausoleil, H Linget, JF Roch, F Treussart, et al. Diamonds with a high density of nitrogen-vacancy centers for magnetometry applications. *Physical Review B*, 80(11):115202, 2009.
- [105] Zoran D Grujić, Peter A Koss, Georg Bison, and Antoine Weis. A sensitive and accurate atomic magnetometer based on free spin precession. *The European Physical Journal D*, 69(5):135, 2015.
- [106] P Sipilä, D Lange, S Lechner, W Löw, P Gross, M Baller, G Wachutka, and F Wiesinger. Robust, susceptibility-matched nmr probes for compensation of magnetic field imperfections in magnetic resonance imaging (mri). *Sensors and Actuators A: Physical*, 145:139–146, 2008.
- [107] Metrolab. <http://www.metrolab.com/>.
- [108] Bruker. <http://www.bruker.com/>.
- [109] Yuan Ji-Ren, Ingemar Karlsson, and Christer Svensson. A true single-phase-clock dynamic cmos circuit technique. *IEEE Journal of Solid-State Circuits*, 22(5):899–901, 1987.
- [110] Behzad Razavi and Razavi Behzad. *RF microelectronics*, volume 2. Prentice Hall New Jersey, 1998.
- [111] Francis Hartmann. Resonance magnetometers. *IEEE Transactions on Magnetics*, 8(1):66–75, 1972.
- [112] H Yan, K Li, R Khatiwada, E Smith, WM Snow, CB Fu, P-H Chu, H Gao, and W Zheng. A frequency determination method for digitized nmr signals. *Communications in Computational Physics*, 15(05):1343–1351, 2014.
- [113] C Gemmel, W Heil, S Karpuk, K Lenz, Ch Ludwig, Yu Sobolev, K Tullney, M Burghoff, W Kilian, S Knappe-Grüneberg, et al. Ultra-sensitive magnetometry based on free precession of nuclear spins. *The European Physical Journal D-Atomic, Molecular, Optical and Plasma Physics*, 57(3):303–320, 2010.
- [114] Norman Bobroff. Position measurement with a resolution and noise-limited instrument. *Review of Scientific Instruments*, 57(6):1152–1157, 1986.
- [115] Ling Chen, Charles E Cottrell, and Alan G Marshall. Effect of signal-to-noise ratio and number of data points upon precision in measurement of peak amplitude, position and width in fourier transform spectrometry. *Chemometrics and intelligent laboratory systems*, 1(1):51–58, 1986.

Bibliography

- [116] Achim Karger. Precision of parameters determined by spectrophotometric measurements: Part 2. precision of the first-order rate constant as obtained by spectrophotometric determination. *Chemometrics and intelligent laboratory systems*, 8(2):217–226, 1990.
- [117] Christoph Barmet, Nicola De Zanche, Bertram J Wilm, and Klaas P Pruessmann. A transmit/receive system for magnetic field monitoring of in vivo mri. *Magnetic resonance in medicine*, 62(1):269–276, 2009.
- [118] Eric Growney, Gary Friedman, and Rex Gerald. Computation of distortions in magnetic field and spectrum for nuclear magnetic resonance instruments. *Journal of applied physics*, 85(8):5205–5207, 1999.
- [119] BW Petley and RW Donaldson. The temperature dependence of the diamagnetic shielding correction for proton nmr in water. *Metrologia*, 20(3):81, 1984.
- [120] DR Lide and WM Haynes. *CRC handbook of chemistry and physics: a ready-reference book of chemical and physical data*-editor-in-chief, David R. Lide; ass. ed. WM" Mickey" Haunes. Boca Raton, Fla: CRC, 2009.
- [121] Benjamin E Dietrich, David O Brunner, Bertram J Wilm, Christoph Barmet, and Klaas P Pruessmann. Continuous magnetic field monitoring using rapid re-excitation of nmr probe sets. *IEEE transactions on medical imaging*, 35(6):1452–1462, 2016.
- [122] Marco Grisi, Franck Vincent, Beatrice Volpe, Roberto Guidetti, Nicola Harris, Armin Beck, and Giovanni Boero. Nmr spectroscopy of single sub-nl ova with inductive ultra-compact single-chip probes. *Scientific reports*, 7, 2017.
- [123] Philipp Selenko and Gerhard Wagner. Looking into live cells with in-cell nmr spectroscopy. *Journal of structural biology*, 158(2):244–253, 2007.
- [124] Zach Serber, Lorenzo Corsini, Florian Durst, and Volker Dötsch. In-cell nmr spectroscopy. *Methods in enzymology*, 394:17–41, 2005.
- [125] Daisuke Sakakibara, Atsuko Sasaki, Teppei Ikeya, Junpei Hamatsu, Tomomi Hanashima, Masaki Mishima, Masatoshi Yoshimasu, Nobuhiro Hayashi, Tsutomu Mikawa, Markus Wälchli, et al. Protein structure determination in living cells by in-cell nmr spectroscopy. *Nature*, 458(7234):102–105, 2009.
- [126] RT Eakin, LO Morgan, CT Gregg, and NA Matwiyoff. Carbon-13 nuclear magnetic resonance spectroscopy of living cells and their metabolism of a specifically labeled ¹³c substrate. *FEBS letters*, 28(3):259–264, 1972.
- [127] Angelique Y Louie, Martina M Hüber, Eric T Ahrens, Ute Rothbächer, Rex Moats, Russell E Jacobs, Scott E Fraser, and Thomas J Meade. In vivo visualization of gene expression using magnetic resonance imaging. *Nature biotechnology*, 18(3):321–325, 2000.

- [128] Benjamin J Blaise, Jean Giacomotto, Bénédicte Elena, Marc-Emmanuel Dumas, Pierre Toulhoat, Laurent Ségalat, and Lyndon Emsley. Metabotyping of *caenorhabditis elegans* reveals latent phenotypes. *Proceedings of the National Academy of Sciences*, 104(50):19808–19812, 2007.
- [129] Stanislav S Rubakhin, Elena V Romanova, Peter Nemes, and Jonathan V Sweedler. Profiling metabolites and peptides in single cells. *Nature methods*, 8(4s):S20–S29, 2011.
- [130] Renato Zenobi. Single-cell metabolomics: analytical and biological perspectives. *Science*, 342(6163):1243259, 2013.
- [131] Byron F Brehm-Stecher and Eric A Johnson. Single-cell microbiology: tools, technologies, and applications. *Microbiology and molecular biology reviews*, 68(3):538–559, 2004.
- [132] James B Aguayo, Stephen J Blackband, Joseph Schoeniger, Mark A Mattingly, and Markus Hintermann. Nuclear magnetic resonance imaging of a single cell. 1986.
- [133] JS Schoeniger, N Aiken, E Hsu, and SJ Blackband. Relaxation-time and diffusion nmr microscopy of single neurons. *Journal of Magnetic Resonance, Series B*, 103(3):261–273, 1994.
- [134] Samuel C Grant, Nanci R Aiken, H Daniel Plant, Stephen Gibbs, Thomas H Mareci, Andrew G Webb, and Stephen J Blackband. Nmr spectroscopy of single neurons. *Magnetic resonance in medicine*, 44(1):19–22, 2000.
- [135] Seung-Cheol Lee, Jee-Hyun Cho, Daniel Mietchen, Young-Sook Kim, Kwan Soo Hong, Chulhyun Lee, Dongmin Kang, Ki Deok Park, Byong-Seok Choi, and Chaejoon Cheong. Subcellular in vivo 1 h mr spectroscopy of *xenopus laevis* oocytes. *Biophysical journal*, 90(5):1797–1803, 2006.
- [136] Seung-Cheol Lee, Daniel Mietchen, Jee-Hyun Cho, Young-Sook Kim, Cheolsu Kim, Kwan Soo Hong, Chulhyun Lee, Dongmin Kang, Wontae Lee, and Chaejoon Cheong. In vivo magnetic resonance microscopy of differentiation in *xenopus laevis* embryos from the first cleavage onwards. *Differentiation*, 75(1):84–92, 2007.
- [137] Choong H Lee, Jeremy J Flint, Brian Hansen, and Stephen J Blackband. Investigation of the subcellular architecture of 17 neurons of *aplysia californica* using magnetic resonance microscopy (mrm) at 7.8 microns. *Scientific reports*, 5:11147, 2015.
- [138] SC Grant, DL Buckley, S Gibbs, AG Webb, and SJ Blackband. Mr microscopy of multicomponent diffusion in single neurons. *Magnetic Resonance in Medicine*, 46(6):1107–1112, 2001.
- [139] Jonathan V Sehy, Joseph JH Ackerman, and Jeffrey J Neil. Water and lipid mri of the *xenopus* oocyte. *Magnetic resonance in medicine*, 46(5):900–906, 2001.

Bibliography

- [140] S Püser, A Zschunke, A Khuen, and K Keller. Estimation of water content and water mobility in the nucleus and cytoplasm of xenopus laevis oocytes by nmr microscopy. *Magnetic resonance imaging*, 13(2):269–276, 1995.
- [141] Alan Wong, Xiaonan Li, Laurent Molin, Florence Solari, Bónódicte Elena-Herrmann, and Dimitris Sakellariou. μ high resolution-magic-angle spinning nmr spectroscopy for metabolic phenotyping of caenorhabditis elegans. *Analytical chemistry*, 86(12):6064–6070, 2014.
- [142] Rainer Flindt. *Amazing numbers in biology*. Springer Science & Business Media, 2006.
- [143] Zhengchao Dong. Proton mrs and mrsi of the brain without water suppression. *Progress in nuclear magnetic resonance spectroscopy*, 86:65–79, 2015.
- [144] John R Holmes, Daniel Kivelson, and William C Drinkard. Proton magnetic resonance spectrum of hdo. *The Journal of Chemical Physics*, 37(1):150–152, 1962.
- [145] Timothy L Peck, Richard L Magin, and Paul C Lauterbur. Design and analysis of microcoils for nmr microscopy. *Journal of Magnetic Resonance, Series B*, 108(2):114–124, 1995.
- [146] DA Seeber, RL Cooper, L Ciobanu, and CH Pennington. Design and testing of high sensitivity microreceiver coil apparatus for nuclear magnetic resonance and imaging. *Review of Scientific Instruments*, 72(4):2171–2179, 2001.
- [147] Kevin R Minard and Robert A Wind. Picoliter 1 h nmr spectroscopy, 2002.
- [148] Vlad Badilita, Robert Ch Meier, Nils Spengler, Ulrike Wallrabe, Marcel Utz, and Jan G Korvink. Microscale nuclear magnetic resonance: a tool for soft matter research. *Soft Matter*, 8(41):10583–10597, 2012.
- [149] Clément Pontoizeau, Laurent Mouchiroud, Laurent Molin, Adeline Mergoud-dit Lamarche, Nicolas Dalliére, Pierre Toulhoat, Bénédicte Elena-Herrmann, and Florence Solari. Metabolomics analysis uncovers that dietary restriction buffers metabolic changes associated with aging in caenorhabditis elegans. *Journal of proteome research*, 13(6):2910–2919, 2014.
- [150] Lidia S Szczepaniak, Evelyn E Babcock, Fritz Schick, Robert L Dobbins, Abhimanyu Garg, Dennis K Burns, J Denis McGarry, and Daniel T Stein. Measurement of intracellular triglyceride stores by h spectroscopy: validation in vivo. *American Journal of Physiology-Endocrinology And Metabolism*, 276(5):E977–E989, 1999.
- [151] D Sakellariou, G Le Goff, and J-F Jacquinet. High-resolution, high-sensitivity nmr of nanolitre anisotropic samples by coil spinning. *Nature*, 447(7145):694–697, 2007.
- [152] Rama Jayasundar, Savita Ayyar, and P Raghunathan. Proton resonance imaging and relaxation in raw and cooked hen eggs. *Magnetic resonance imaging*, 15(6):709–717, 1997.

- [153] David K Gardner, Michelle Lane, Antje Spitzer, and Paul A Batt. Enhanced rates of cleavage and development for sheep zygotes cultured to the blastocyst stage in vitro in the absence of serum and somatic cells: amino acids, vitamins, and culturing embryos in groups stimulate development. *Biology of Reproduction*, 50(2):390–400, 1994.
- [154] Fabienne Devreker and Yvon Englert. In vitro development and metabolism of the human embryo up to the blastocyst stage. *European Journal of Obstetrics & Gynecology and Reproductive Biology*, 92(1):51–56, 2000.
- [155] Elisabet Rodríguez-González, Manel López-Bejar, María-José Mertens, and María-Teresa Paramio. Effects on in vitro embryo development and intracellular glutathione content of the presence of thiol compounds during maturation of prepubertal goat oocytes. *Molecular reproduction and development*, 65(4):446–453, 2003.
- [156] Lalantha R Abeydeera, Wei-Hua Wang, Thomas C Cantley, August Rieke, and Billy N Day. Coculture with follicular shell pieces can enhance the developmental competence of pig oocytes after in vitro fertilization: relevance to intracellular glutathione. *Biology of reproduction*, 58(1):213–218, 1998.
- [157] AM Brad, CL Bormann, JE Swain, RE Durkin, AE Johnson, AL Clifford, and RL Krisher. Glutathione and adenosine triphosphate content of in vivo and in vitro matured porcine oocytes. *Molecular reproduction and development*, 64(4):492–498, 2003.
- [158] Zofia Luberda. The role of glutathione in mammalian gametes. *Reprod Biol*, 5(1):5–17, 2005.
- [159] Kurt A Zuelke, Susan C Jeffay, Robert M Zucker, and Sally D Perreault. Glutathione (gsh) concentrations vary with the cell cycle in maturing hamster oocytes, zygotes, and pre-implantation stage embryos. *Molecular reproduction and development*, 64(1):106–112, 2003.
- [160] Hiroaki Funahashi, Naoya Bandoh, Shinobu Nakahira, She-Hoon Oh, and Seiji Tsuboi. Changes in intracellular content of glutathione and thiols associated with γ -glutamyl cycle during sperm penetration and pronuclear formation in rat oocytes. *Zygote*, 7(04):301–305, 1999.
- [161] Emre Seli, Lucy Botros, Denny Sakkas, and David H Burns. Noninvasive metabolomic profiling of embryo culture media using proton nuclear magnetic resonance correlates with reproductive potential of embryos in women undergoing in vitro fertilization. *Fertility and sterility*, 90(6):2183–2189, 2008.
- [162] John Paul Urbanski, Mark T Johnson, David D Craig, David L Potter, David K Gardner, and Todd Thorsen. Noninvasive metabolic profiling using microfluidics for analysis of single preimplantation embryos. *Analytical chemistry*, 80(17):6500–6507, 2008.

Bibliography

- [163] Telma Cristina Esteves, Fleur van Rossem, Verena Nordhoff, Stefan Schlatt, Michele Boiani, and Séverine Le Gac. A microfluidic system supports single mouse embryo culture leading to full-term development. *RSC advances*, 3(48):26451–26458, 2013.
- [164] Hakho Lee, Yong Liu, Donhee Ham, and Robert M Westervelt. Integrated cell manipulation system—cmos/microfluidic hybrid. *Lab on a Chip*, 7(3):331–337, 2007.
- [165] Lee Hartley, Karan VIS Kaler, and Orly Yadid-Pecht. Hybrid integration of an active pixel sensor and microfluidics for cytometry on a chip. *IEEE Transactions on Circuits and Systems I: Regular Papers*, 54(1):99–110, 2007.
- [166] Ingemar Jönsson, Eliana Beltran-Pardo, Siamak Haghdoost, Andrzej Wojcik, Rosa María Bermúdez-Cruz, Jaime E Bernal Villegas, and Mats Harms-Ringdahl. Tolerance to gamma-irradiation in eggs of the tardigrade richtersius coronifer depends on stage of development. *Journal of limnology*, 72(1s):9, 2013.
- [167] Dorice M Czajka, Asher J Finkel, Conrad S Fischer, and Joseph J Katz. Physiological effects of deuterium on dogs. *American Journal of Physiology—Legacy Content*, 201(2):357–362, 1961.
- [168] Sutiman Bambang Sumitro and Hidemi Sato. The isotopic effects of d20 in developing sea urchin eggs. *Cell structure and function*, 14(1):95–111, 1989.
- [169] J Wabo Poné, Olivia Fossi Tankoua, Jeannette Yondo, Marie Claire Komtangi, Mpoame Mbida, and CF Bilong Bilong. The in vitro effects of aqueous and ethanolic extracts of the leaves of *ageratum conyzoides* (asteraceae) on three life cycle stages of the parasitic nematode *heligmosomoides bakeri* (nematoda: Heligmosomatidae). *Veterinary medicine international*, 2011, 2011.
- [170] Sydney Brenner. The genetics of *caenorhabditis elegans*. *Genetics*, 77(1):71–94, 1974.



Marco Grisi

E-mail: marco.grisi.88@gmail.com

Personal Information

Nationality: Italian

Date of Birth: January 4th, 1988

Education

- February 2013 – June 2017, **PhD in microelectronics and microengineering, EPFL, Lausanne (CH)**.
Design of CMOS single-chip transceivers for micro-NMR spectroscopy and high field magnetometry.
- October 2010 – October 2012, **Master in theoretical-computational physics, Università degli studi di Milano Bicocca, Milano (IT)**. *110/110 with honors, winner of 2010/2011 university scholarship.*
- November 2011 – July 2012, **Master thesis project, LENS (European Laboratory of non-linear spectroscopy), Sesto Fiorentino (IT)**. *Levy walks in bounded systems and study of light propagation in complex optical materials.*
- September 2007 – October 2010, **Bachelor in physics, Università Statale degli studi di Milano, Milano (IT)**. *110/110 with honors, winner of 2007/2008 and 2008/2009 university scholarship.*
- June 2010 – September 2010, **Bachelor thesis project, Cavendish Laboratory, Cambridge (UK)**. *Fluorescence microscopy on E.coli strains and analysis of the anomalous diffusion of genes in cytoplasm.*
- September 2009 – June 2010, **Erasmus project, Queen Mary University (QMUL) and University College (UCL), London (UK)**.

Peer-reviewed Publications

- Javer, A., Long, Z., Nugent, E., Grisi, M., Siriawatwetchakul, K., Dorfman, K. D., ... & Lagomarsino, M. C. (2013). *Short-time movement of E. coli chromosomal loci depends on coordinate and subcellular localization*. **Nature communications**, 4.
- Svensson, T., Vynck, K., Grisi, M., Savo, R., Burreli, M., & Wiersma, D. S. (2013). *Holey random walks: Optics of heterogeneous turbid composites*. **Physical Review E**, 87(2), 022120.
- Gualco, G., Grisi, M., & Boero, G. (2014). *Frequency jumps in single chip microwave LC oscillators*. **Applied Physics Letters**, 105(24), 242102.
- Grisi, M., Gualco, G., & Boero, G. (2015). *A broadband single-chip transceiver for multi-nuclear NMR probes*. **Review of Scientific Instruments**, 86(4), 044703.
- Yesilkoy, F., Ueno, R., Desbiolles, B. X. E., Grisi, M., Sakai, Y., Kim, B. J., & Brugger, J. (2016). *Highly efficient and gentle trapping of single cells in large microfluidic arrays for time-lapse experiments*. **Biomicrofluidics**, 10(1), 014120.
- Grisi, M., Vincent, F., Volpe, B., Guidetti, R., Harris, N., Beck, A., & Boero, G. (2017). *NMR spectroscopy of single sub-nL ova with inductive ultra-compact single-chip probes*. **Scientific Reports** 7.

Conference talks

- M. Grisi, B. Volpe, R. Guidetti, N. Harris, G. Boero. (2016). *NMR spectroscopy of subnanoliter ova with ultra-compact single-chip probes*. **EUROMAR 2016, Aarhus (DK)** promoted talk.
- M. Grisi, G. Boero. (2017). *Broadband IQ CMOS transceivers for compact and ultra-compact NMR probes*. **ENC 2017, Asilomar (CA, USA)**, promoted talk.

